UNIVERSITÀ DEGLI STUDI DI MILANO

Facoltà di Scienze Matematiche, Fisiche e Naturali

Dottorato di Ricerca in Fisica, Astrofisica e Fisica Applicata

CONFORMAL WALKS IN TWO DIMENSIONS

Settore Scientifico Disciplinare FIS/02

Coordinatore: Prof. Gianpaolo Bellini

Tutore: Prof. Sergio Caracciolo

Tesi di Dottorato di
Marco GHERARDI
Ciclo XXI

Anno Accademico 2008/2009

Contents

Introduction

This work deals with the statistical properties of some walk models in two dimensions in their critical limits, with particular attention to their conformal invariance.

Statistical mechanics is the framework in which physicists study systems with a large number of degrees of freedom. Exact methods for solving the equations of motion often become useless already when the number of degrees of freedom is of order 10 (see for instance the three-body problem). Say one is interested in the behavior of a large collection of interacting objects, such as the molecules in a gas, the dipoles in a magnet, or even cars on a highway. Oftentimes not only is it impossible to exactly solve the equation governing such complex situations, but also it would be experimentally unfeasible to measure all the initial conditions that are to be plugged into the equations in order to get the trajectories of the single objects. Moreover, in the end one is not really interested in having access to such a huge load of information. The change in paradigm introduced by statistical mechanics is a change of focus from the many *microscopical* quantities to a few number of *macroscopical* observables. In the examples above, these could be for instance temperature for gases, mean magnetization for magnets, or number of jams for traffic. By following this strategy, an initially complicated problem gets reduced to more tractable (and — often — interesting) approximations regarding a restricted set of quantities. These approximations turn out to be more and more precise as the so-called *thermodynamic* limit is reached, that is, the limit as the number of degrees of freedom goes to infinity.

A great majority of the interesting models in statistical mechanics (the self-avoiding walk we will define in Chapter 1 is a notable exception) have one or more parameters, which represent the tunable characteristics of the physical situation, the metaphorical experimentalist's *knobs*. For instance, in modeling, say, a swarm of mosquitos, after having decided what the interaction between the single insects would be (e.g. everyone flies following its nearest neighbors), one can leave the *strength* of this interaction unspecified (e.g. *how much* one is affected by the direction its nearest neighbors

are flying). The goal of statistical mechanics is the to study the behavior of the system as a function of the parameters. When doing so, a very common feature of statistical systems emerges, which is the presence of *critical points*. Roughly speaking, a critical point is a particular choice of the parameters (there could also be a whole continuum of such choices, that is a continuum of critical points) where the system does not behave in an analytical fashion. Some observables could become infinite, others could be non-continuous. Actually, such a non-analytical behavior is impossible to get if we consider only a finite number of degrees of freedom, since the so-called *partition function*, from which every interesting quantity can be calculated, is then a finite sum of terms, and therefore analytical. But in the true thermodynamic limit, the terms become infinite, and if every degree of freedom in the system "cooperate", observable features of the system may actually become infinite. The hallmark of such a critical point is the divergence of the *correlation length*, which describes the scale at which the microscopical degrees of freedom "cooperate" (i.e. are correlated).

Critical phenomena show a variety of interesting behaviors, but they also manifest an important "grouping" feature, ubiquitous in physics: *universality*. Universality is displayed by systems in which the microscopic degrees of freedom behave and interact in possibly very different ways, but which display identical qualitative and quantitative behavior at their critical points. (See Section 1.3 for a deeper explanation).

In this work we shall study lattice walks from a statistical-mechanics point of view. A *lattice* is a regular graph, composed of nodes (sites) and links between them, the latter defining a notion of *neighborhood* on the lattice. A lattice *walk* is an ordered collection of sites such that two consecutive sites are connected by a link. An *ensemble* of walks can be defined by collecting together many of them (usually sharing some property) each with its own *statistical weight*. This amounts to considering an experiment the outcome of which is a lattice walk with certain properties — characterized by a probability distribution — but which is otherwise unpredictable. One can ask questions such as "What is the mean number of steps?", "What is the mean distance travelled?", "How strong are the deviations from the average behavior?", and so on.

Why study lattice walk models? Firstly, there is a direct application to actual problems in *polymer science* (see Chapter 1. Polymers are ordered

collections of unit cells (called *monomers*) and experiments and industrial applications usually treat a very high number of identical polymers at once. Hence the interest in a statistical description of the polymer's properties. Secondly, walk models are stimulating mathematical objects, with connections to many other fields, such as *field theory* (Section 1.3), *conformal field theory* (CFT) in two dimensions (Section 2.5), geometric critical phenomena. By varying the type of local interaction between the monomers, polymer models flow into many universality classes studied in other fields. Dense polymers are a well-known realization of a $c = -2$ (logarithmic) CFT, ..., and — rather amazingly — tricritical polymers at the collapse transition are described by a geometric critical phenomenon (namely percolation) which does not really need any tuning (see Chapter 1).

The divergence of the correlation length at criticality is a crucial feature when the *continuum limit* of the lattice model is to be defined. The continuum limit is reached by embedding the lattice in the continuum (for instance $\mathbb{R}^2$ or $\mathbb{C}$ in two dimensions), sending the lattice spacing to zero and the size of the lattice to infinity at the same time, in such a way that the correlation length does not scale to zero, because otherwise the continuum model would be trivial. This is why the continuum limit is defined for the lattice system *at criticality*. In this way we obtain a critical continuum system. Another way of keeping the continuum correlation length away from zero is to reach the thermodynamic and the critical limit at the same time, by keeping some combination of the two characteristic scales (size and lattice correlation length) fixed. This limiting procedure is called *critical crossover limit* and yields a non-zero but finite continuum correlation length. What comes out is known as a *massive* theory — in the field-theoretic jargon, mass is the inverse of the correlation length — or an *off-critical* model, as it is called in the mathematic literature.

In this work we will be solely interested in the usual critical limit, where the lattice model sits at its critical point, since this is the situation that displays *conformal invariance*. Critical systems are rotationally and scale-invariant (such is their fractal nature), but usually (there are exceptions) they also exhibit a much broader symmetry group: that of conformal transformations (see Section 2.2). Conformal invariance in two dimensions is a strict requirement which is full of consequences for the properties of the statistical system, ranging from the scaling form of the correlation functions to exact prediction of the critical exponents. The study of these properties is one of the applications of *conformal field theory* (see Section 2.5 for some references).

But when continuum walk models are concerned, yet another method is available for the study of the statistical properties of conformally-invariant

systems. It was introduced by Loewner in the early twentieth century for studying the geometry of interfaces and has revived in the very late years of the century thanks to the brilliant work of Oded Schramm. The basic idea is to turn attention from the walks themselves to some conformal maps that encode every information about them, so that every possible walk has an associated element in the group of conformal maps (namely, the one that maps the "exterior" of the walk to some standard domain). It is possible to obtain a differential equation for the parametrized family of maps which describe the time parametrization of a single walk. This is called a *Loewner evolution*. The generalization introduced by Schramm was a *stochastic* version of it (thus involving a stochastic differential equation), which is called *Schramm-Loewner evolutions*, or *SLE*. SLE is a powerful framework for demonstrating non-rigorous results obtained through other methods, and has proved useful for performing new calculations and even for exploring new directions in CFT and geometric phenomena (see Chapter 2).

In this work we will be interested in the critical behavior and the continuum limits of some lattice walk models, namely the *self-avoiding walk* and the *interacting self-avoiding walks* (see Chpater 1). A connection has been (non-rigorously) established between these two models and SLE when the environment is a half-plane. From a CFT point of view the presence of a boundary (as is the case for the half-plane) is a very important feature. We will be interested in studying this connection when the domain is the whole plane. Moreover we will concentrate on the critical behavior of the interacting self-avoiding walks (the so-called θ point). Most of the present work relies on extensive numerical analysis obtained through careful Montecarlo simulations of the models.

Chapter 1 introduces the modelization of polymers in a solution and the lattice walk models we will be using. It also includes a discussion of what universality means and why it is of such importance for the subject at hand. In Chapter 2 we first recall some concepts from the theory of conformal maps and then introduce SLE. We describe some of its properties, the connection to CFT, and review the relevant results in the extensive literature. Chapter 3 describes the methods we will use for the numerical simulation of SLE, starting from the well-known half-plane case and concluding with the whole plane, which is the relevant case for our purposes. Chapter 4 is a somewhat technical investigation of three ways of approaching the problem of reparametrizing

the SLE curves, which is crucial for the kind of connection that we want to establish here. Chapter 5 presents a wealth of numerical data about the θ point. We obtain high precision estimates of the critical exponents and the shape of the distribution functions, finding good agreement with theory. In Chapter 6 we finally compare the walk models and the SLE in the whole plane. We test a conjecture by Werner, and reveal an unexpected result. The appendices gather some calculations which are essential building blocks of our algorithm described in Chapter 3.

Chapters 1 and 2 are mainly reviews. Chapter 3 is a review of very recent literature. The last section of Chapter 3 is original material. Everything in Chapter 4 is original, except for the concept of fractal variation. The first section of Chapter 5 is a review of theoretical results, while the second section is original numerical work. Chapter 6 is original.

Chapter 1

Polymers on the lattice

In this chapter we review what polymers are, and how they are modeled by means of lattice models. We focus on the self-avoiding walks, the interacting self-avoiding walks and the percolation explorer, which will play central roles in the following chapters.

1.1 Polymers in a solvent

A *polymer* [1, 2, 3, 4, 5, 6] is a long, repeating chain of atoms, formed through the linkage of many molecules, called *monomers*. When the number of bonds becomes large, the overall polymer dimensions greatly exceed those of the constituent monomer units; because of its large dimensions the polymer is also called a *macromolecule*; real polymers can consist of more than 10^5 monomers.

$$X - X - X - \cdots - X$$

If the monomers (X) are identical then the chain is called a *homopolymer*, otherwise it is called a *heteropolymer*. The number of monomers in a single chain (usually denoted by N) is called *degree of polymerization*, and is a very important quantity, because it is responsible — as will be clear in the following — of the approach to criticality. When one considers ensembles of polymers, two different choices are possible with respect to the degree of polymerization: one considers either fixed-N or variable-N ensembles. The former case is referred to as *monodisperse*, while the latter is the *polydisperse* ensemble. In this work we will be dealing mainly with monodisperse homopolymers.

When a large number of polymers is put together, the different chains interact with each other. The bulk properties of this ensemble depend on the type of polymers and on the temperature: the phase can be solid, liquid, or

glassy. The liquid phase is characterized by its viscosity, which raises rapidly with the molecular mass, but its behavior under external solicitation is viscoelastic, that is, the liquid reacts at first in an elastic way, and the viscosity manifest itself only after a time which raises with the molecular mass. In general, the bulk properties of mass polymers are hard to describe mathematically, because several kinds of interactions are involved, and because the polymers all interact with each other. An example of the complex behavior of these ensembles is the glassy transition, that is the transition between the glassy and the solid phase: the transition temperature depends on the speed at which the temperature is lowered. This complexity is smoothed when one considers polymers in diluted solutions.

A complete theory of polymers — be it solutions, melts, or solid state — would be enormously complicated and almost certainly the mathematical and computational difficulties in solving or extracting valuable information from a thorough model would be severe. Modelization of polymers in the framework of statistical mechanics and the renormalization group [see chapter 4] helps in both simplifying the models one has to study and providing new techniques and new perspectives that are valuable tools in coping with the problems encountered when investigating such a vast and faceted subject.

In general, a polymer model on a configuration space Ω (be it on a lattice, on continuum space, with discrete segments or with continuous chains) can be described by means of an ensemble of instances $\{\omega\}$, specified — with respect to an underlying measure $d\mu$ on the state space — by a Hamiltonian $H[\omega]$ which specifies the energy of a configuration. The Hamiltonian gives information about the system statistics through the postulation of the Gibbs distribution, by which the mean value of an observable $O[\omega]$ over the ensemble is given by

$$\langle O \rangle_H = \frac{1}{Z} \int_\Omega e^{-\beta H[\omega]} O[\omega] d\mu[\omega] \tag{1.1}$$

where

$$Z = \int_\Omega e^{-\beta H[\omega]} d\mu[\omega] \tag{1.2}$$

is called *partition function*, and β is the *inverse temperature*.

When two monomers become close in space, they repel each other through a force F whose strength depends on the separation between them, as well as on the chemistry of each bead and on temperature and pressure conditions. When a liquid solvent is introduced into the system, and a dilute solution is generated, other kinds of interactions are present. Now each bead has a chance to interact with solvent molecules as well as other beads. As a result, the *effective force* $F + F'$ that acts between a pair of beads is no longer equal

to the vacuum value F, because it gets mediated by the solvent, which contributes a force F'. The type of this mediation — which modifies the effective interaction that drives the chain — depends on the particular choice of the two constituents of the solution, and on the temperature. Solvent-mediated interactions can be either repulsive or attractive. If the bead-solvent interaction favors bead-solvent contact over the bead-bead one, the solvent is said to be a *good solvent* (for the polymer and temperature considered), while if the reverse is the case, it is called a *poor solvent*. In a good solvent the segment-solvent interaction tends to pull pairs of segments apart, so that the effective force F' is repulsive as is F. On the other hand F' is attractive in poor solvents. A solution of two fixed constituents can be made poorer or better by changing the temperature: the hotter, the better. There happen to exist a certain temperature — called θ *temperature* — for which on average $F + F' = 0$. Roughly speaking, at the theta temperature the attractive forces exactly balance the repulsive ones; the chain is then expected to behave ideally. Actually, we will see that in two dimensions the θ-point behavior is far from ideal, but is nonetheless different from the good- and poor-solvent ones.

In the good solvent regime, the chain is expected to be in a swelled state. This means that the average extension of the polymer has to be larger than in the non-interacting case, because now the interactions are mainly repulsive. On the contrary, for a poor solvent below the θ temperature, the polymer is expected to be dominated by the attractive interactions between its monomers, so that it will be found in a globular collapsed state. A way to measure how much a walk is collapsed or swelled is by looking at how its size scales with the number of steps. In polymer theory, this corresponds to considering how the size of the polymer depends on the number of monomers in the chain. Let us call R the approximate size of the chain (more precise definitions will be given in Chapter 5). Then one expects that for N large

$$R \sim N^{\nu} \tag{1.3}$$

where ν is sometimes called *swelling exponent* and is an example of a critical exponent (see Section 1.3). It is easy to see that $\nu = 1/2$ for simple random walks or Brownian motion (which are the simplest polymeric models), for which Equation 1.3 is the well-known relation between time and space, and it holds in any dimension. For a collapsed polymer one expects that all available space is occupied by the chain (one says that it is *space-filling*) so that $\nu = 1/d$. For swelled and θ-point polymers, on the other hand, ν takes non-trivial values.

1.2 Models

1.2.1 Self-avoiding walks

Consider N-step walks ω taking values on some lattice Λ. ω is defined as the ordered collection of lattice sites $\omega_0, \ldots, \omega_N$ such that ω_i and ω_{i+1} are lattice nearest neighbors. By translation invariance we will always fix ω_0 to be the origin. We restrict to walk that do not visit any site of Λ more than once. The flat measure on such walks is a model called the *self-avoiding walk* (SAW).

Microscopically, this models a repulsive interaction (which is short-ranged in space, but long-ranged in the length of the walk). One could also allow for some self-intersections, but discourage them by assigning an energy to each of them. Such a model is called Domb-Joyce, and it is known to lie in the same universality class as the SAW for any finite temperature.

There is a wealth of rigorous results on the SAW; see for instance the book by Madras and Slade [7].

What we will be interested in, is the behavior of the ensemble as $N \to \infty$, since it is only in this regime that the correlation length (for a precise definition, see Chapter 5) becomes infinite, and one can hope to obtain a non-trivial scaling limit. Not much is known *rigorously* in this limit, and the connection with the Schramm-Loewner evolution we will be focusing on in most of this work helps to shed light on some of the interesting questions in this regard.

An example of a typical SAW on the square lattice is displayed in Figure 1.1. (For an account of the manifold numerical methods for the SAW see [8]).

1.2.2 Interacting SAWs

As we have seen, the SAW models the repulsive interaction which is dominant in good solvents. If one instead wants to model poor solvents and the transition between the two regimes, then opposite-sign interactions must be introduced. One possibility is to consider an attractive interaction between neighboring sites: the walk can not pass more than once on the same site (it is still self-avoiding), but if it comes close to itself it looses energy.

Thus, for each walk we define an energy function $\mathcal{E}$ defined as follows:

$$\mathcal{E} \equiv -\sum_{i=0}^{N-2} \sum_{j=i+2}^{N} c_{ij}, \tag{1.4}$$

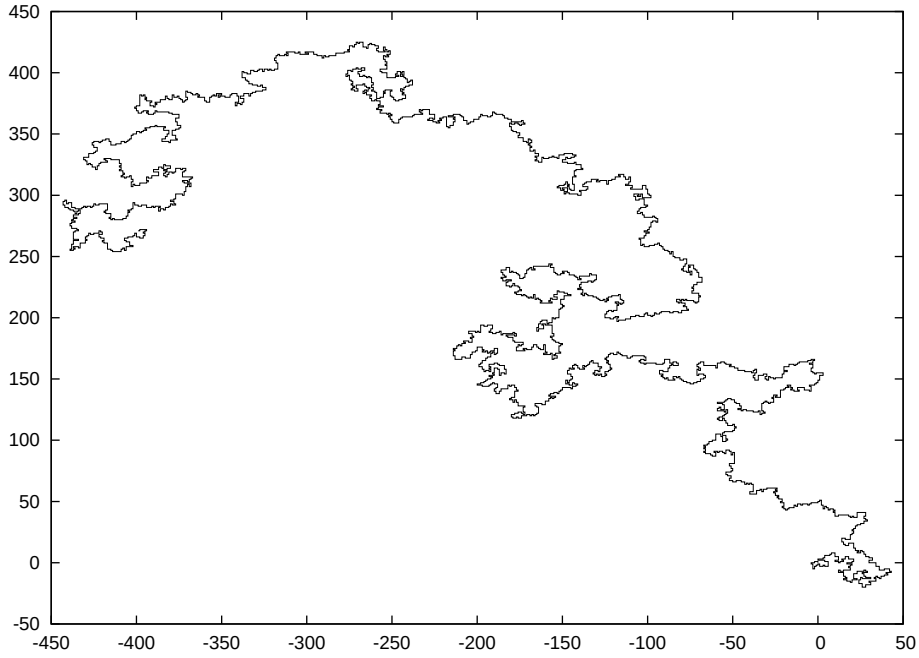

Figure 1.1: A typical self-avoiding walk on the square lattice ($N = 5000$).

where

$$c_{ij} \equiv \begin{cases} 1 & \text{if } |\omega_i - \omega_j| = 1 \\ 0 & \text{otherwise} \end{cases} \tag{1.5}$$

Essentially, $\mathcal{E}$ is the number of nearest-neighbor contacts without considering the trivial contacts between subsequent monomers.

We consider the ensemble of N-step walks with partition function

$$Z_N = \sum_{\{\omega\}} e^{-\beta\mathcal{E}}, \tag{1.6}$$

where β is the inverse temperature and the sum is extended over all N-step walks. The model defined in this way is called interacting self-avoiding walk (ISAW). What happens is that there is some critical value β_θ such that for $\beta < \beta_\theta$ the model behaves (in the large-N limit) as the SAW, while for $\beta > \beta_\theta$ one observes a very different behavior: the walk becomes a compact, globule-like, essentially two-dimensional object. Precisely *at* the critical point $\beta = \beta_\theta$ the behavior is yet another, and it at this transition that we will be studying the model the most. This transition is called θ point, coil-globule or collapsing transition. A wide spectrum of results is presented in detail in Chapter 5. A typical θ-point walk is displayed in Figure 1.2.

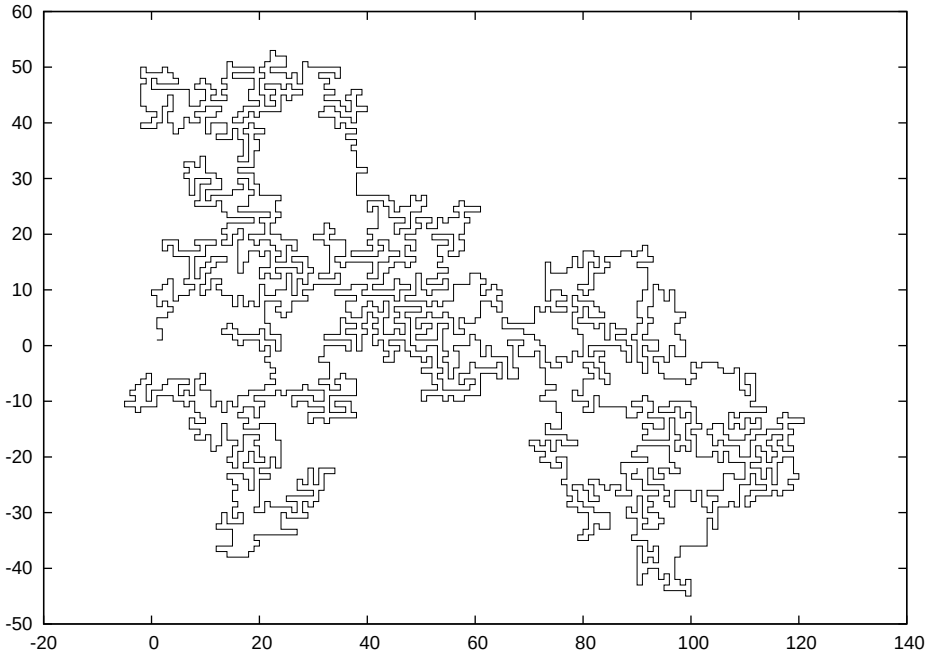

Figure 1.2: A typical θ-point interacting self-avoiding walk on the square lattice ($N = 3000$).

1.2.3 Walks in percolation

Percolation is a vast subject. The interested reader can find a wealth of results and references in [9]. In this section we will be interested in a special case, which is commonly referred to as *site percolation on the triangular lattice*. Actually, we will be working on the *dual* lattice (which in this case is the honeycomb lattice), because this is where the natural notion of *interface* can be defined. A percolation configuration is an assignment of a spin (+ or -) to every plaquette in the hexagonal lattice (corresponding to sites in the triangular lattice). Every plaquette gets a + with probability $0 \leq p \leq 1$ (we will then color it gray) or a - with probability $1 - p$ (we will then color it white). One focuses on the connectivity properties of the clusters of gray cells. Of course, if p is close to 0 then gray hexagons will be rare, while when p is close to 1 almost every cell in the lattice will be colored gray, and there will be a cluster "percolating" through the lattice, that is an *infinite* cluster. There turns out to exist a non trivial p_c such that for $p > p_c$ this happens with probability 1 (while for $p < p_c$ with probability on it does *not* happen). The honeycomb lattice enjoys a particular symmetry by virtue of which it can be argued that $p_c = 1/2$. This is not true in general for other

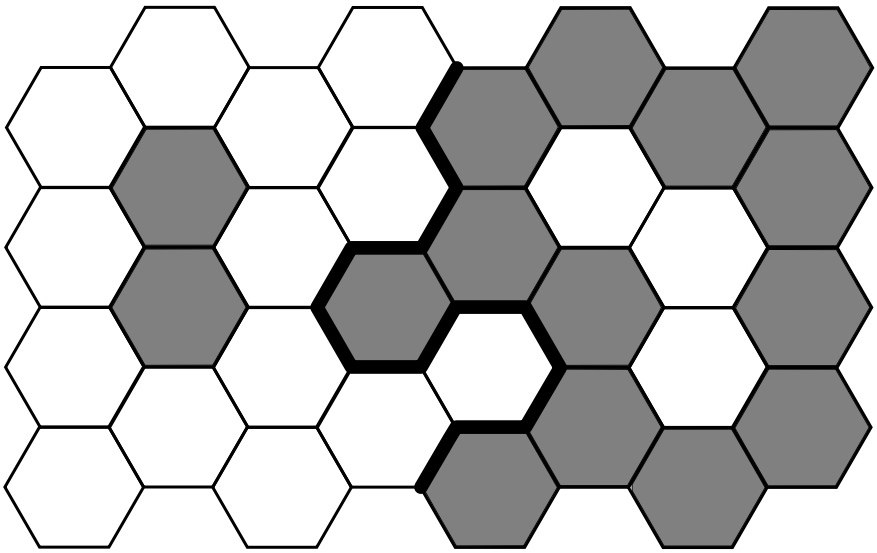

Figure 1.3: A percolation configuration with fixed boundary conditions on the honeycomb lattice and the corresponding interface.

lattices (for instance the square lattice has $p_c > 1/2$). The critical measure on the honeycomb lattice is then simply the flat measure on every possible configuration $\{\sigma_i\}$.

Let us consider a "rectangle" of the honeycomb lattice, with sides $2a$ and $2b$, with a, b two fixed real parameters. To do this, simply label each cell with the coordinates (x, y) that its center gets when the lattice is embedded on the Cartesian plane, and the consider those cells for which $|x| < a$ and $|y| < b$. Refer to Figure 1.3 for an example. Let us fix the value of the spins on the boundary plaquettes of the rectangle, so that the boundary cells with $x > 0$ are grey and those with $x < 0$ are white, for instance. With this choice of boundary conditions, every configuration will produce one *interface* between gray and white cells, which will be a walk defined on the hexagonal lattice itself (it is the only one interface with loose ends: there exist others, but they are all closed curves). Figure 1.3 shows an example of such a configuration, together with its interface.

Notice that, from an operative point of view, we do not really need to know every single spin in a configuration in order to know the interface. Actually, one can grow the curve a step at a time, tossing a coin at every step to choose the color of the single hexagon that the walk is facing. In this way, when the walk has reached the other side of the lattice only the plaquettes that are adjacent to the interface will have been colored. This process is called the *percolation exploration process* and it is then seen to be

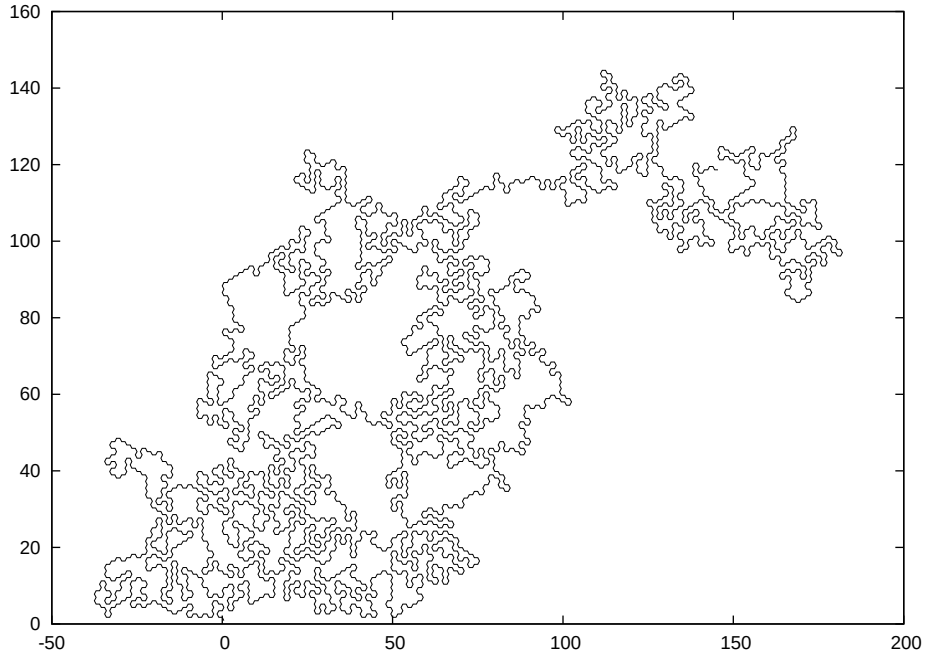

Figure 1.4: A percolation explorer on the honeycomb lattice ($N = 3000$).

local, meaning that a realization of the walk only depends on the plaquettes it visits, and not on the other local degrees of freedom. Figure 1.4 displays one such exploration process, stopped before it reaches the upper side of the lattice. Of course we will be interested in the *scaling limit* of such a process, so we will always be sending the size of the rectangle to infinity, and the lattice spacing to zero.

By construction, these walks are self-avoiding. Let us now try and compare the ensemble generated by the percolation measure with the flat measure on the SAW we defined in Section 1.2.1. Fix a realization of the walk, say ω. How many different realizations of the percolation give rise to ω? Let us call this number $\mathcal{N}(\omega)$. By locality, we know that every spin that is not adjacent to the walk is unconstrained. So we have

$$\mathcal{N}(\omega) = 2^{V-N(\omega)} \tag{1.7}$$

where V is the volume of the lattice and $N(\omega)$ is the number of spins involved in the growing of ω. In order to express $N(\omega)$ in terms of the geometric features of the walk, consider what happens when the walk moves a step further. Four things can happen: (i) the spin of the hexagon ω is facing has not been tossed yet; (ii) the spin has been fixed because the walk has already been facing that hexagon once; (iii) the spin is fixed because the walk has

already been facing that hexagon twice; (iv) the spin is fixed because it is a boundary spin. It is then clear that the number of constrained spins $N(\omega)$ is

$$N(\omega) = (L-1) - N_2 - 2N_3 - N_B, \tag{1.8}$$

where L is the length of the walk, N_i $(i = 1, 2)$ is the number of hexagons hosting i disconnected steps of the walk, and N_B is the number of boundary hexagons touched by the walk. It is with this argument that Coniglio et al. conjectured in [10] that the percolation exploration process and the interacting self-avoiding walk at the θ transition be in the same universality class. Indeed, if one considers fixed-length walks for definiteness, the statistical weight in (1.7) with $N(\omega)$ given by (1.8) displays an attractive interaction between neighboring bonds.

1.3 Universality

The theoretical study of polymer models is focused on the long-chain limit. This is not only because real polymers have high degrees of polymerization. The importance of this particular regime is related to a fundamental aspect of statistical systems: *universality*. We shall devote this section to a — rather informal — discussion of what universality means and implies, since it is the central methodological approach this work is based on.

General statistical system exhibit a vast variety of behaviors, which are specified by the particular choices of a multitude of model parameters, for instance the microscopic characteristics of the model, the approximations introduced, the type of lattice on which the system is placed. But there exists a particular situation in which much more symmetry and simplicity seems to emerge from this apparently wild plethora of behaviors. When they are observed in the true thermodynamic limit (infinite degrees of freedom), statistical systems happen to have a point — that is, a particular choice of their parameters — for which they behave in some non-continuous fashion, and many of their measurable quantities diverge. This point is called *critical point*, and is defined as a particular set of model parameters for which an appropriate *correlation length* diverges. The correlation length is a quantity that measures the typical size of likely fluctuations, that is, the distance along which the system exhibits coherence.

The correlation length defines a typical scale of the system. For a walk model at fixed N, the obvious definition of correlation length would be the mean space travelled by the walker. It is easy to guess that, when this scale becomes infinite, the small-scale characteristics of the model become irrelevant. This is indeed a general property of statistical systems at a critical

point: they exhibit universality; that is, some properties do not depend on the short-scale specifics of the models, and are therefore called *universal*. The *critical exponents*, which describe the rate of divergence of some observables near the critical point, are examples — and perhaps the most important ones — of universal quantities.

Most qualitative and quantitative features of critical phenomena (that is, statistical systems at the critical point) can be understood in the framework of the *renormalization group* (RG) [11, 12]. The RG idea is to study the behavior of the system under some sort of transformation which neglects the small scale particulars of the model, so that truly universal features become apparent. This transformation induces a *renormalization flow* on the space of theories. The fixed points of this flow correspond to those theories which exhibit scale invariance. For a walk model, this means that the walk is self-similar. In critical walk models, for instance, small loops are as likely to be found as large ones, at *all* scales. Critical theories flow towards the fixed points: their universal quantities are the fixed-point universal quantities. In this picture, the parameter space is divided into "attraction basins", each corresponding to a fixed point. Critical theories in the same basin flow towards the same point. As a consequence they will share the same universal properties. Therefore, they are said to be in the same *universality class*.

With universality in mind, it is natural to ask whether there exist a field theory whose universal quantities are those of polymer models. The affirmative answer is due to the original intuition of de Gennes [13]. The remarkable statement is that the statistical properties of polymers in good solutions (respectively, at the θ point) are related to the properties of the critical $g\phi^4$ (respectively, tricritical $g\phi^6$) field theory in the 'unphysical' limit $N \to 0$. As a consequence, all critical exponents for polymer models are those obtained for the zero-component field theory.

In two dimensions there are other methods which are of great help in extracting critical quantities, the most important of which are conformal invariance methods (see for instance [14], for an introduction, and the references given in Section 2.5). The study of conformal invariance properties of polymers, whose central charge — in the terminology of conformal field theory — is zero, has been carried out in [15]. The idea behind these techniques again is based on symmetry considerations. Critical systems in two dimensions are expected to show more than the sole scale invariance. Actually, they usually exhibit invariance under a much wider group of symmetries, namely the *conformal group*, which basically collects *local* scale transformations and rotations. Using the constraints imposed by this infinite-dimensional symmetry group, it is then possible to classify universality classes and to gather information about operators, critical exponents, correlations, and so on (see

Section 2.2 for the definitions and more in-depth discussion).

Another thing that is exactly known from field theory is the upper critical dimension d_+. It is the dimension strictly above which excluded-volume or θ-point polymers behave asymptotically exactly as free (Gaussian) chains (precisely *at* the upper critical dimension, one expects logarithmic corrections to the ideal behavior). Field theory predicts $d_+ = 4$ for the ϕ^4 operator[1], and $d_+ = 3$ for ϕ^6. Indeed, it can be proved that self-avoiding walks in $d > 4$ have the same scaling limit as ordinary random walks. In this work we will be always considering two-dimensional space, so both good-solvent and θ-point behaviors are non-trivial.

[1]Indeed, this is very easy to explain heuristically in the polymer language, since Brownian motion paths have dimension 2, and one expects that two such paths almost never intersect in $d > 2 + 2$: a 4-dimensional walker has a large volume to explore, and will rarely come back to a place it already visited.

Chapter 2

Schramm–Loewner evolutions

This chapter is a (hopefully self-contained) introduction to SLE and some of its applications. It will give the reader everything that is needed to fully understand the material in chapters 3, 4 and 6. For much more thorough and authoritative presentations see for instance reviews [16, 17, 18, 19, 20] and the wealth of references therein.

2.1 Introducing SLE

2.1.1 Motivation

Studying walk models on the lattice, from a physicist's point of view, usually means focusing on the universal properties which are displayed at the critical point. What one is tipically interested in are the critical exponents — which are the descriptors of the *power law* nature of criticality — and the scaling (or crossover) functions. These quantities encode a lot of information about the universality class that the physical situation one is trying to describe belongs to. As far as polymers in a solution are concerned, for instance, the sole swelling exponent ν can tell whether the phase is globule-like, tricritical or swelled, by giving quantitative information about a configurational property of the polymer, namely its size. Crossover functions, on the other hand, effectively describe the universal properties of the approach to criticality, i.e. they encode precious information about the abrupt changes in the behavior of observables that one encounters close to a critical point.

What is usually lacking within this framework is a *complete* description of the scaling limit. By *complete description* one refers to a mathematical formulation of a well-defined continuum model which *is* a (suitably defined) limit of the lattice model as the lattice spacing goes to zero and the volume

goes to infinity. Such a continuum description need not necessarily offer powerful computational methods to address unanswered questions in the lattice framework; in fact this is not the case most of the time. But if one is able to find a continuum description of the full scaling limit of some (class of) models, which is at the same time an effective tool in computing formerly unreachable quantities of interest, and perhaps even a good starting point to extend or generalize the initial problem, then that model is definitely going to be successful.

Schramm-Loewner evolutions (briefly referred to as *SLE*) are indeed such a powerful tool. SLE is a model defined (loosely speaking) in the complex plane — it is what we would call a continuum model — which corresponds to the full scaling limit of several lattice walk models[1]. Moreover it gives access to a huge amount of information, since it is a relatively user-friendly computational framework, and its semplicity make it a fertile and solid terrain to build on. On the other hand, from a mathematician's point of view, SLE provides a framework to find rigorous proofs of conjectures and non-rigorous results obtained by physicists with other methods (e.g. CFT, field theory, Coulomb gas, mapping to other models...), it also assists in proving the very existence of some scaling limits, and their conformal invariance. Last, but not least, the rigorous nature of SLE together with its fruitful connection to CFT happily gave some common ground for theoretical physicists and mathematicians to discuss about conformal invariance related questions. It is not even to be excluded that this rigorous view on conformal invariance and CFT could be the starting point for a reformulation of field theory itself. In John Cardy's words:

> One might ask whether QFT has outlived its usefulness to generate new results, or whether (rather like string theory) it can reinvent itself in the 21st century, in a different and more powerful form — perhaps QFT as fractal geometry?

2.1.2 Overview of the model

We give here a quick overview of what SLE, intended as a statistical mechanics model, is. The remainder of the chapter is devoted to a more formal and precise explanation.

The idea behind the SLE approach to describing (measures on) curves in the complex plane has its roots in the theory of conformal maps. The strategy — first proposed in 1923 by Löwner[21] — consists in describing

[1] As will be clear in a moment, this does not mean that these models need to be in the same universality class, since SLE actually refers to a whole *family* of evolutions.

the curves through some conformal maps that encode everything about the curves themselves. Thus, instead of having some complex-valued function of time, which is the usual way to describe a parametrized curve, one works with functions taking values in the group of conformal maps. At every time, a conformal map describes the shape of the curve. How is this map defined? Let us consider the upper complex half-plane $\mathbb{H}$, and a simple[1] curve γ starting from the origin and staying in $\mathbb{H}$. Now let $\gamma[0,t]$ be the image of the curve up to time t: this is a connected set touching the real line, i.e. what will be called a *hull*[2]. We want to find a map encoding the shape of this hull. The most natural thing to do is then to map it onto some fixed standard domain. Unfortunately, this is not a sensible strategy, as far as the very existence of the map is concerned. One instead focuses on the complement of the hull $\mathbb{H} \setminus \gamma[0,t]$. This is an open simply connected set, and can be safely mapped onto the whole upper half-plane $\mathbb{H}$ by the Riemann mapping theorem. With some care in choosing the normalization, the map that does the work is unique, and can be given a name: it is the Loewner map g_t. Now, turning attention from a relatively simple object like a single curve to a much more involved entity like a conformal map does not seem a winning strategy, at first. But the beauty and power of this approach is unveiled by the Loewner theorem, which reveals how the whole conformal mapping (together with its evolution, i.e. its dependence on time t) can be described in terms of a much simpler mathematical object: a real function. In other words one completely characterizes a two-dimensional object (the curve $\gamma(t)$, for each $t \in [0,\infty]$) by means of a one-dimensional object (the so-called *driving function*). It is this "holographical" property that is at the core of Loewner evolutions and their stochastic version, SLE. Schramm–Loewner evolutions[3] put the foregoing machinery at the service of statistical mechanics. In statistical mechanics one deals with *ensembles* of curves (in the language of mathematics: with probability measures on the set of curves). The probabilistic formulation seamlessly integrates into the classical deterministic treatment. If one puts a measure on the set of driving functions one gets a measure on the curves that are described, in the Loewner formalism, by those functions. Therefore asking that certain properties be satisfied by (the measure on) the curves induces constraints on (the measure on) the driving functions. This is exactly what has been done by Schramm. He proved that if the curves have to be

[1] Actually, Loewner evolutions describe much more than simple curves. See the next paragraphs.

[2] A hull is a somewhat more general object than discussed here. See the remainder of this chapter for more precise statements.

[3] Actually, the leading S stood for *stochastic* in the seminal paper by Schramm himself, but it was soon replaced by everybody else.

conformally invariant and satisfy a conformal version of the Markov property then the driving function is constrained to be Brownian motion times a constant. This constant is conventionally chosen to be $\sqrt{\kappa}$ [1]. SLE finally reveals itself as a one-parameter family of stochastic processes taking values in the group of conformal maps.

The behaviour of SLE turns out to depend strongly on the parameter κ. Roughly speaking κ controls how fast the curve is bending. For $\kappa = 0$ the Brownian motion is actually a constant function, and the Loewner evolution (which is not stochastic in this particular case) generates straight lines. As one turns on stochasticity by increasing κ, the curves start to display wrinkles (and they do so at every scale, thanks to the self-similarity of the driving function) and they visit more and more points of the plane, by turning more and more severely: in a word, they become fractal. There are "critical" values of the parameter that separate different "phases", i.e. regions where the qualitative behaviour of the curves is different. For low enough variance of the Brownian motion ($\kappa < 4$) the curves are simple, while for large values ($\kappa \geq 8$) they visit every single point of the plane[2].

This variety gives SLE the power to describe curves and interfaces in very different statistical systems — that is, to describe a wide spectrum of physical objects.

2.2 Definitions and background

2.2.1 Measures on curves

SLE is essentially a probability measure on some well-defined set of curves.

Definition Let D be some domain of the extended complex plane $\mathbb{C}^*$. A *curve* in D is a continuous map γ: $[0, \infty] \longrightarrow D$. We say that γ *starts* at $\gamma(0)$ and *ends* at $\gamma(\infty)$.

Actually, we will always be interested in curves as equivalence classes of parametrized curves, that is we shall not distinguish between curves that can be obtained from one another by a monotonic change of parametrization. Essentially, this means that one focuses on the *support* of the curve. This is true for *simple* (i.e. injective) curves — up to an overall orientation sign —, but the requirement of monotonicity distinguishes non-simple curves by the

[1] Notice that the letter under the square root is a Greek κ, not the Latin k.

[2] Of course, these properties hold *almost surely* with respect to the SLE measure. Alternatively, the partition function restricted to those curves for which these properties do not hold is zero.

orientation of each of their loops. The reason for this choice will hopefully become clear in the forthcoming.

It is very natural to start by considering simple curves, as we did in the informal description of the model, in section 2.1. In fact, we are going to do so also in section 2.3, where a heuristic argument will be proposed, to justify the definition of the SLE equation itself. Nonetheless, SLE will turn out to describe a more general class of objects (one to which some non-simple curves belong as well)[1]. Therefore, simplicity of the curves is not to be understood in the following statements.

We shall consider *probability measures* on some sets of curves, i.e. measures with total mass equal to 1, and we will stick to curves living in simply connected regions, since multiply connected domains are still very young in the SLE literature. Actually, since we are interested in the conformal properties of the physical models (the continuum limits of the lattice models), we also have to add information about the way these measures change when a conformal transformation of the complex plane is performed. Moreover, topological arguments and intuition from conformal theory suggest to distinguish between curves that start and end at *interior* (bulk) or *boundary* points of the domain. Altogether, the measures and all the information we need to know about them (how they transform and the topology of the curves they are supported on) will be called *processes* or *evolutions*[2]. These considerations justify the following

Definition A *chordal process* is a collection of probability measures $\mu(D, z, w)$, one for each choice of (D, z, w), where D is a simply connected domain ($\neq \mathbb{C}$) and z and w are two points on its boundary, over the set of all curves defined on the closure of D that start at z and end at w.

Definition A *radial process* is a collection of probability measures $\mu(D, z, w)$, one for each choice of (D, z, w), where D is a simply connected domain ($\neq \mathbb{C}$), z is a point on its boundary and w a point in its interior, over the set of all curves defined on the closure of D that start at z and end at w.

Notice that the foregoing definitions do not exhaust all possible ensembles of curves, since for instance an interior→interior path is not taken into account. More subtly, also interior→exterior paths are not considered, since as far as

[1] We will discuss some intuition regarding this more general class of curves in the following.

[2] The former stems from the mathematical formulation of stochastic processes, while the latter is suggested by the "dynamical" description that naturally comes up in the SLE formalism.

our previous definition goes we are treating *oriented* curves[1]. This issue becomes apparent when trying to define (section 2.7) and simulate (section 3) SLE on the whole plane.

2.2.2 Conformal maps

Conformal mappings lie at the very heart of the whole SLE industry. We informally recall that a conformal map is defined on $\mathbb{R}^2$ as a differentiable map which preserves angles. An important theorem of complex analysis states that a map from an open subset of the complex plane D to another open subset D' is conformal if and only if it is a one-to-one, onto, analytic function of D to D'. Now, this (almost–) equivalence between conformal maps and analytic functions in two dimensions has an enormous power. Informally, this means that one has infinite degrees of freedom in choosing a conformal map (more precisely: the conformal group is infinite-dimensional in two dimensions). This high versatility is quantified by the following, most useful

Theorem 1 (Riemann mapping theorem) *Let z be an internal point of a simply connected region $D \neq \mathbb{C}$. Then there is a unique conformal transformation f of D into the unit disc $\mathbb{D}$ such that $f(z) = 0$ (z is mapped to the origin) and $f'(z) > 0$ (the derivative in z is real and positive).*

As a corollary, any two simply connected domains are conformally equivalent, i.e. there is at least one conformal map between them[2].

The Riemann theorem guarantees existence and uniqueness of the mapping, provided one fixes a special point to be sent to the origin. Actually, given two simply connected domains D and D', one can always write a conformal mapping f between them as a composition of two mappings ϕ_D and $\phi_{D'}^{-1}$ that have the unit disc $\mathbb{D}$ as co-domain and domain respectively:

$$\begin{array}{ccccc} & & \phi_D & & \phi_{D'}^{-1} & \\ D & \longrightarrow & \mathbb{D} & \longrightarrow & D' \end{array} \tag{2.1}$$

If one fixes these two maps, then one sees that f is defined modulo an automorphism of the disc. Since we will be interested in defining such a conformal map for domains in the half plane in a unique way, some normalization property must be asked.

[1] The issue of *reversibility* is still object of research among mathematicians studying SLE.

[2] There are other versions of this theorem, for example when one wants the map to be supported also on the boundary of the domain (and this particular case is interesting in that it shows how conformal maps between two given domains have "three real degrees of freedom"). See for instance [22] for formal statements and proofs.

Definition A bounded subset A of $\mathbb{H}$ is a *compact* $\mathbb{H}$*-hull* if $A = \mathbb{H} \cap \bar{A}$ and $\mathbb{H} \setminus A$ is simply connected.

Essentially, a compact $\mathbb{H}$-hull is a compact set touching the real axis and not disconnecting any point from infinity. With this definition, a very useful corollary of the Riemann theorem states existence *and* uniqueness of the conformal map:

Theorem 2 *If A is a compact $\mathbb{H}$-hull then there is a unique conformal map $g_A : \mathbb{H} \setminus A \longrightarrow \mathbb{H}$ such that*

$$\lim_{z\to\infty} (g_A(z) - z) = 0. \tag{2.2}$$

The choice that g_A behave as the identity near infinity is called *hydrodynamic normalization*[1]. Such a map is called *uniformizing*. Its uses are manifold. It is used on a daily basis for technological applications, since it permits one to solve an originally complicated Laplace problem in much simpler geometries. For instance, if A (together with $\mathbb{R}$) is a charged conductor, then g_A greatly helps in determining the electrical field in the rest of $\mathbb{H}$.

Having chosen a standard domain ($\mathbb{H}$) and a normalization, we now have a canonical map from the set of compact $\mathbb{H}$-hulls to the group of conformal mappings. In other words, we are describing a hull A through its *uniformizing* map g_A. Let us take a look at the Laurent expansion of a uniformizing map g around infinity:

$$g(z) = z + \sum_{n=1}^{\infty} \frac{b_n}{z^n} \tag{2.3}$$

Since the map has to be the identity at infinity, the first coefficient must be 1 (no rescaling) and the second has to be 0 since we are not allowing for translations. A property of hulls that can be defined by means of the foregoing correspondence is the half-plane capacity:

Definition Let A be a compact $\mathbb{H}$-hull and g_A its uniformizing map. The *half-plane capacity* of A is the coefficient of $1/z$ in the Laurent expansion of g_A. It will be denoted $\mathrm{hcap}(A)$.

The capacity is a measure of the conformal size of the hull, "as seen from infinity". In the application to electrostatics, the coefficients of the Laurent series are the multipole moments of the charged hull (along with its mirror image with respect to $\mathbb{R}$); the half-plane capacity is the electric dipole moment. More precisely, capacity satisfies the following properties (the proofs are elementary):

[1] If one considers g as describing one time-step of the evolution of a 2-dimensional fluid, then the normalization means the fluid does not move at infinity.

- If $A_1 \subsetneq A_2$ then $\mathrm{hcap}(A_1) < \mathrm{hcap}(A_2)$.
- $\mathrm{hcap}(A + x) = \mathrm{hcap}(A), \quad x \in \mathbb{R}$.
- $\mathrm{hcap}(rA) = r^2\,\mathrm{hcap}(A), \quad r \geq 0$.

Since we will be needing it at the end of this Chapter, when defining the whole-plane version of SLE, we introduce here the concept of a ($\mathbb{C}$)-hull:

Definition A *compact hull* is a connected compact subset of $\mathbb{C}$ which contains more than one point and such that its complement in $\mathbb{C}$ is connected.

The Riemann mapping theorem is very directly applied to such a domain, and the corresponding notion of capacity can be defined. We will do so in Section 2.7.

Now we introduce two properties (both in contact with the conformal nature of the formalism we are building on) that our processes will be required to satisfy.

Definition A (chordal or radial) process $\mu(D, z, r)$ is *conformally invariant* if

$$f \circ \mu(D, z, w) = \mu(D', f(z), f(w))$$

for every conformal transformation of D into D'. (Here, $f \circ \mu$ denotes the image of the measure μ under f).

Definition Let γ be "split" into two disjoint parts γ_1, starting from z and ending in ζ, and γ_2, starting from ζ and ending in w. A (chordal or radial) process satisfies the *domain Markov property* if

$$\mu_{|\gamma_1}(D, z, w) = \mu(D \setminus \gamma_1, \zeta, w)$$

where $D \setminus \gamma_1$ is the complement of the support of γ_1 in D, and $\mu_{|\gamma_1}(D, z, w)$ is the conditional measure on γ_1, i.e. the measure $\mu(D, z, w)$ restricted to those γ's that agree with γ_1 from z to ζ, divided by their total mass[1].

Let us briefly discuss their meaning. That of conformal invariance in physical systems is a concept that dates back to the Eighties, when its role in quantum field theory was explored (see [23] for a review). Conformal invariance happens to have a very important role in statistical mechanics too,

[1]Sometimes the process is said to be *domain Markov covariant*. The term *covariance* is used to state equivalence of two measures up to a multiplicative factor, in this case the mass of all curves agreeing with γ_1.

since (almost all) systems on their critical manifolds possess wider invariance properties than the sole global scale and rotational symmetries. Actually, they display invariance under *local* rescaling and rotation. The first and simplest walk model that was known to be conformally invariant was the scaling limit of the lattice random walker: the Brownian motion. The starting lattice model clearly has a much narrower symmetry group, since the underlying lattice itself is invariant only under a discrete set of rotations. But the magic of criticality here is that it organizes the microscopic degrees of freedom in such a way that the scaling limit has a much broader symmetry group: Brownian motion transformed through a conformal map "looks the same" as Brownian motion in the transformed geometry. Putting a magnifying lens over a small portion of a Brownian path does not change the (statistical) properties of the whole path. The application of Conformal Field Theory methods to statistical mechanics has helped theoreticians to derive a wealth of new exact results and gain more in-depth knowledge of many models and the nature of phase transitions themselves (see [24]).

The second property, that of domain Markov invariance, is much less ubiquitous. Its definition was first proposed in the seminal paper by Schramm[25], for the purpose of formulating precisely what stochastic version of the Loewner evolution was to be reached for. It was chosen as a sensible property to require, since a lattice version of it holds for many walk models (such as the loop-erased random walk — which is the original model addressed by Schramm —, the self-avoiding walk, the percolation exploration process, etc. See section 2.6). This is a very natural generalization of the usual Markov property, which clearly does not hold for any interesting walk model, apart from the plain random walk. While Markov property asks the process not to "remember its past", the domain Markov property states that the evolution of the curve *can* indeed depend on its past, but only through a restriction of its domain: the path already travelled is not distinguishable from the boundary.

2.2.3 Loewner equation

With all the definitions in the previous paragraphs we are ready to put everything together. Recall the key idea of Loewner evolutions: describing a parametrized curve by the evolution of the normalized conformal maps

$$g_t : \mathbb{H} \setminus \gamma[0,t] \longrightarrow \mathbb{H}. \tag{2.4}$$

In particular, one focuses on the image of the tip of the curve, that is on $U_t = g_t(\gamma(t))$. As we said, we will first consider simple curves. The follow-

ing theorem says that g_t satisfies a differential equation, known as *Loewner equation*.

Theorem 3 (Loewner equation) *Let γ be a simple curve in $\mathbb{H}$ (parametrized by t) starting at the origin, such that its half-plane capacity $hcap(t)$ is C^1 and goes to infinity for large t. Let g_t be the unique conformal map of $\mathbb{H} \setminus \gamma[0,t]$ onto $\mathbb{H}$ with the hydrodynamic normalization, and let $U_t = g_t(\gamma(t))$. Then*

$$\dot{g}_t(z) = \frac{\frac{d}{dt} hcap(t)}{g_t(z) - U_t}. \tag{2.5}$$

Notice that by definition $g_0(z) = z$. Even when $\mathrm{hcap}(t)$ is not C^1 it can be shown to be strictly increasing and continuous (even for non-simple curves). It is then always possible to gauge $\mathrm{hcap}(t) = 2t$ through a change of parametrization, thus obtaining the canonical form of the Loewner equation

$$\dot{g}_t(z) = \frac{2}{g_t(z) - U_t}. \tag{2.6}$$

The function U_t is called *driving function*. It is real-valued, since the tip of the curve lies on the boundary of $\mathbb{H} \setminus \gamma$, and has then to be mapped to the boundary of $\mathbb{H}$, which is $\mathbb{R}$.

Now, let us discuss some intuition about simplicity of the curves. The driving function can be proved to be continuous for simple curves, but actually it is continuous for a broader set of curves. The lattice models we will consider all give rise to strictly self-avoiding lattice walks (polymers). This fact alone does not at all imply that the measure in the scaling limit be supported on simple curves (by being supported on simple curves we mean that the set of non-simple curves has null measure). In fact, while this is true for instance for the (supposed) scaling limit of the SAW, continuum curves describing collapsed dense polymers do have double contacts, and they do so with probability one. Intuitively, this is due to the fact that when the lattice size goes to zero loops can actually close in the limit, and then the almost-sure simplicity depends on how the weights of large loops scale in this limit. Yet, there are two things that can not happen: the curve can not *cross* itself, and it can not enter a region which has been disconnected from infinity (the inside of a loop). In words, this simply means that when it touches itself it "bounces off" immediately. In terms of conformal maps this property has a much more precise characterization. Imagine a portion of a curve that is close to forming a loop, as in Figure 2.1. Let us call z^+ and z^- the right and left limits to the contact point z and consider the action of the conformal map g_γ that maps $\mathbb{H} \setminus \gamma$ onto $\mathbb{H}$. This map sends z^+ and z^- to

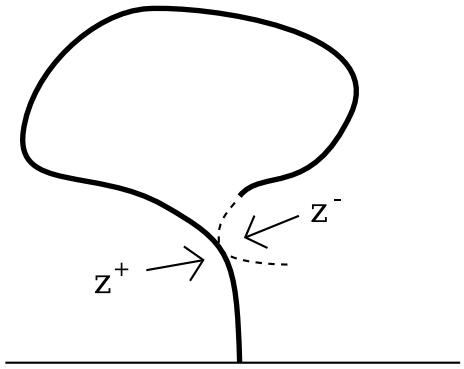

Figure 2.1: A loop is going to close. z^+ and z^- are the right and left limits to the intersection point respectively.

two different points on the real axis. If at time t the curve has not yet closed the loop, the image of the end-point will be close to $g_\gamma(z^+)$. First of all, if after hitting itself the curve enters the region inside the loop, the tip will not be mapped onto $\mathbb{R}$ anymore, because it is no longer on the boundary of the domain. But if at time $t + \delta t$ the curve has *crossed* itself, the tip will be then mapped somewhere near $g_\gamma(z^-)$. Thus, such a crossing would probably break continuity of the driving function. So one sees that the continuity of U_t prevents the curve from passing "from one side to the other" of itself.

The foregoing reasoning suggests that if one goes the other way around than theorem 3, by assuming some continuous function U_t and then studying the solutions to the Loewner equation, one is not going to get simple curves. This inverse problem (which is the relevant one for our purposes) is defined in the following way. Let us consider equation (2.6) for a continuous real-valued function U_t, with initial condition $g_0(z) = z$ (which means that the growing hull starts from being a subset of the real axis). The denominator in (2.6) can go to zero for a fixed point z, causing the solution to fail to exist after some finite time. Let us call this time (which depends on z) T_z, if it exists; otherwise let us set $T_z = \infty$. Then the growing hull is defined as the complement of the domain of the solution at time t:

$$K_t = \{z \in \mathbb{H} : T_z \leq t\}. \tag{2.7}$$

It is the set of all points "swallowed" by the evolution up to time t. The *trace* of the evolution is of course defined as $\gamma_t = g_t^{-1}(U_t)$, and it is the curve such that the domain $\mathbb{H} \setminus K_t$ of g_t is the unbounded component of $\mathbb{H} \setminus \gamma[0, t]$. One says that the evolution is *generated* by γ.

We conclude this paragraph by discussing some intuition about the composition of partial Loewner maps, which will be useful in the forthcoming,

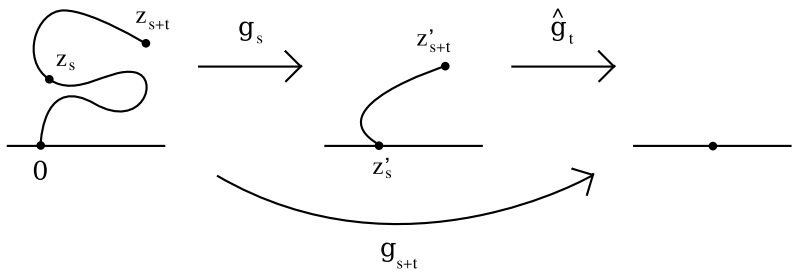

Figure 2.2: The Loewner map g_{s+t} as a composition of an earlier Loewner map with the incremental map $\hat{g}_t$.

especially when considering how domain Markov covariance translates into a statistical property for the driving function.

Imagine we have grown a hull for a time $s + t$ (refer to Figure 2.2 for a sketch). Let us suppose it is a simple curve, and let us divide it in two parts, the first from the origin to z_s and the second from z_s to z_{s+t}. The uniformizing map of the whole curve g_{s+t} can be thought of as acting in two stages: a first map g_s swallowing the curve up to point z_s, and a second map $\hat{g}_t$ swallowing the image under g_s of the remainder of the curve (from z'_s to z'_{s+t}). The hat in $\hat{g}_t$ is to remind that this map does not necessarily satisfy Loewner equation with the same driving function as g. By uniqueness of the maps (that is, commutativity of the diagram in figure),

$$g_{s+t} = \hat{g}_t \circ g_s \;\Rightarrow\; \hat{g}_t = g_{s+t} \circ g_s^{-1} \tag{2.8}$$

Since g_{s+t} satisfies Loewner equation with driving function U_{s+t}, we have

$$\frac{d}{dt}\hat{g}_t(z) = \frac{d}{dt} g_{s+t} \circ g_s^{-1}(z) = \frac{2}{g_{s+t} \circ g_s^{-1}(z) - U_{s+t}} = \frac{2}{\hat{g}_t(z) - U_{s+t}} \tag{2.9}$$

from where one recognizes the function that drives the Loewner evolution of the partial map $\hat{g}_t$: $\hat{U}_t = U_{s+t}$. Of course, one also have to check that the initial condition for the differential equation is satisfied, but this is straightforward, since setting $t = 0$ in (2.8) yields $\hat{g}_0(z) = z$.

2.3 Heuristic argument

As we said earlier in this chapter, the idea that led to the formulation of SLE was that of incorporating the stochastic nature of random curves directly into the Loewner formalism. Every constraint one puts on the process (every property required of it) propagates into a corresponding property for the

driving function. For SLE, we will require the processes to satisfy conformal invariance and domain Markov covariance. Moreover, a very natural property will be required as well, since it is satisfied by almost every statistical mechanical system: that of reflection invariance, that is invariance under the transformation $z \to -z^*$, which is not conformal. These constraints can be seen to lead to a very strong characterization of the driving process: it has to be a rescaled Brownian motion.

We will present here the chordal version of the original argument by Schramm. The same exact reasoning can be applied to other versions of SLE, like the important (for our purposes) radial case.

Suppose we have a random family of *simple* curves starting at the origin and staying in the upper half-plane. Let us consider one such curve γ parametrized in such a way that $\mathrm{hcap}(\gamma[0,t]) = 2t$, and suppose the probability measure is both conformal invariant and domain Markov covariant. We fix a time T and condition the curve on $\gamma[0,T]$, that is, on its past up to time T. Let g be the Loewner uniformizing map that sends $\mathbb{H} \setminus \gamma[0,T]$ onto $\mathbb{H}$ (with the hydrodynamic normalization). Of course this map completely swallows the first part of the curve, sending it to the real axis. Now consider what happens to the rest of the image of the curve: $\gamma[T, T+t]$ is a curve that starts at U_T. From time T on, γ lives in $\mathbb{H} \setminus \gamma[0,T]$, and by Markov property it has there the same distribution as γ conditioned on $\gamma[0,T]$. But now, by conformal invariance, this means that this distribution is the same as that of γ itself. Therefore, if we translate the curve $g(\gamma[T, T+t])$ so that it starts at the origin, the two properties imply that it has the same distribution as the original random curve, and it is independent of $\gamma[0,T]$. Now let us take two curves γ_1 and γ_2, both picked up according to the same ensemble, the definition of which is the goal of this paragraph. Let g_t^1 and g_t^2 be their uniformizing maps at time t, and U_t^1 and U_t^2 their driving functions. We construct a curve $\hat{\gamma}$ by chaining these two curves as follows. For $t \leq T$, $\hat{\gamma}(t)$ is just $\gamma^1(t)$. For $t > T$, it is the pre-image of γ^2 under g_T^1, that is the uniformizing map of the *first* curve, evaluated at the cutting time T. Of course, one has to perform a shift in time — in order to let $\hat{\gamma}(T+t)$ correspond to $\gamma^2(t)$ — and a shift in space — in order to have the pre-image start where the first part of the curve ends, so that the two join continuously. One therefore considers

$$\hat{\gamma}(t) = \begin{cases} \gamma^1(t) & \text{for } t \leq T \\ (g_T^1)^{-1}(\gamma^2(t-T) + U_T^1) & \text{for } t > T. \end{cases} \tag{2.10}$$

Notice that since γ^2 is constrained to stay strictly in the upper half-plane, its pre-image under g_T^1 is ensured not to hit $\gamma^1[0,T] = \hat{\gamma}[0,T]$, since the pre-image of the latter set is a subset of the real axis. So $\hat{\gamma}(t)$ is a simple curve

starting at the origin and staying in the upper half-plane for all $t \geq T$. The property discussed earlier — consequence of conformality and Markovianity — then says that $\hat{\gamma}$ has the same distribution as γ^1 and γ^2. Let us then call $\hat{g}_t$ the uniformizing map of $\hat{\gamma}[0,t]$ and $\hat{U}_t$ its driving function. We have

$$\hat{g}_t^2(z) = g_{t-T}^2(g_T^1(z) - U_T) + U_T \tag{2.11}$$

which, by differentiating with respect to t, yields

$$\dot{\hat{g}}_t(z) = \frac{2}{g_{t-T}^2(g_T^1(z) - U_T^1) - U_{t-T}^2} = \frac{2}{\hat{g}_t(z) - U_T^1 - U_{t-T}^2}. \tag{2.12}$$

One can then recognize in this formula the driving function $\hat{U}_t$ as $U_T^1 + U_{t-T}^2$. Since $\hat{U}_T = U_T^1$, one can write $\hat{U}_t - \hat{U}_T = U_{t-T}^2$. This implies that $\hat{U}_t - \hat{U}_T$ is independent of $\hat{U}_s$ for $s \leq T$ and the distribution of this increment does not depend on T. What this means is that the process $\hat{U}_t$, which is what we are trying to characterize, has *independent* and *stationary* increments.

Now, let us ask one more property for the probability measure. Let us suppose that the measure is such that γ and $-\gamma^*$ (which is the reflection of γ against the imaginary axis) have the same distribution. The uniformizing map of the reflected curve is just $-g_t^*$, whose driving function is simply $-U_t$. Then, U_t and $-U_t$ have the same distribution, that is the mean of the process has to be zero for all t. The only one dimensional continuous process with stationary, independent increments and mean zero is the Brownian motion. Its variance is not fixed by the constraints we chose, so we can take it to be the square of any positive number. Finally one ends up with the SLE_κ equation

$$\dot{g}_t(z) = \frac{2}{g_t(z) - \sqrt{\kappa} B_t}, \quad g_0(z) = z \tag{2.13}$$

where B_t is standard unit variance one-dimensional Brownian motion.

Let us note here in passing that the first more natural generalization that comes into mind is the extension to more general classes of driving processes, which is to say, relaxation of the constraints. Some work has been done in the past years about SLE processes driven by Levy flights. In this particular case, the hull turns out not to be necessarily generated by a curve. The interested reader can find advances in [26] and the references therein.

2.4 Some properties

2.4.1 Phases

We have seen that SLE_κ naturally depends on a real parameter: the variance of the driving Brownian motion. We saw in last section that whether the

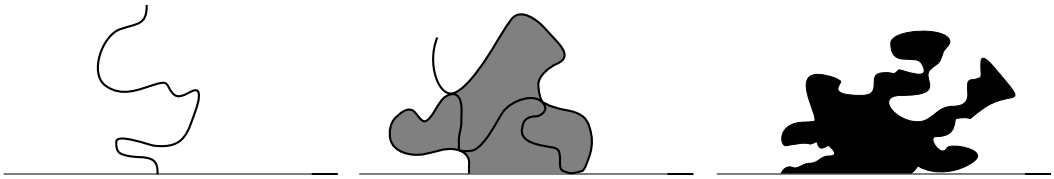

Figure 2.3: A sketch of how the three phases of SLE look like. Left: $\kappa \leq 4$; center: $4 < \kappa < 8$; right: $\kappa \geq 8$. Grey-shaded regions indicate points that belong to the hull but not to the trace.

curves generated are simple depends on the smoothness of the driving function. Actually, SLE happens to be right on the boundary between simple and non-simple curves, since Brownian motion sits right on the line between "smooth" and "not smooth enough" processes. In fact, the behaviour of the curves changes qualitatively as well as quantitatively while the parameter κ is changed [27]. There happen to be (at least) three *phases*[1] with different global behaviour. Three instances of SLE are plotted in Figure 2.4.1 for values of κ belonging to the three different phases.

- $\kappa \in [0, 4]$. The SLE trace γ in this regime is almost surely a simple path. Moreover, since by conformal Markov covariance the role of the boundary is the same as the support of the curve, the trace almost surely does not hit the real line and stays in the upper half-plane after time 0. As a consequence, the hulls K_t coincide with the trace itself.

- $\kappa \in (4, 8)$. The trace is no longer simple for $\kappa > 4$: every point belonging to $\mathbb{H} \setminus \{0\}$ almost surely becomes part of the hull in finite time. This means that every point eventually gets swallowed, either because it is on the trace or because it is disconnected from infinity by the trace. In this phase, that is for $\kappa < 8$, the former happens with probability zero: the trace swallows the entire half-plane in blobs, but touches itself only a few times. The trace is not dense but nonetheless every $z \in \overline{\mathbb{H}} \setminus \{0\}$ becomes part of the hull in finite time.

- $\kappa \geq 8$. In this regime the trace becomes dense in the half-plane. With probability one $\gamma[0, \infty) = \overline{\mathbb{H}}$. The hulls coincide again with the trace.

[1] Here, the terms "phase", "phase transition" and "critical point" are used with a loose meaning, without any connection to the formal theory of criticality in statistical mechanics. They stand to underline the sharpness of the transitions, with different properties holding in the different phases.

2.4.2 Fractal dimension

Of course, one of the first very important properties of a random curve one wants to study is its fractal dimension. Roughly speaking, the fractal dimension is a measure of how "dense" the curve is. A line has fractal dimension 1, and a space-filling curve has the dimension of the embedding space, in this case 2. For fractal objects living in-between these two extremes, one wants to look closer and closer to the curve and see how completely it appears to fill space. Of course one could do this also in the opposite limit, that is by looking at larger and larger sections of the object, but the fractal dimension is a *local* quantity. The possible definitions are manifold. We will use the following

Definition Let $\mathcal{A}$ be a subset of the plane. Let $N(\epsilon)$ be the minimum number of discs of radius ϵ required to cover $\mathcal{A}$. Then if $N(\epsilon) \sim \epsilon^{-d_f}$ as $\epsilon \to 0$, d_f is called the *fractal dimension* of the set $\mathcal{A}$.

Of course, different samples of a random process will in general have different fractal dimensions. Nonetheless, it will turn out that *almost all* SLE samples (for a fixed value of the parameter κ) will have the same d_f. In order to calculate it, we rely on a property of random curves which is very closely related to the fractal dimension. Let us define $P(x, y, \epsilon)$ as the probability that a given point $z = x + iy$ lies within a distance ϵ of the curve γ. Its scaling behavior is expected to be of the form

$$P(x, y, \epsilon) \sim \epsilon^{2-d_f} f(x, y) \quad \text{as } \epsilon \to 0 \tag{2.14}$$

P can be calculated in the SLE framework by deriving a differential equation for it. Let us consider the action of the infinitesimal Loewner map at time 0

$$dg : z \mapsto z + \frac{2}{z} dt \tag{2.15}$$

on a curve γ going from 0 to ∞. Under this map the point z and the distance from the curve ϵ scale as

$$\begin{aligned} x &\mapsto x + \frac{2x}{x^2 + y^2} \\ y &\mapsto y - \frac{2y}{x^2 + y^2} \\ \epsilon &\mapsto |\partial_z dg(z)|\, \epsilon \sim \epsilon - \frac{2(x^2 - y^2)}{(x^2 + y^2)^2} \epsilon \end{aligned} \tag{2.16}$$

and at the same time the origin gets mapped to $\sqrt{\kappa} dB$. The probability $P(x, y, \epsilon)$ has to be equal to the sum over all possible realizations of the

Brownian motion of the probability in the transformed geometry, that is $P(x' - \sqrt{\kappa}dB, y', \epsilon')$, where the translation in x sends $\sqrt{\kappa}dB$ back to the origin. One then obtains the "master equation"

$$P(x, y, \epsilon) = \left\langle P(x' - \sqrt{\kappa}dB, y', \epsilon') \right\rangle_{dB}. \tag{2.17}$$

By expanding at first order in dt, remembering that $\langle dB \rangle = 0$ and that by Itō calculus $\langle dB^2 \rangle = dt$, one finally obtains the following PDE:

$$\left(\frac{2x}{x^2+y^2}\partial_x - \frac{2y}{x^2+y^2}\partial_y + \frac{\kappa}{2}\partial_x^2 - \frac{2(x^2+y^2)}{(x^2+y^2)^2}\epsilon\partial_\epsilon \right) = 0. \tag{2.18}$$

The ansatz $P = \epsilon^{2-d_F} y^\alpha (x^2+y^2)^\beta$ satisfies the equation with $\alpha = (\kappa-8)^2/8\kappa$, $\beta = (\kappa-8)/2\kappa$ and

$$d_f = 1 + \frac{\kappa}{8} \tag{2.19}$$

which is then (with probability 1; see [28] for details) the fractal dimension of SLE curves, as far as $\kappa \leq 8$. For $\kappa > 8$ the equation admits a solution with $d_f = 2$, which is of course the expected fractal dimension for space-filling curves.

We mention here an important conjecture due to Duplantier [29]. For $\kappa > 4$ the curve is not simple, but the *frontier* of the hull is by definition simple. The conjecture states that *locally* this curve is $\mathrm{SLE}_{\tilde{\kappa}}$, with

$$\tilde{\kappa} = \frac{16}{\kappa} \tag{2.20}$$

. Under this duality, the fractal dimension d_f goes to

$$\tilde{d_f} = 1 + \frac{2}{\kappa}. \tag{2.21}$$

For example, the frontier of a percolation cluster and a self-avoiding walk are locally the same in the scaling limit.

2.5 Connection to CFT

SLE as we described it in the foregoing sections is a measure on curves satisfying conformal invariance. Of course, when the conformal transformations belong to the symmetry group of a problem, the tool of choice for a theoretical physicist is *conformal field theory* (CFT). A description of CFT is widely out of the scope of this thesis; we refer the reader to the extensive literature on the subject [30].

It is very natural to try and find a connection between SLE and CFT. This can be done in several ways [31, 32, 16]. We will present here the original approach by Bauer and Bernard, and supplement it later with ideas by Cardy.

Let us consider the Virasoro algebra — which is the (unique) central extension of the Lie algebra of conformal transformations —, generated by $\{L_n\}_{n\in\mathbb{Z}}$, satisfying the commutation relations

$$[L_n, L_m] = (n-m)L_{n+m} + \frac{c}{12}(n-1)n(n+1)\delta_{n+m,0} \tag{2.22}$$

Recall from general CFT that the action of the Virasoro generators on a primary field of weight Δ is

$$[L_n, \phi_\Delta(z)] = \left[z^{n+1}\partial_z + (n+1)\Delta z^n\right]\phi_\Delta(z) \tag{2.23}$$

Connection with SLE is established through the so-called *lifted* process, which is a random walk on the Virasoro group — obtained by formal exponentiation of the elements of the algebra —, defined as

$$d(\log \mathcal{G}) \equiv \mathcal{G}_t^{-1} d\mathcal{G}_t = -2L_{-2}\, dt + L_{-1}\, d\xi_t, \tag{2.24}$$

where $\mathcal{G}_t$ is an element of the group and $\xi_t = \sqrt{\kappa}B_t$. The initial condition for the differential equation is $\mathcal{G}_0 = 1$, which corresponds to the identical conformal map. Equation (2.24) describes the flow of a family of elements of the Virasoro group. As such, it is possible to study its action on conformal primary fields ϕ_Δ. By definition of primary field one has

$$\mathcal{G}_t^{-1}\phi_\Delta(z)\mathcal{G}_t = \left(\partial_z g_t(z)\right)^\Delta \phi_\Delta\left(g_t(z)\right), \tag{2.25}$$

where g_t is the conformal transformation induced by $\mathcal{G}_t$. We want to derive a differential equation for g_t. In order to do so, let us differentiate both sides of Equation (2.25). By using the identities

$$\begin{aligned} \mathcal{G}_t^{-1}\mathcal{G} &= \mathbb{I} \\ \frac{d}{dt}\mathcal{G}_t^{-1}\mathcal{G} &= 0 \end{aligned} \tag{2.26}$$

the left-hand side yields

$$\frac{d}{dt}\left(\mathcal{G}_t^{-1}\phi_\Delta(z)\mathcal{G}_t\right) = \left[\mathcal{G}_t^{-1}\phi_\Delta(z)\mathcal{G}_t\ ,\ \mathcal{G}_t^{-1}\frac{d}{dt}\mathcal{G}_t\right] \tag{2.27}$$

The commutator is easily evaluated by using the intertwining relations (2.23), the definition of the lifted process (2.24) and the scaling form (2.25):

$$\begin{aligned}\frac{d}{dt}\left(\mathcal{G}_t^{-1}\phi_\Delta(z)\mathcal{G}_t\right) &= (\partial_z g_t(z))^\Delta \left[\phi_\Delta\left(g_t(z)\right)\ ,\ -2L_{-2}+L_{-1}\frac{d\xi_t}{dt}\right] \\ &= (\partial_z g_t(z))^\Delta \left[\Omega^{(1)}\ \frac{\partial_z}{\partial_t g_t(z)} -\ \Omega^{(0)}\ \right]\ \phi_\Delta\left(g_t(z)\right),\end{aligned} \tag{2.28}$$

where

$$\begin{aligned}\Omega^{(1)} &= \left(\frac{2}{g}-\frac{d\xi_t}{dt}\right) \\ \Omega^{(0)} &= \frac{2\Delta}{g_t^2(z)}.\end{aligned} \tag{2.29}$$

The differentiation of the right-hand side of Equation (2.25) instead gives

$$\frac{d}{dt}\left(\mathcal{G}_t^{-1}\phi_\Delta(z)\mathcal{G}_t\right) = (\partial_z g_t(z))^\Delta \left[\tilde{\Omega}^{(1)}\ \frac{\partial_z}{\partial_t g_t(z)} -\ \tilde{\Omega}^{(0)}\ \right]\ \phi_\Delta\left(g_t(z)\right), \tag{2.30}$$

with

$$\begin{aligned}\tilde{\Omega}^{(1)} &= \dot{g}_t(z) \\ \tilde{\Omega}^{(0)} &= \Delta\frac{\partial_z\dot{g}_t(z)}{\partial_z g_t(z)}.\end{aligned} \tag{2.31}$$

Equating the differentials of both sides of Equation (2.25) finally yields

$$\begin{aligned}\Omega^{(1)} &= \tilde{\Omega}^{(1)} \\ \Omega^{(0)} &= \tilde{\Omega}^{(0)}\end{aligned} \tag{2.32}$$

which read

$$\begin{aligned}\dot{g}_t(z) &= \frac{2}{g_t(z)}-\frac{d\xi_t}{dt} \\ \partial_z\dot{g}_t(z) &= -\frac{2}{g_t^2(z)}\partial_z g_t(z).\end{aligned} \tag{2.33}$$

The first equation is immediately recognized as the chordal SLE equation, by substituting $g_t(z) \to g_t(z) - \xi_t$. The second equation is simply the space derivative of the first.

One could have also gone the other way around. Following Cardy [16], one can define what a *curve* state $|\gamma_t\rangle$ is in (boundary) CFT by restriction of

the path integral. The representation of the conformal group on the Hilbert space of states is realized through insertion of line integrals of the stress-energy tensor $T(z)$. For instance, the action of the infinitesimal translated Loewner map $dg_t(z) = 2dt/z - d\xi_t$ corresponds to inserting $(1/2\pi i) \oint (2dt/z - d\xi_t)T(z)dz$. With the usual definition

$$L_n = \frac{1}{2\pi i} \oint z^{n+1} T(z)\, dz \tag{2.34}$$

one can see that in operator notation the state $|\gamma_t\rangle$ transforms as

$$|dg(\gamma_t)\rangle = \mathbf{T} \exp\left(\int_0^t (2L_{-2}d\tau - L_{-1}d\xi_\tau) \right) |\gamma_t\rangle \tag{2.35}$$

where $\mathbf{T}\exp$ denotes a time-ordered exponential. Now, integrating $|\gamma_t\rangle$ with the measure induced by the restriction of the path integral yields a unique state $|h\rangle$ which does not depend on time. This state turns out to be the state corresponding to a boundary condition changing operator at the origin: it is the state obtained by conditioning the path integral on the existence of one curve going from the origin to ∞. $|h\rangle$ is then invariant under the action of the conformal map, so one can integrate Equation (2.35) over all realizations of the Brownian motion, using Itō calculus, and finally find

$$\left(2L_{-2} - \frac{\kappa}{2} L_{-1}^2\right) |h\rangle = 0 \tag{2.36}$$

which means that the Virasoro representation corresponding to $|h\rangle$ has a null state at level 2. From this condition, by acting with L_1 and L_2 to extract the central charge, it is then easy to find

$$c = \frac{(3\kappa - 8)(6 - \kappa)}{2\kappa} \tag{2.37}$$

which relates SLE with parameter κ and CFT with central charge c. Notice that as expected percolation ($\kappa = 6$) and the SAW ($\kappa = 8/3$) correspond to $c = 0$. Also notice that the dual partners κ and $16/\kappa$ yield the same c.

2.6 Identification with lattice models

Schramm-Loewner evolutions are interesting mathematical objects *per se*. Yet they become powerful tools for the physicist when they are used in the context of statistical mechanics. A wealth of lattice models are proved or supposed to have some SLE_κ as their scaling limits. Even more models —

while not being described by a *single* curve — do display SLE-like properties when looked at from the right perspective, that is, when the right observable has been chosen. It turns out that a multitude of statistical systems at their critical points "generate" SLE's, ranging from the obvious polymeric models, to interfaces in statistical systems, spin-glasses and even out of equilibrium phenomena like turbulent flow. We will focus here on some of the lattice walk models presented in Chapter 1, namely the self-avoiding walk and the critical percolation explorer.

The SLE machinery permits straightforward proofs of convergence for some lattice models. One just follows the most natural way. Imagine embedding the lattice — at finite mesh size a — in the complex plane $\mathbb{C}$, and consider a lattice curve $\tilde{\gamma}_a(t_i)$, $i = 0, 1, \ldots, \infty$. The discrete parametrization $t_0, t_1, \ldots$ can be uniquely extended to continuous time $t \in [0, \infty)$ by linear interpolation. Of course, such a (random but non-fractal) curve $\gamma_a(t)$ has a Loewner driving function $U_a(t)$. The strategy is to try and prove that $U_a(t)$ converges to Brownian motion with variance κ as $a \to 0$ and t is rescaled appropriately. Indeed, this is the way that loop-erased random walks, the harmonic explorer and the Peano curve around uniform spanning trees were proved to converge to SLE_2, SLE_4 and SLE_8 respectively.

Yet, there are models for which this strategy is not feasible. Two such models are the self-avoiding walk and the percolation explorer. We will discuss here two properties[1] that lead to conjectures for their values of κ.

Definition Suppose L is a $\mathbb{H}$-hull bounded away from the origin. Let K_t and K_t^* be the hull families of two chordal processes from 0 to ∞ in $\mathbb{H}$ and $\mathbb{H} \setminus L$ respectively. The process is said to satisfy the *locality property* if for all such hulls L the distribution of K_t and K_t^* is the same[2], up to the hitting time to the boundary of L.

In words, a process satisfying locality is affected by a change in the shape of the domain only from the moment it hits the changed region on. As long as one is interested in the behaviour of the process before the hitting time, there is no difference in growing the hulls in the larger or in the restricted domain. In some very loose sense, the process is blind, in that it "feels the boundary only when it hits it". It can be proved that the only SLE process satisfying this property is that with parameter $\kappa = 6$. There is a lattice

[1] The reader be warned that there are almost as many ways of defining these properties as there are papers on the subject. We choose what we feel to be the most geometrical approach.

[2] Remember that equivalence up to a monotonic reparametrization of time is understood.

process satisfying a lattice version of the locality property: it is the critical percolation explorer (see Chapter 1). Since one expects the lattice property to be conserved under the continuum limit, one is led to conjecture SLE_6 as the scaling limit for the percolation explorer.

Definition Suppose L is a $\mathbb{H}$-hull bounded away from the origin and let g_L be the uniformizing map of L. Consider a conformal process supported on simple curves γ going from 0 to ∞ and not touching the real axis. The process is said to satisfy the *restriction property* if for all such hulls L, the distribution of the image under g_L of γ is the same as the distribution of γ, conditioned not to hit L[1].

Since this definition requires the process to assign null measure to non-simple curves and to curves touching the real axis, we shall apply it only to SLE_κ with $\kappa \leq 4$. Loosely speaking, the restriction property states that if the domain is extended, then the new process will give the same relative weights to the curves that still live in the smaller domain. The one SLE process satisfying restriction is that with parameter $\kappa = 8/3$. Self-avoiding walks on the lattice happen to satisfy a lattice version of this property (see Chapter 1), so they are conjectured to have $SLE_{8/3}$ as their scaling limit.

As we said, many more models have been either proved or conjectured to yield SLE processes in the scaling limit. Some of these are summarized in Table 2.6.

2.7 Radial and whole-plane SLE

One can also consider curves in other geometries. For instance, radial processes growing from a boundary point towards the bulk are not accounted for by the discussion in the preceding sections. Eventually, we will be interested in defining a version of SLE in the whole plane. It turns out to be useful to first develop the theory for a bounded region of C. Of course, the natural choice is to take the unit disc $\mathbb{D}$ as the standard domain, and the origin as the interior point toward which the curve goes. The Riemann mapping theorem then says that there is exactly one conformal mapping g of any simply connected domain containing the origin to $\mathbb{D}$ and such that $g(0) = 0$ and $g'(0) > 0$. We will again call this unique map g the *uniformizing map* of the domain. The simply connected regions we are interested in are of course

[1] There is a technical subtlety here, since the conditioning could happen to be on a set of null measure. In the SLE case, this is not a concern, since the requirement of simplicity actually implies that the set be of finite measure.

Model	κ	d_f	Ref
Loop-erased random walk	2	5/4	[25, 33]
Ising spin glass	~ 2.1		[34]
Self-avoiding walk	8/3	4/3	[35]
Ising model (spin clusters)	3	11/8	[27]
Dimer tilings	4	3/2	[36]
Harmonic explorer	4	3/2	[37]
Level lines of Gaussian field	4	3/2	[38]
Inverse turbulent cascades	4	3/2	[39]
Ising model (FK clusters)	16/3	5/3	[27]
Percolation	6	7/4	[40, 41]
Uniform spanning trees	8	2	[33]

Table 2.1: Some models for which a connection to SLE has been established, either by proof, conjecture or numerical analysis. The table shows the values of κ and of the fractal dimension.

those corresponding to the hulls of radial processes starting from a boundary point $w \in \partial\mathbb{D}$ and going to 0:

Definition A subset A of $\mathbb{D} \setminus \{0\}$ is a $\mathbb{D}$-*hull* if $A = \mathbb{D} \cap \bar{A}$ and $\mathbb{D} \setminus A$ is simply connected.

Just as the half-plane capacity represents the "conformal size" of a $\mathbb{H}$-hull "as seen from infinity", there is a corresponding definition here of "conformal size" of a $\mathbb{D}$-hull "as seen from the origin":

Definition Let A be a $\mathbb{D}$-hull and g_A its uniformizing map. Then $g'_A(0)$ is a real positive number. The *logarithmic capacity* of A (in the unit disc) is

$$\mathrm{lcap}_0(A) = \log g'_A(0). \tag{2.38}$$

Notice a nice property of the logarithmic capacity that regards its behavior under composition of the maps: if A, B and C are $\mathbb{D}$-hulls such that $g_A = g_B \circ g_C$ then $\mathrm{lcap}_0(A) = \mathrm{lcap}_0(B) + \mathrm{lcap}_0(C)$.

There exists a version of the Loewner equation also in $\mathbb{D}$, which describes the evolution of a conformal Markov radial process in terms of a real function. The same reasoning as in the chordal case then leads to considering rescaled Brownian motion as a driving function, finally leading to the *radial SLE* equation

$$\dot{g}_t(z) = g_t(z)\frac{e^{i\xi_t} + g_t(z)}{e^{i\xi_t} - g_t(z)}, \quad g_0(z) = z, \tag{2.39}$$

where $\xi_t = \sqrt{\kappa}B_t$. As in the chordal case, the denominator in (2.39) can (and does) become zero. Of course, the *hulls* of the process are defined as in the chordal case: K_t is the set of those points in $\mathbb{D}$ for which the differential equation does not admit a solution that exists up to time t. By differentiating (2.39) and evaluating at $z = 0$, one finds

$$\partial_t g_t'(0) = g_t'(0) \tag{2.40}$$

which means that the logarithmic capacity grows linearly in time, as was the case for the half-plane capacity in chordal SLE:

$$\mathrm{lcap}(K_t) = t, \tag{2.41}$$

where K_t are the radial SLE hulls.

By applying a conformal transformation, one can turn (2.39) into an equation for a radial process in *any* simply connected domain. One very special such transformation is the complex inversion

$$\Pi(z) = \frac{1}{z} \tag{2.42}$$

which sends the unit circle $\mathbb{D}$ onto its exterior $\mathbb{C}\backslash\mathbb{D}$, which is simply connected only on the Riemann sphere. Let $\tilde{g}(z)$ be the map in the "punctured" plane $\mathbb{C} \setminus \mathbb{D}$ defined by

$$\tilde{g}(z) = \Pi \circ g \circ \Pi(z) = \frac{1}{g(\frac{1}{z})}. \tag{2.43}$$

Then, from Equation (2.39) one gets the whole-plane version of SLE

$$\partial_t \tilde{g}(z) = \tilde{g}_t(z)\frac{e^{-i\xi_t} + \tilde{g}_t(z)}{e^{-i\xi_t} - \tilde{g}_t(z)}, \quad \tilde{g}_0(z) = z. \tag{2.44}$$

This process is sometimes just referred to as the radial SLE *growing toward infinity*, when the name *whole-plane* SLE is reserved for another flavor of SLE, where one considers the radial process transformed with Π and extended to $t \in (-\infty, \infty)$. Yet, we will refer to (2.44) with $t \geq 0$ as whole-plane SLE, for we are not going to really shrink the circle to a point, since we will be interested only in the long distance behavior of the curve and will be treating the finite size of $\mathbb{D}$ as a cut-off.

Of course, the hull K_t in this case is defined as the set of points belonging to $\mathbb{C} \setminus \mathbb{D}$ such that the differential equation does not have a solution up to time t. Also, the notion of capacity can be extended. If K is a compact hull and $\tilde{g}_K$ is a conformal map of $\mathbb{C} \setminus \mathbb{D}$ onto $\mathbb{C} \setminus K$ with $\lim_{z\to\infty} \tilde{g}_K(z)/z > 0$ then the logarithmic capacity of K as seen from infinity is defined as

$$\mathrm{lcap}_\infty(K) = \log \lim_{z\to\infty} \frac{\tilde{g}_K(z)}{z} \tag{2.45}$$

With some abuse of language we shall call this whole-plane capacity logarithmic capacity *tout court*, as that defined for maps of the unit disc.

By differentiating (2.43), remembering $g(0) = 0$, one obtains a useful formula that relates the logarithmic capacities in the disc and in the plane:

$$g'(0) = \lim_{z\to\infty} \left(\frac{\tilde{g}(z)}{z} \right)^{-1} \tag{2.46}$$

If we call K and K' a $\mathbb{D}$-hull and its image under Π respectively, we then have

$$\mathrm{lcap}_0(K) = \mathrm{lcap}_\infty(K') \tag{2.47}$$

Sometimes (especially when simulating SLE, see Chapter 3) it will be more natural to consider the inverse of the Loewner map, g^{-1}. By substituting the identity $1 = g'(g^{-1}(z))\,(g^{-1})'(z)$ in Equation (2.46), one obtains

$$\mathrm{lcap}_\infty(K') = -\log\left(g^{-1}\right)'(0) \tag{2.48}$$

which gives the logarithmic capacity of a hull in $\mathbb{C}\backslash\mathbb{D}$ in terms of the derivative of the inverse Loewner map of its pre-image in $\mathbb{D}$.

Chapter 3

Simulating SLE

This chapter introduces a few techniques for simulating Schramm-Loewner evolutions both in $\mathbb{H}$ and in $\mathbb{C}$. Simulating SLE is an exercise of carefulness and compromise. Many steps are involved, and many possible strategies can be chosen. This chapter is not intended to be a comprehensive survey of the possibilities and hindrances one can face, but only a presentation of how the numerical results in later chapters have been obtained.

3.1 Discretizing time

We are going to approximate SLE by what is called a *discrete* SLE. This is not to be intended in the most strict sense. Actually, only the proper time variable t in Loewner equation will be discretized, while we will retain full continuity in the complex space variable[1]: the plane does not get replaced by a lattice. This is possible because one works with the iteration of conformal maps which will be chosen among a parametrized family: in this way, very complicated conformal maps can then be described by a string of real parameters.

Recall what we observed in Chapter 2 about the evolutor

$$\hat{g}_t = g_{s+t} \circ g_s^{-1}. \tag{3.1}$$

It satisfies the Loewner equation with driving function shifted by s. Indeed, this fact is not dependent on the explicit form of the equation. Let us consider a general Loewner-type equation of the form

$$\frac{d}{dt} g_t(z) = \Theta\left[g_t(z), U_t\right], \quad g_0(z) = z \tag{3.2}$$

[1]Of course, this is to be intended in the computer-science meaning, that is, continuity up to the machine's floating point precision.

where Θ depends explicitly only on the Loewner map and the driving function at time t. Then by deriving (3.1) one finds

$$\begin{aligned} \frac{d}{dt}\hat{g}_t(z) &= \left(\frac{d}{dt}g_{s+t}\right)\circ g_s^{-1} \\ &= \Theta\left[g_{s+t}\circ g_s^{-1}(z), U_t\right]. \end{aligned} \tag{3.3}$$

which states the Loewner semigroup property for this more general class of Loewner equations. Then, it holds also in the radial cases, that is for the SLE in the disc and in the punctured plane. This is a direct consequence of the Markov property. One can continue growing an already grown hull at finite time s by simply using the driving function from that time on. It is this property of the Loewner increments that permits an easy discretization of time.

Let us consider chordal SLE in $\mathbb{H}$ for definiteness. Let us partition $[0,\infty)$ into discrete intervals $0 = t_0 < t_1 < t_2 < \cdots < t_k < \cdots$ (in actual simulations we are going to consider only the first n such intervals). We define the increment at time t_k as [43]

$$G_k = g_{t_k}\circ g_{t_{k-1}}^{-1}. \tag{3.4}$$

Then

$$g_{t_k} = G_k\circ G_{k-1}\circ\cdots\circ G_1. \tag{3.5}$$

By the calculation above, $G_k(z)$ is obtained by solving the Loewner equation with driving function $U_{t_{k-1}+t}$ for $t\in(0, t_k - t_{k-1})$. Equation (3.5) represents the discretization of the process that we will use. It bears information about the whole conformal map. Most of the time we will only be interested in points on the trace $\gamma(t)$. With the foregoing approximation, we have access only to finite points on the trace, namely to

$$\begin{aligned} \gamma(t_k) &= g_{t_k}^{-1}\left(U_{t_k}\right) \\ &= G_1^{-1}\circ\cdots\circ G_k^{-1}\left(U_{t_k}\right). \end{aligned} \tag{3.6}$$

The increments G_k^{-1} map the half-plane onto the half-plane minus a hull comprising the real point $U_{t_{k-1}}$.

$$G_k^{-1} : \mathbb{H} \longrightarrow H\setminus g_{t_{k-1}}\left(\gamma[t_{k-1}, t_k]\right). \tag{3.7}$$

We will instead consider the following maps

$$h_k(z) = G_k^{-1}(z + U_{t_k}) - U_{t_{k-1}}. \tag{3.8}$$

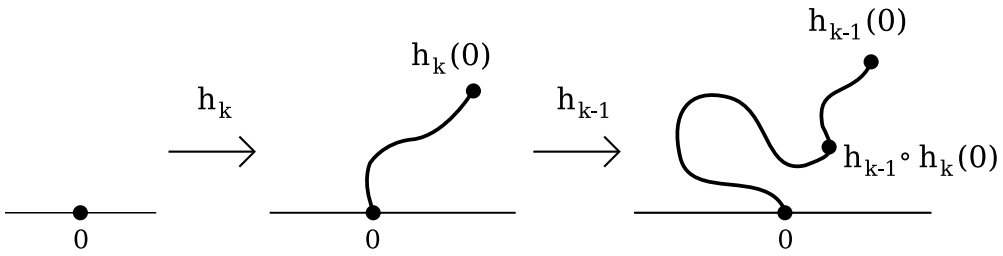

Figure 3.1: The composition of the incremental maps h_k building the curve by curvilinear segments.

which map the half-plane onto the half-plane minus a hull containing the origin. Equation (3.6) then becomes

$$\gamma(t_k) = h_1 \circ \cdots \circ h_k(0) \tag{3.9}$$

Equation (3.9) is the basis of the discretization procedure, as well as of the simulation strategy we will deploy. The incremental maps h_k act by growing a small piece of hull from the origin (refer to Figure 3.1). They are then concatenated in order to grow the whole hull. The first map h_k produces a small cut starting from the origin, by mapping a small interval of the real axis containing the origin up into the half plane. This cut will be of whatever shape is needed, but we will choose very simple and standard incremental maps for our simulations (see subsequent sections and Appendix A). The origin is sent to the tip of the cut. The second map h_{k-1} then does the same thing but with a possibly differently-shaped cut, thus growing one more curvilinear segment, and so on. Notice that the order of composition in (3.9) is the opposite than what one could naively expect, as the rightmost map is actually the last one in the ordered string. This very fact has a high impact on the time-per-point the computation takes, since we will have to go through the whole list of maps every time we need to compute a single point on the chain.

The incremental maps h_k will be chosen from a parametrized family of maps. One samples the driving function U_t at discrete times t_k, and defines it on the intervals $t_{k-1} < t < t_k$ in such a way that the Loewner equation has an explicit solution that can be computed during that interval. This solution is G_k, from which by translation one can find h_k by (3.8).

Let

$$\begin{aligned} \Delta_k &= t_k - t_{k-1} \\ \delta_k &= U_{t_k} - U_{t_{k-1}}. \end{aligned} \tag{3.10}$$

In the most simple case, the interpolating driving function will depend only on Δ_k and δ_k. One will then have to deal with families parametrized by two

such parameters, playing the roles of the quantized steps in time and space respectively. Actually, it is always easier to parametrize the curve by its capacity, so that the numerator in the right hand side of the SLE equation (2.5) will be a constant. The time parameter is thus closely related to the capacity of the incremental map. These parameters will have to be randomly chosen in such a way as to reproduce a discretization of the Brownian motion with the correct variance κ. We will say more about this in the forthcoming section.

One can also adopt a slightly different strategy. One can consider maps that do *not* map the origin to the tip of the curve, but instead do so for some small real number $\pm\delta$. Of course, the concatenation of these increments is not going to give a curve, since the hull will present branching points for every single step. Yet, a careful choice can lead nonetheless to a process that does converge to SLE (see next section).

3.2 Half plane

Let us consider now the discretization procedure for SLE in the half plane $\mathbb{H}$. A possible choice for the incremental map would be

$$h_k(z) = (z + y_k)^{1-\alpha}(z - x_k)^{\alpha} \tag{3.11}$$

with real numbers x_k and y_k chosen in such a way as to satisfy hydrodynamic normalization and capacity $2\Delta_k$. This map produces a tilted slit of angle α with respect to the positive real axis. This choice amounts to approximating SLE by tilted segments. Notice that this does not imply that the produced hull actually be a union of segments. In fact, segments already grown get distorted more and more as the rest of the curve is built.

Instead, we will choose to follow a simpler strategy, and use incremental maps that do not send the origin to the tip of the curve (see the discussion in the preceding section). We will thus define

$$h_k = T_{\delta_k} \circ \phi_k^{\mathbb{H}} \tag{3.12}$$

where

$$\phi_k^{\mathbb{H}}(z) = \sqrt{z^2 - 4\Delta_k} \tag{3.13}$$

is the atomic map, which depends on a single (time-like) parameter related to the capacity. T_{δ_k} is a translation by the real (space-like) parameter δ_k. There is an important subtlety here, which concerns the branch-cut of the square root. Let us fix the principal value so that $\sqrt{1} = +1$. The common use is to put the branch-cut on the negative real axis. We will instead choose

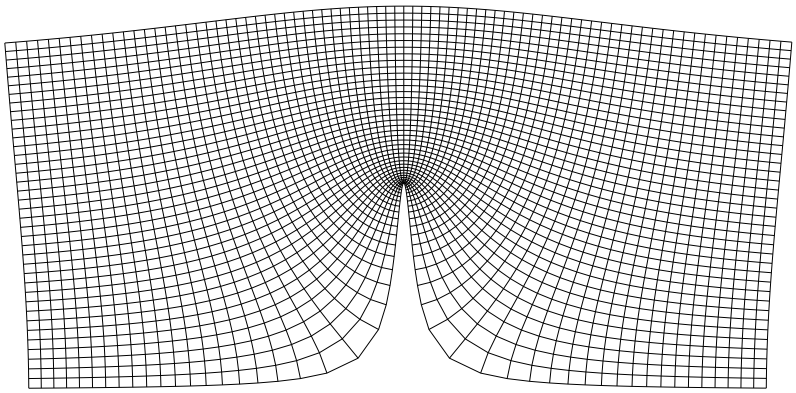

Figure 3.2: The image — under the atomic map in (3.13) — of a lattice with links parallel to the coordinate axes. The bottom line is *not* the image of the real axis. Rather, it corresponds to a line parallel to the real axis and slightly offset in the imaginary direction. The image of $\mathbb{R}$ is not a regular curve. Notice the singularity at $z = 2i$.

to have it on the *positive* real axis, so that (3.13) actually has the upper half plane as co-domain. The map in (3.13) is graphically depicted in Figure 3.2. It maps the half plane onto the half plane minus a vertical slit based at the origin and has capacity $2\Delta_k$, that is to say, the segment is of length $2\sqrt{\Delta_k}$. It is the inverse map of the solution to the Loewner equation in the special case where the driving function is constant in time (in particular it is 0; otherwise the map would simply get shifted). In this case, the evolution is very simple, and the hull is a straight segment of the imaginary axis, growing with capacity $2t$ (that is, its length grows with the square root of time). With this choice for the incremental map, Equation (3.9) then becomes

$$\gamma(t_k) = T_{\delta_1} \circ \phi_1^{\mathbb{H}} \circ T_{\delta_2} \circ \phi_2^{\mathbb{H}} \circ \cdots \circ T_{\delta_k} \circ \phi_k^{\mathbb{H}}(0). \tag{3.14}$$

In words, the first (rightmost) map grows a slit based at the origin: this slit will become the last curvilinear segment of the hull. Then the half plane is translated and another slit is created at the origin. The process continues until the last slit — which constitutes the first segment of the hull — is created and no translation is performed, so that the hull will be based at the origin. Where does the tip of the hull get mapped to by the Loewner map? Refer to Figure 3.3. Imagine we have grown the hull up to discrete time t_k using the map $h_1 \circ \cdots \circ h_k$. The Loewner map at this time will be g_k, which absorbs the hull and sends the tip z_k to the real point U_k. Now let us add one step. This means adding one map h_{k+1} at the beginning, that is at the

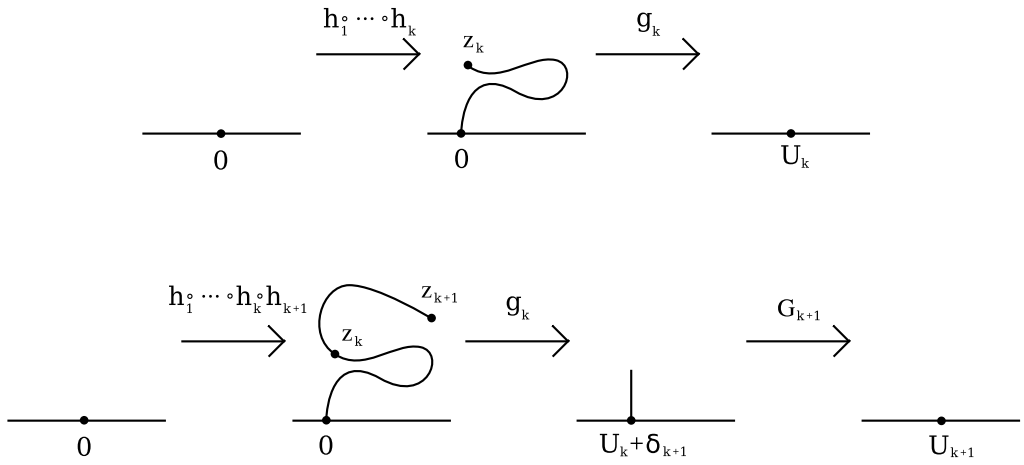

Figure 3.3: The hull at step k is created by the map $h_1 \circ \cdots \circ h_k$ and absorbed back into the half plane by g_k. The latter does not absorb the hull at step $k+1$, but leaves a slit based at $U - k + \delta_{k+1}$.

rightmost place in the composition chain. The new hull is built with map $h_1 \circ \cdots \circ h_k \circ h_{k+1}$ and absorbed by the Loewner map $g_{k+1} = G_{k+1} \circ g_k$, from Equation (3.4). The first step is performed by g_k, which maps z_k to U_k and the last segment of the hull (ending at z_{k+1}) to a slit based at $U_k + \delta_{k+1}$. Then, the map G_{k+1}, which by Equations (3.8) and (3.12) can be written as

$$\begin{aligned} G_{k+1} &= T_{U_{k+1}} \circ h_{k+1}^{-1} \circ T_{-U_k} \\ &= T_{U_{k+1}} \circ \left(\phi_{k+1}^{\mathbb{H}}\right)^{-1} \circ T_{-\delta_{k+1}} \circ T_{-U_k} \\ &= T_{U_{k+1}} \circ \left(\phi_{k+1}^{\mathbb{H}}\right)^{-1} \circ T_{-\delta_{k+1}-U_k}, \end{aligned} \tag{3.15}$$

sends what remains to the half plane, mapping the tip of the slit to the real number U_{k+1}. One then sees that

$$U_{k+1} = U_k + \delta_{k+1}. \tag{3.16}$$

This equation tells us that — as was to be expected — the process δ_k is an approximation of the *discrete time derivative* of the process U_k. In the scaling limit, where we want U_t to be a Brownian motion with variance κ, we then expect δ_t to be κ-correlated white noise. We have several possible choices for the discrete process δ_k. We choose to draw δ_k (independently of k) with uniform measure in the set $\{\sqrt{\kappa\Delta_k}, -\sqrt{\kappa\Delta_k}\}$, which amounts to approximating the Brownian motion by a simple random walk with step length $\sqrt{\kappa\Delta_k}$. A formal theorem about convergence of this "discrete SLE" process to continuum SLE has been proved by Bauer [44].

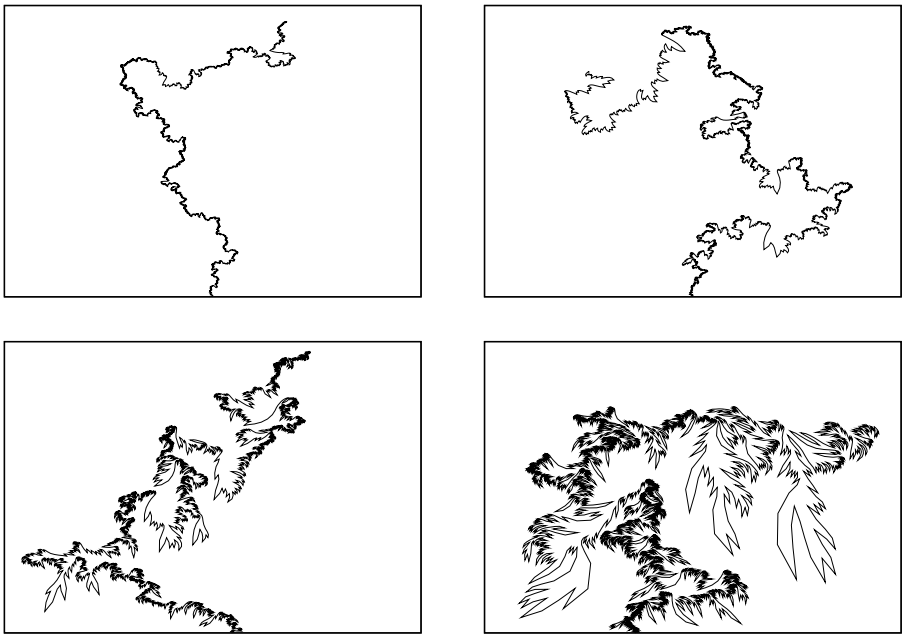

Figure 3.4: Four examples of approximate SLE traces in the half plane. Top-left: $\kappa = 2$; top-right: $\kappa = 8/3$; bottom-left: $\kappa = 6$; bottom-right: $\kappa = 8$.

Some examples of the approximate SLE trace for various values of the diffusivity κ are presented in Figure 3.4.

3.3 Whole plane

Simulating SLE in the whole plane is just a matter of finding the right atomic map ϕ_k. The rest is the application of the same reasoning as in the preceding section. We choose the atomic map following the same strategy as in the half plane. We look for the solution of the whole-plane Loewner equation in the simple case when the driving function is constant. Here, of course, we can not fix the constant to zero, since it lives on the unit circle. Instead, we will take it to be 1, so as to have a curve starting from a point on the real axis:

$$e^{i\theta_t} = 1. \tag{3.17}$$

Of course, this choice explicitly breaks rotational invariance, since the real point 1 selects a specific direction in the complex plane. Nonetheless, we will be interested here in *radial* quantities, that is, we will be averaging out the angular dependence of observables, so that symmetry will be reestablished

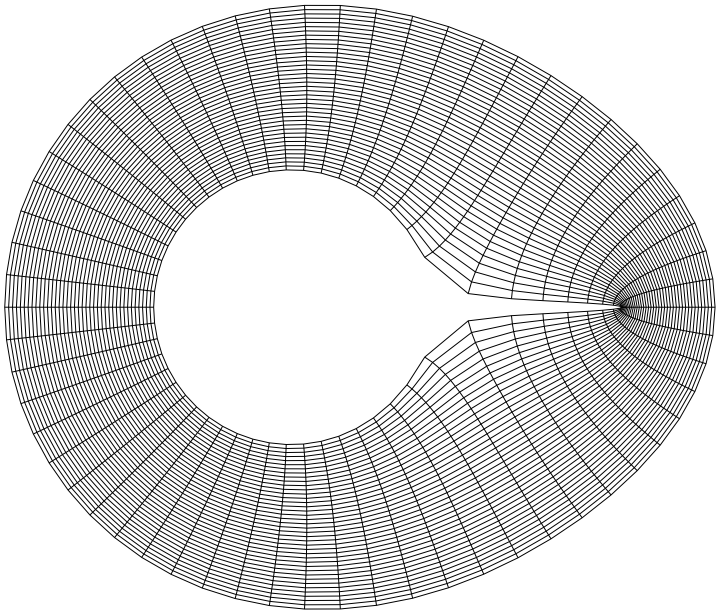

Figure 3.5: The image — under the atomic map in (3.18) — of a lattice made of radii and circumferences around the unit circle. The innermost curve is *not* the image of $\partial\mathbb{D}$. Rather, it is a circumference with radius slightly greater than 1. Notice the singularity, which lies on the real axis.

(see Chapter 6). See Appendix A for the details of the calculation and some heuristics about the solution to the whole-plane Loewner equation with constant driving function. The atomic map, obtained by interpreting Loewner time in the solution as the parameter Δ_k and then taking the inverse, is finally

$$\phi_k^{\mathbb{C}\setminus\mathbb{D}} = \Pi \circ \phi_k^{\mathbb{D}} \circ \Pi, \tag{3.18}$$

where $\Pi(z) = 1/z$ is the complex inversion and $\phi_k^{\mathbb{D}}$ is the inverse slit solution to the Loewner equation with constant driving function in the unit disc $\mathbb{D}$

$$\phi_k^{\mathbb{D}}(z) = \frac{1}{4e^{-\Delta_k} z}\left[2(z+1)^2 - 4e^{-\Delta_k} z - 2(z+1)\sqrt{(z+1)^2 - 4e^{-\Delta_k} z}\right]. \tag{3.19}$$

A visualization of the map[1] in (3.18) is in Figure 3.5. A very close relative to this map already appeared in the literature about diffusion limited aggregates (see Section 4.2 and references therein).

[1]Here, as well as in the chordal case, the choice of the analytical branch for the square root is crucial, especially for the purpose of simulating (the visualization in Figure 3.5 of course makes use of this). See Appendix A for details.

It is easy to check that the atomic map builds a hull of logarithmic capacity Δ_k. In fact, by expanding (3.18) around $z = 0$ one has

$$\phi_k^{\mathbb{D}} = \frac{1}{4e^{-\Delta_k} z} \left[4e^{-2\Delta_k} z^2 + o(z^2)\right] = z e^{-\Delta_k} + o(z) \tag{3.20}$$

which by equation (2.48) and the additivity property of the logarithmic capacity, means that the growing approximated hull at step k has logarithmic capacity $\sum \Delta_k$, and Δ_k again plays the role of time in the Loewner equation as in the chordal case, since by Equation (2.41) whole-plane SLE grows with logarithmic capacity t.

In the half plane, back in the preceding chapter, we built the incremental maps by chaining the slit map with translations by a real number. Here in the whole (punctured) plane, what plays the role of translations is the rotations around the origin. Indeed, Brownian motion in chordal SLE lives on the real axis, so that it can be regarded as a random walk in the group of real translations. On the other hand, Brownian motion in radial and whole plane SLE lives on the unit circle, and can be thus regarded as a random walk in the group of rotations. The incremental maps we are going to employ are then[1]

$$\begin{aligned} c_k &= R_{\delta_k} \circ \phi_k^{\mathbb{C}\setminus\mathbb{D}} \\ &= R_{\delta_k} \circ \Pi \circ \phi_k^{\mathbb{D}} \circ \Pi, \end{aligned} \tag{3.21}$$

where

$$R_{\delta_k}(z) = e^{i\delta_k} z \tag{3.22}$$

so that Equation (3.9) is replaced by

$$\gamma(t_k) = c_1 \circ \cdots \circ c_k(0). \tag{3.23}$$

As well as in the half-plane case, we draw the δ_k's as Bernoulli variables in the set $\{\sqrt{\kappa\Delta_k}, -\sqrt{\kappa\Delta_k}\}$. We mention here that one has actually one more degree of freedom. In fact, there remains to choose the time-steps Δ_k, that is the partitioning of time. The most natural choice would be to take them equally spaced. What one sees is that if one does so, then the points on the SLE trace come out to be farther and farther apart as one travels along the curve. This is true for the whole-plane version, while the opposite happens for chordal SLE in the half plane: the points appear more and more distant from each other as one approaches the origin. To prevent this from happening, we let Δ_k scale with a certain law depending on k. The tedious

[1] Remember that $\phi_k^{\mathbb{D}}$ implicitly depends on Δ_k so that the incremental maps actually depend on both time- and space-like parameters Δ_k and δ_k.

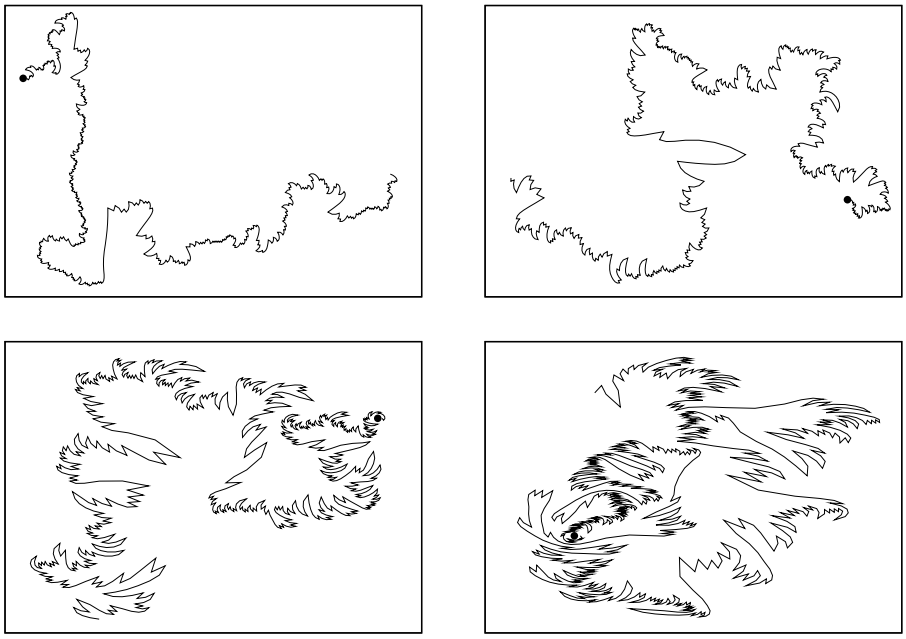

Figure 3.6: Four examples of approximate SLE traces in the whole plane. The black dots corrspond to the unit disc, which is avoided by the curve. Top-left: $\kappa = 2$; top-right: $\kappa = 8/3$; bottom-left: $\kappa = 6$; bottom-right: $\kappa = 8$.

computations that show how this law must be chosen are presented in detail in Appendix B. Basically, half-plane SLE requires

$$\Delta_k \sim k^{1/2}, \tag{3.24}$$

while for whole-plane SLE approximate time-invariant distribution of the steps is achieved through the choice

$$\Delta_k \sim k^{-1}. \tag{3.25}$$

Examples of the approximation to the whole-plane SLE trace obtained by the method presented in this section are shown in Figure 3.6.

Finally, figures 3.7 and 3.8 show (the image of the coordinate lattice under) the conformal maps corresponding to a few steps of the algorithms described in this chapter for half-plane and whole-plane SLE. Notice that the Jacobian of the map becomes large close to the trace, as is displayed by the increasing size of the cells. The apparent finite width of the trace is for illustration purposes: of course every point has a counter-image, no matter how close to the trace it is.

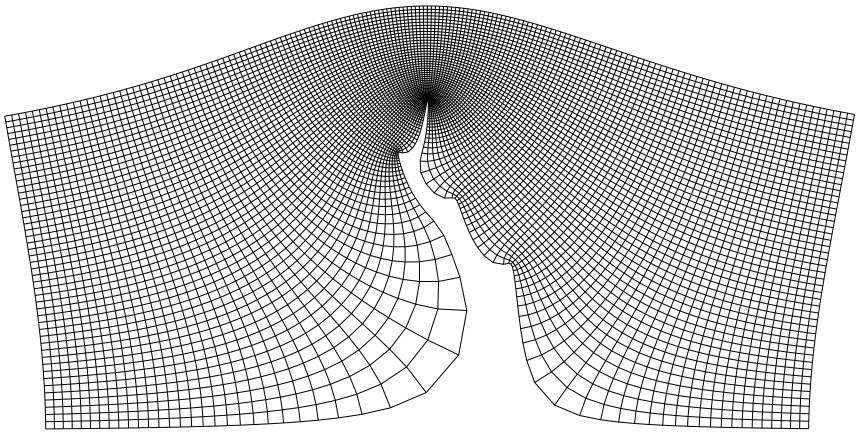

Figure 3.7: An example of an iterated conformal map that grows a half-plane hull.

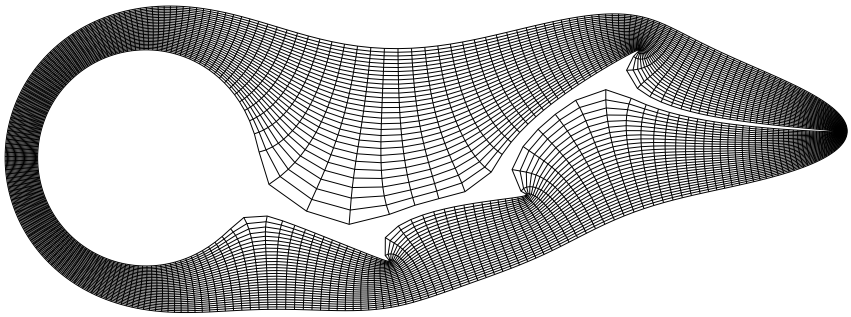

Figure 3.8: An example of an iterated conformal map that grows a whole-plane hull.

Chapter 4

Reparametrizing SLE

This chapter gathers material about the specific issue of SLE trace reparametrization. Those presented here are just hints and ideas, since work is still in progress. Much of what follows is preliminary, and is only intended as a statement of the problem and and indication of some possible directions where to look for a solution.

4.1 Reparametrization issues

Most of the observables mathematicians are interested in are parametrization-independent. For instance, the fractal dimension of a curve or the probability that it passes to the left of a given point are only dependent on the shape of the curve, that is, on its support. On the other hand, polymer scientists and statistical mechanicists more often focus their attention on quantities that do depend on the particular choice of the parametrization. One very important example (especially for our purposes) is the *distribution of the end-point* of a walk. Actually, every observable concerning the position of the end-point will depend on how one measures the "length" of the walk, since a definition of length is indeed necessary for the very definition of end-point. Of course, a real polymer has a very natural way of measuring length along the chain: one counts the number of polymers, starting from one end and travelling towards the other. This monomer-counting procedure is essentially what one also uses for the self-avoiding walk. In trying to define the scaling limit of SAWs the most natural thing to do is to define a continuum parametrization of the lattice walk, so as to embed it in the complex plane:

$$\omega_i \in \Lambda \rightsquigarrow \tilde{\omega}(t) \in \mathbb{C}, \tag{4.1}$$

one then passes from a discrete index $i \in \mathbb{N}$ to a continuum time $t \in \mathbb{R}^+$. The obvious choice is to let

$$\omega_i = \tilde{\omega}(t) \quad \text{for} t = i \tag{4.2}$$

and linearly interpolating for non-integer times. This choice leads to what we will call the *natural* parametrization in the scaling limit (if it exists). Basically, since it amounts to counting the number of equal-length steps on the walk, it is a parametrization by *length*.

Of course, when one compares parametrization-dependent quantities in the lattice models with those in SLE, one wants to be using the same parametrization in the continuum models. It is not at all obvious that SLE as it is generated by the algorithm described in Chapter 3 should have a parametrization in any way similar to that of the SAW. In fact, we already chose a particular parametrization for SLE in Chapter 2, such as to have the usual Brownian motion appear as the driving function. This parametrization is that *by capacity*, which means that capacity grows linearly with proper time along the curve. Since we sample Brownian motion by discretizing its natural parametrization, we are generating samples of SLE parametrized by capacity. Even if we rescale time as in (3.24) and (3.25) to try and have approximately steps of equal length, we are simply reparametrizing the curves in a global fashion. We are just changing time labelling of *every* sample in the same way. If we were to rescale time in such a way, and computed the scaling dimension of the end-to-end radius R_e, we would find the trivial result $\nu = 1$ nonetheless. This is due to the fact that we are compensating for the scaling of the step-length only *on average*, but the step-lengths still have a high variance, and retain a strong correlation with the geometry of the already-grown hull. Figure 4.1 presents a plot of an SLE trace (in the whole plane) with the non-random scaling (3.25), for the sake of comparison with the techniques we will present in the forthcoming.

If one looks closely at how length and capacity are (un-)related, one clearly sees that the reparametrization procedure has to be done on a sample-by-sample basis. In fact, capacity and length are not in one-to-one correspondence, even for discrete curves. It is easy to produce two (non-fractal) curves with the same length but different capacities, and vice-versa. This means that the reparametrization must be *random*. This fact was first highlighted in [45], with the aid of numerical computations. In the rest of this chapter we will be dealing with ways of simulating SLE with the correct parametrization (that is, with that of the supposed continuum limits of the lattice walks). In other words, we will be interested in a *numerical* strategy. Rigorous analysis of the problem and some proposals for analytically tractable definitions are

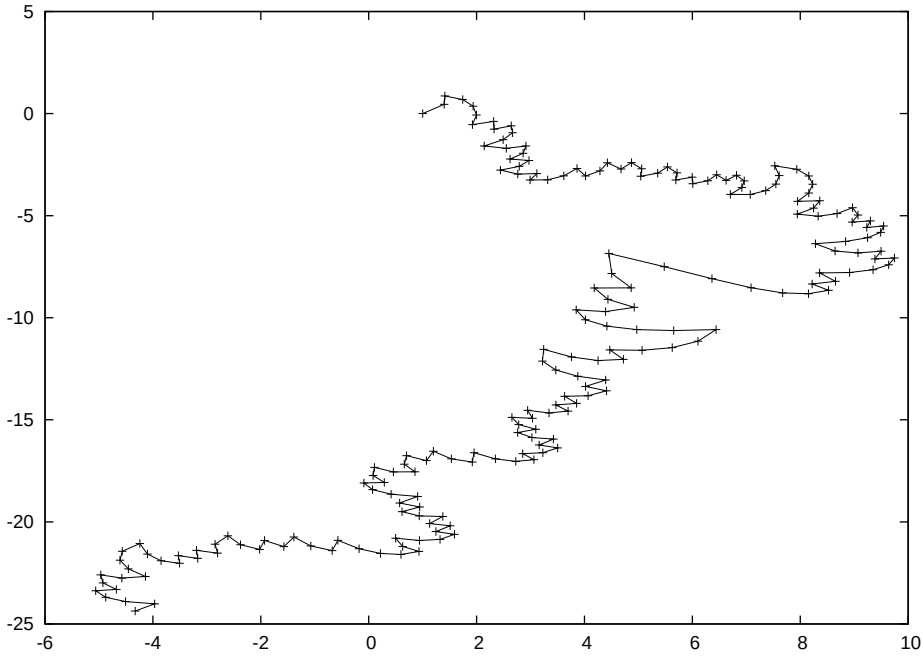

Figure 4.1: The approximate reparametrized SLE trace, obtained by simply rescaling the time-steps as in (3.25) (here $\kappa = 8/3$). The crosses indicate consecutive points on the trace.

presented in a recent work by Lawler [46], but almost no analytical results are yet available.

4.2 Intermezzo: diffusion-limited aggregation

We take a short break and briefly describe a model of fractal growth called DLA. What it shares with SLE is the computational strategy based on conformal maps, and it will then serve as a comparison for the reparametrizing techniques we will discuss in this chapter.

Diffusion limited aggregation (DLA) was introduced by Witten and Sander [47]. It is a kinetic model where finite-sized particles perform random walks (one at a time) from infinity until they stick irreversibly to a cluster, which grows from a seed at the origin. DLA and its variants provide simple models for many fractal patterns in nature, such as colloidal aggregates, dendritic electro-deposits, snowflakes, lightning strikes (dielectric breakdown), mineral deposits. It is a very interesting mathematical object *per se*, and many of its properties are not yet well-understood.

Let us suppose there is a cluster around the origin of the complex plane (DLA itself can be studied in any dimension, but we are interested in the 2-dimensional model here). We want to compute the probability $P_{\mathcal{C}}(\Delta)$ that a random walker B_t (Brownian motion) started from infinity hits the cluster $\mathcal{C}$ for the first time inside a subset $\Delta \subset \partial\mathcal{C}$ of its boundary $\partial\mathcal{C}$. Since the Brownian motion is conformally invariant, the problem can be reduced to a much simpler situation by use of a conformal map. If we define the *uniformizing* map as the conformal map[1] that maps the cluster to the unit disc

$$\phi_{\mathcal{C}} : \mathcal{C} \mapsto \mathbb{D} \tag{4.3}$$

then

$$P_{\mathcal{C}}(\Delta) = P_{\phi_{\mathcal{C}}(\mathcal{C})\equiv\mathbb{D}}\left(\phi_{\mathcal{C}}(\Delta)\right) \tag{4.4}$$

where $\phi_{\mathcal{C}}(\Delta)$ is a subset of the boundary of the unit disc $\mathbb{D}$. Of course, in the new ϕ-transformed geometry, the problem is radially symmetric, and very easy to solve, since the probability density $p(\theta)$ giving rise to $P_{\mathbb{D}}$ is a constant function of the angle θ. This view on DLA highlights its similarity with a continuum non-stochastic growth model called Laplacian growth, which is ubiquitous in the study of interfacial dynamics (see for instance the nice review by Crowdy [48]).

Hastings and Levitov [49] took advantage of this conformal symmetry, and proposed an algorithm which turns out to be quite similar to what we use for simulating Schramm-Loewner evolutions. The algorithm works as follows. The seed of the growth is the unit disc. At each time-step, an angle θ is chosen with the uniform distribution in $[0, 2\pi)$. A conformal map $g_{\lambda,\theta}$ is applied, that creates a bump of fixed area λ centered at $e^{i\theta}$. Then, another θ is chosen, the maps are composed, and so forth.

This growth process satisfies an even stronger version of the domain Markov property we discussed in Chapter 2, since now the growth of the fractal at a specific time does not even depend on where it last grew, so the future does not depend on the past, but — modulo a conformal transformation — it does not depend on the present either.

An important technical aspect of this algorithm is that one wants to grow bumps of approximately equal size as time grows. But peripheral bumps have undergone several conformal maps and have thus changed their shape and size. To compensate this rescaling, one wants to create bumps of different sizes, depending on the whole history of maps the will be subject to in the remainder of the growth process. As a first approximation, as long as the

[1] This map is unique if one fixes the image of the origin and the direction of the derivative in the origin. See Chapter 2.

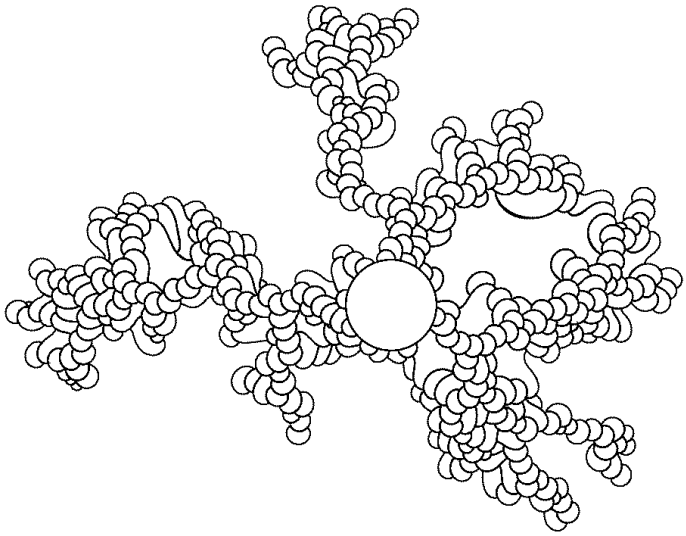

Figure 4.2: A DLA cluster generated with the method of Hastings and Levitov, through composition of conformal maps.

new bump is sufficiently small, it is natural to try and correct only for the Jacobian factor J_{n-1} of the previous conformal map, calculated at the center of the new bump, so that the n-th bump size would be

$$\lambda_n = \frac{\lambda_0}{J_{n-1}(e^{i\theta_n})}. \tag{4.5}$$

This strategy seems to give satisfying results (there is another subtlety, see [50]). An example of a small cluster generated with these techniques is in Figure 4.2;

4.3 Numerical strategies

4.3.1 First derivative of ϕ

It is very natural to try and apply the DLA strategy to the numerical reparametrization of SLE: rescaling the size of the k-th step of the approximated SLE trace by the dilatation factor given by the Jacobian. Let us restrict to the whole-plane case (the half-plane situation is just easier). The size L_k of the k-th step is a function of the time-like parameter Δ_k that controls the

capacity of the atomic map at step k

$$\Delta_k = \log \frac{\left(\frac{L_k}{1+L_k} - 2\right)^2}{4\left(1 - \frac{L_k}{1+L_k}\right)}, \tag{4.6}$$

as can be seen by calculating the length of the segment created *inside* the circle by $\phi_k^{\mathbb{D}}$

$$\tilde{L} = 1 - \phi_k^{\mathbb{D}}(1) \tag{4.7}$$

and then observing that complex inversion sends

$$\tilde{L} \mapsto L, \quad \tilde{L} = \frac{L}{1+L} \tag{4.8}$$

Finally one wants to rescale Δ_k so that L_k gets rescaled by a factor given by the Jacobian

$$J_k = |\partial_z g_k(z)|_w \tag{4.9}$$

calculated in terms of the derivative of the complex map g_k that grows the whole hull at step k, evaluated at the point w on the unit circle where the next slit is to be placed.

Unfortunately, there happens to be a great obstruction to this program, due to the fact that SLE satisfies "only" domain Markov property, instead of the stronger independence of the DLA steps that we discussed in Section 4.2. If we look at Equation (4.5) we see that the rescaling of the step-sizes is possible because of the independence of θ_n (the *space-like* variable) from λ_n (the *time-like* variable). This independence in DLA stems from the fact that the distribution of the θ's is flat on $[0, 2\pi)$ and does not change, so that one can operatively choose every step $\theta_0, \ldots, \theta_n$ *before* performing the composition of the corresponding maps. In SLE, on the contrary, despite the fact that the steps satisfy domain Markov independency, the *increments* δ_k are drawn with a Bernoulli distribution from the set $\left\{\sqrt{\kappa\Delta_k}, -\sqrt{\kappa\Delta_k}\right\}$, which does depend on time, since it depends explicitly on the time-like parameter Δ_k. Therefore, the problem is that we do not really know where to compute the Jacobian, until we have actually computed it! This is ultimately related to the fact that SLE is driven by a non-trivial stochastic process, so that Δ_k and δ_k are intertwined.

A possible way out of this impasse is to try and guess the position (call it δ_k^0) of the next spike — based on some scaling or heuristics —, calculate the Jacobian there, and then rescale both Δ_k and δ_k accordingly. Of course the new δ_k will generally be different from the tentative one. It is therefore possible to measure the error one is making, and iteratively repeat the

procedure in a self-consistent fashion, until the error drops under a reasonable bound. There is nonetheless no assurance that this procedure will ever converge. In fact, some preliminary numerical results show that the error actually increases after the first iteration, and gets completely out of control. We will thus stick to a single iteration in the upcoming.

Since δ_k is a Bernoulli variable in $\left\{\sqrt{\kappa\Delta_k}, -\sqrt{\kappa\Delta_k}\right\}$, only its amplitude depends on Δ_k, but not its sign. One can then draw a random sign $s_k \in \{+1, -1\}$, which is independent of the properties of the conformal map, and then calculate Δ_k and δ_k based on it. This amounts to choosing the direction to turn (whether left or right) first, and then using the Jacobian to calculate how far to go. The first value of δ one tries will then be

$$\delta_k^0 = s_k \lambda_k \tag{4.10}$$

One has some freedom in the choice of the tentative step-length λ_k. Taking a constant $\lambda_k = \lambda$ is not a good choice because as we saw in Chapter 3 the values of Δ_k increase (decrease) more and more as the chain grows, in whole-plane (half-plane) SLE. One can follow several strategies:

- Rescale λ_k according to the known scaling law, (3.24) or (3.25);
- Set it to the previously calculated "true" δ:

$$\lambda_k = \frac{\delta_{k-1}}{s_{k-1}}; \tag{4.11}$$

- Guess it with some heuristics based on the knowledge of the whole history $\{\delta_k\}_k$.

The third strategy needs a deep understanding of how the conformation of the chain and the Jacobian of the conformal map are linked. We implemented the first and the second ones instead (which seem to give similar results).

Notice that it is impossible to get information from the first derivative in 0 (for half-plane SLE) or in 1 (for whole-plane SLE), since the Loewner maps are singular there, and the atomic map has null derivative.

An example of the approximate SLE trace obtained by this method is in Figure 4.3.

4.3.2 Second derivative of ϕ

So, the main problem with the first-derivative approach is that δ_k and Δ_k depend on one another, so that one does not really know where to compute the derivative. One way to overcome this problem is the following. Expand

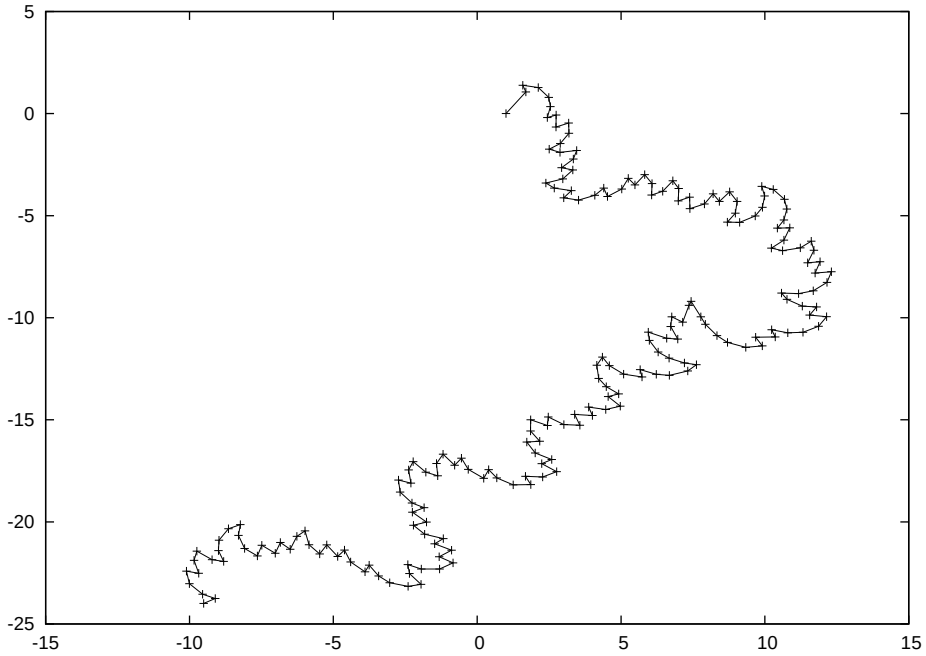

Figure 4.3: The approximate reparametrized SLE trace, obtained by the first-derivative method of Section 4.3.1 (here $\kappa = 8/3$). The crosses indicate consecutive points on the trace. The sample has been generated with the same sequence of signs used for that in Figure 4.1.

the derivative of g_k, the map that grows the whole hull at step k, around its zero, which occurs at $z = 1$, and evaluate it at the point $e^{i\Delta_k}$, which is the place where the $(k+1)$-th slit is going to be placed:

$$\partial g_k(e^{i\delta_k}) = \partial g_k(1) + \left(e^{i\delta_k} - 1\right) \partial^2 g_k(1) + \dots \tag{4.12}$$

where a shorthand $\partial g_k(w) \equiv \partial_z g_k(z)\big|_w$ is used for the first and second derivatives. By expanding the exponential, taking the modulus, and remembering that $\partial_z g_k(1) = 0$ one obtains the Jacobian at order $|\delta_k|$

$$J_k \approx |\delta_k| \left|\partial_z^2(1)\right|. \tag{4.13}$$

We want to rescale the length of the slit L_k by J_k, so we rewrite the equation relating Δ_k and L_k (4.6) using

$$L_k = \frac{\lambda}{J_k}, \tag{4.14}$$

where λ is the desired step length, and the Brownian relation

$$|\delta_k| = \sqrt{\kappa \Delta_k}. \tag{4.15}$$

Finally, we obtain an equation which (if solved) gives the time-step Δ_k such that it produces both the correct rescaling and the right relation with the space-step δ_k:

$$e^{\Delta_k} = \frac{1}{4}\left(2 - \frac{\lambda}{\lambda + \partial^2 g_k(1)\sqrt{\kappa\Delta_k}}\right)^2 \left(1 - \frac{\lambda}{\lambda + \partial^2 g_k(1)\sqrt{\kappa\Delta_k}}\right)^{-1}. \quad (4.16)$$

The actual sign of $\delta_k = \pm\sqrt{\kappa\Delta_k}$ is to be chosen at random, according to the Bernoulli nature of δ_k.

Unfortunately, Equation (4.16) is transcendental, and can not be solved explicitly. A little thinking shows that for $\partial^2 g_k(1)$ large one expects a small Δ_k. A crude approximation is then obtained by expanding (4.16) in powers of $\partial^2 g_k(1)$ around ∞, keeping only the terms up to $O(\Delta_k^4)$, so that the resulting algebraic equation can be solved explicitly. Nothing ensures that the resulting Δ_k will be real (this means that the desired point where the derivative has the right properties does not necessarily lie on the unit circle), but nonetheless we get the approximate scaling in $\partial^2 g_k(1)$. The resulting behavior is finally

$$\Delta_k \sim \frac{\Lambda}{\partial^2 g_k(1)}, \quad (4.17)$$

where the constant Λ is a function of κ and λ. Since the equation for Λ is of grade 4, one actually gets 4 roots. They happen to be all real, meaning that under this approximation the point we are seeking is indeed on the unit circle. We choose the one solution that is different from 0 and positive

$$\Lambda = \frac{\lambda}{2\sqrt{\kappa}}. \quad (4.18)$$

An example of the approximate SLE trace obtained by this method is in Figure 4.4.

4.3.3 Fractal variation

A different approach was proposed and studied by Kennedy [45, 51]. Instead of trying to grow the trace with strictly constant step lengths, one could also use the natural parametrization by capacity, and stop the growth when a fixed "length" has been reached. For this purpose, one needs a sensible definition of what the "length" of a discretized fractal object is.

Let $\gamma(t)$ be a parametrized curve. If γ is the trace of a Brownian motion in the plane, then it is a well-known result of probability theory that if one partitions time with $0 = t_0 < t_1 < \cdots < t_n = t$ then the naive notion of

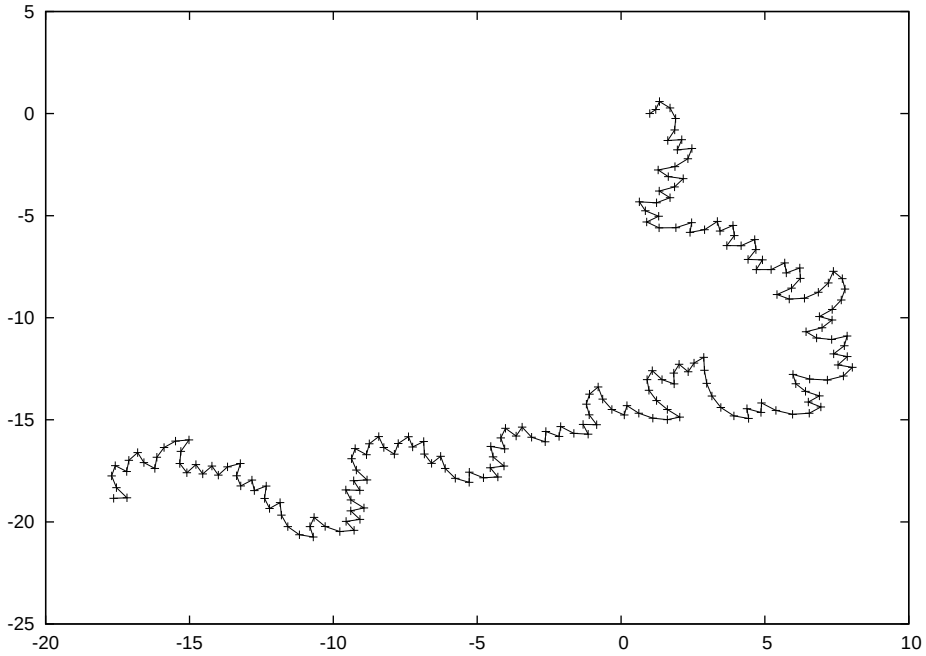

Figure 4.4: The approximate reparametrized SLE trace, obtained by the second-derivative method of Section 4.3.2 (here $\kappa = 8/3$). The crosses indicate consecutive points on the trace. The sample has been generated with the same sequence of signs used for that in Figure 4.1.

length defined by $L_n(\gamma[0,t]) = \sum_i |\gamma(t_i) - \gamma(t_{i-1})|$ diverges as $n \to \infty$, while the *quadratic variation*

$$\mathrm{var}_2(\gamma[0,t]) = \lim_{n\to\infty} \sum_{i=1}^{n} |\gamma(t_i) - \gamma(t_{i-1})|^2 \tag{4.19}$$

is finite. This is of course due to the fractal nature of the Brownian paths, for which "space" scales as the square root of "time". It is then very natural to consider the *fractal variation*, defined for an arbitrary fractal curve as

$$\mathrm{var}_d(\gamma[0,t]) = \lim_{n\to\infty} \sum_{i=1}^{n} |\gamma(t_i) - \gamma(t_{i-1})|^d \tag{4.20}$$

where d is the fractal dimension of γ. Notice that this definition actually depends on the parametrization, and in principle different choices could give different values of var_d.

To define the fractal variation in a parametrization-independent way, but in close analogy with (4.20), one does the following. Fix a scale λ, and let

$t_0 = 0$. The times $\{t_i\}_{i=1\ldots n}$ are defined recursively as follows. Given t_i, let t_{i+1} be the first time after t_i such that $|\gamma(t_{i+1}) - \gamma(t_i)| \geq \lambda$. Then the fractal variation of the whole curve is defined as

$$\mathrm{var}_d(\gamma[0,t]) = \lim_{\lambda \to 0} n\lambda^d \tag{4.21}$$

where n is the largest integer such that $t_n \leq t$. The very existence of this variation can not be established rigorously, but numerical evidence for its convergence has been given in [51]. In practical applications, the fractal dimension d will be computed as $1/\nu$, where ν is the swelling exponent defined in Equation (1.3).

4.4 Comparison

In this section we compare the results of the two methods presented in Sections 4.3.1 and 4.3.2. We are going to compare the results only in the radial whole-plane case, that is for SLE growing from the unit circle to infinity.

Controlling the step length becomes more and more difficult as the parameter κ increases. This is due to the fact that the trace gets more and more entangled (and self-touching for $\kappa > 4$) so that large domains of the complex plane have a higher chance to be mapped to very small regions by the Loewner map. This essentially means that the derivatives of the map fluctuate more and more, thus spoiling the precision of the approximations. We choose to perform the comparisons for the two values $\kappa = 8/3$ and $\kappa = 6$ which lie at different sides of the transition point $\kappa = 4$, and which are relevant for our purposes, since we are going to study these two cases in Chapter 6.

Figure 4.5 is a plot of the step lengths $|\gamma(t_i) - \gamma(t_i - 1)|$ for $\kappa = 8/3$. It compares the two methods (based on the first and the second derivative of the map), together with the results obtained through simple global rescaling as in (3.25). It is just a little section of a much longer chain. The three plots were obtained using the same sequence of signs s_k, so that the three paths actually have the same pattern of right/left turns. The large fluctuations that the naive rescaling shows seem to be much softer in both other reparametrizing methods. The second-derivative curve still retains some correlation with the naive one. On the other hand, the first-derivative step lengths suffer instead from a high self (anti-)correlation, displayed by the oscillations that occur on a time-scale of 2 steps. These might be due to the systematic nature of the error one does in choosing the tentative point where the derivative is computed. The variances of the step lengths (calculated on a much more

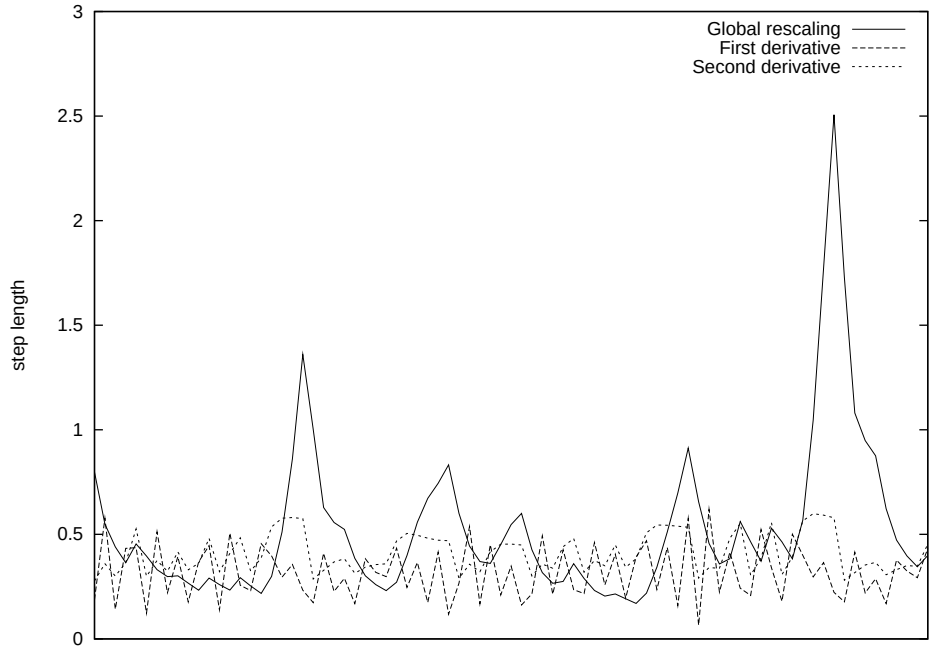

Figure 4.5: The lengths of the discrete steps (in whole-plane SLE), obtained by three different reparametrization methods (here $\kappa = 8/3$).

wide data range than that displayed in figure) are

$$\sigma^2_{|\gamma(t_i)-\gamma(t_i-1)|} = \begin{cases} 0.69(4) & \text{(Global rescaling)} \\ 0.0713(3) & \text{(First derivative)} \\ 0.0196(1) & \text{(Second derivative)} \end{cases}$$

These variances are renormalized on an average step-length of 1, so they represent the entity of the fluctuations with respect to the average.

As far as $\kappa = 8/3$ is concerned, the first- and second-derivative approaches both yield good results in so far as their variances are at least one order of magnitude less than that of the unconstrained steps. Let us now increase the value of κ beyond the critical value 4, thus entering a region where simulations are much harder.

Figure 4.6 displays the same information as above, now for $\kappa = 6$. The first-derivative reparametrization now fails completely, its fluctuations being orders of magnitude larger than those obtained with the globally rescaled parametrization. This is probably due to the oscillating nature of these fluctuations, that now wildly dominate the behavior. On the contrary, the second-derivative approach still yields step lengths whose variance is less than

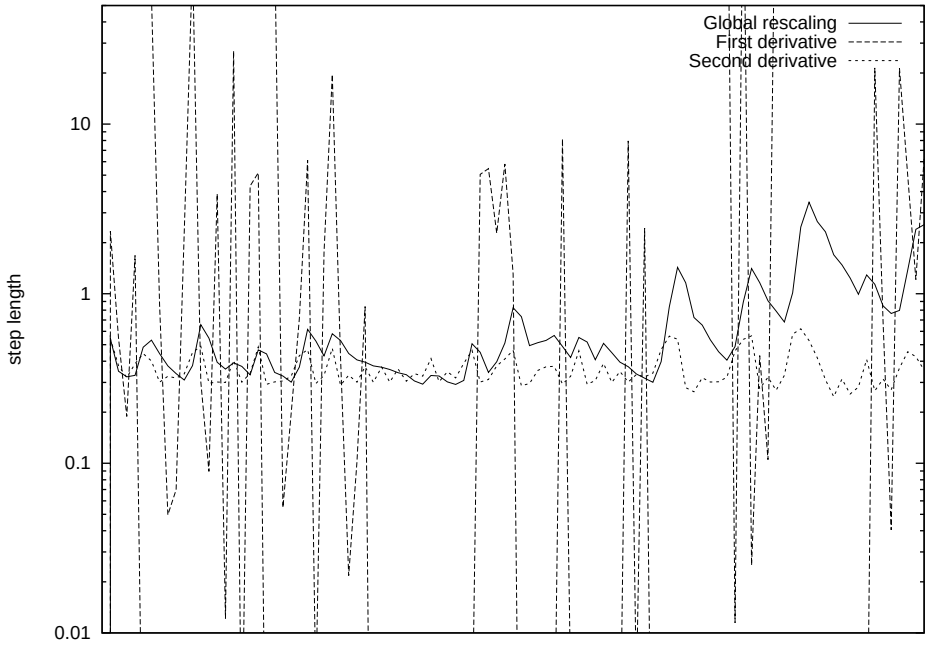

Figure 4.6: The lengths of the discrete steps (in whole-plane SLE), obtained by three different reparametrization methods (here $\kappa = 6$). Notice the logarithmic scale on the y-axis.

that obtained with the naive approach.

$$\sigma^2_{|\gamma(t_i)-\gamma(t_i-1)|} = \begin{cases} 0.76(4) & \text{(Global rescaling)} \\ \sim 10^6 & \text{(First derivative)} \\ 0.038(1) & \text{(Second derivative)} \end{cases}$$

For the second-derivative approach to be used as a tool for simulating SLE, one has to be sure that it actually yields the expected parametrization. It turns out that it does indeed. See Chapter 6 for a check of the distribution functions obtained by this method.

Chapter 5

The θ point

This chapter deals with the end-to-end distribution function of polymers at the θ transition, with the aim of obtaining high-precision estimates of several universal and some non-universal quantities of interest. We perform extensive Monte Carlo simulations and compare the results with theoretical predictions. Material presented here will be published in [52].

5.1 Theoretical results

5.1.1 Critical exponents

We consider three different observables (radii) that measure the size of the walk ω:

- The mean square end-to-end distance

$$R_e^2 \equiv (\omega_N - \omega_0)^2. \tag{5.1}$$

- The mean square radius of gyration

$$\begin{aligned} R_g^2 &\equiv \frac{1}{N+1} \sum_{i=0}^{N} \left(\omega_i - \frac{1}{N+1} \sum_{k=0}^{N} \omega_k \right)^2 \\ &= \frac{1}{2(N+1)^2} \sum_{i,j=0}^{N} (\omega_i - \omega_j)^2. \end{aligned} \tag{5.2}$$

- The mean square monomer distance from an endpoint

$$R_m^2 \equiv \frac{1}{N+1} \sum_{i=0}^{N} (\omega_i - \omega_0)^2. \tag{5.3}$$

Ref.	year	method	β_θ
[69]	1987	EE	0.75
[70]	1988	MC	0.65(3)
[71]	1990	EE	0.67(4)
[72]	1990	MC	0.658(4)
[73]	1992	EE	0.657(16)
[74]	1993	MC	0.658(4)
[75]	1994	EE	0.660(5)
[76]	1995	MC	0.665(2)
[77]	1996	MC	0.664, 0.666
[78]	1997	MC	0.667(1)

Table 5.1: Estimates of β_θ on the square lattice. EE stands for exact enumeration, MC for Monte Carlo.

Correspondingly we define the universal ratios[1] :

$$A_N \equiv \frac{\langle R_g^2 \rangle_N}{\langle R_e^2 \rangle_N}, \qquad B_N \equiv \frac{\langle R_m^2 \rangle_N}{\langle R_e^2 \rangle_N}, \qquad C_N \equiv \frac{\langle R_g^2 \rangle_N}{\langle R_m^2 \rangle_N}. \tag{5.4}$$

Finally, we introduce the specific heat

$$\begin{aligned} c_N(\beta) &\equiv \frac{1}{N} \frac{\partial \langle \mathcal{E} \rangle_N}{\partial \beta^{-1}} \\ &= \frac{\beta^2}{N} \left(\langle \mathcal{E}^2 \rangle_N - \langle \mathcal{E} \rangle_N^2 \right). \end{aligned} \tag{5.5}$$

As is well known, the θ point corresponds to a very specific value β_θ of β, which depends on the microscopic details of the model. For the SAW, the best present-day estimates on the square lattice are reported in Table 5.1.

In a neighborhood of β_θ the radii have a scaling behavior of the form

$$\langle R^2 \rangle_N = N^{2\nu_\theta} f_\pm \left[N^\phi (\beta - \beta_c) \right], \tag{5.6}$$

with $f_\pm(0) \neq 0$. In two dimensions, the universal exponents ϕ and ν_θ are given by [68]

$$\nu_\theta = \frac{4}{7}, \qquad \phi = \frac{3}{7}. \tag{5.7}$$

[1] Of course, knowledge of two of them yields the third.

The crossover exponent ϕ can be measured directly at $\beta = \beta_\theta$ by considering the specific heat, which scales as

$$c_N \sim N^{2\phi-1}, \tag{5.8}$$

or

$$\begin{aligned} D_N &\equiv -\frac{1}{\langle R^2\rangle_N}\frac{d\langle R^2\rangle_N}{d\beta} \\ &= \langle \mathcal{E}\rangle_N - \frac{\langle R^2\mathcal{E}\rangle_N}{\langle R^2\rangle_N} \sim N^\phi, \end{aligned} \tag{5.9}$$

where R^2 is one of the radii.

We also introduce the exponent γ_θ that controls the large N-behavior of the partition function

$$Z_N \sim \mu^N N^{\gamma_\theta - 1}. \tag{5.10}$$

Here μ is a lattice- and model-dependent constant, while γ_θ is universal, $\gamma_\theta = 8/7$.

Finally, we mention a general relation (which will henceforth be called CSCPS) that has been proved for noniteracting SAWs [54, 53] and which has been conjectured to hold at the θ-point too [75]. If we define

$$F_N = \left(2 + \frac{2}{\gamma_\theta + 2\nu_\theta}\right) A_N - 2B_N + \frac{1}{2}, \tag{5.11}$$

then, it is conjectured that $F_\infty = 0$.

5.1.2 End-to-end distribution function

We consider a monodisperse ensemble of polymers with N monomers. If $\mathbf{r}$ is the vector joining the endpoints of the walk, we will be interested in computing the unnormalized distribution $c_N(\mathbf{r})$ of the endpoint vector[1]. We also introduce a normalized distribution

$$P_N(\mathbf{r}) = \frac{c_N(\mathbf{r})}{\sum_r c_N(\mathbf{r})}\ , \tag{5.12}$$

the mean squared end-to-end distance

$$R^2_{e,N} = \sum_r |\mathbf{r}|^2 P_N(\mathbf{r}), \tag{5.13}$$

[1] In continuum models, the function $c_N(\mathbf{r})$ is not well defined. For models regularized on a lattice, $c_N(\mathbf{r})$ can be identified with the number of walks starting at the origin and ending in $\mathbf{r}$.

and the related correlation length

$$\xi_N^2 = \frac{1}{2d} R_{e,N}^2. \tag{5.14}$$

In the limit $N \to \infty$, $|\mathbf{r}| \to \infty$, with $|\mathbf{r}|N^{-\nu}$ fixed, the function $P_N(\mathbf{r})$ has the scaling form [61, 62, 63]

$$P_N(\mathbf{r}) \approx \frac{1}{\xi_N^d} f(\rho) \left[1 + O(N^{-\Delta})\right], \tag{5.15}$$

where $\boldsymbol{\rho} = \mathbf{r}/\xi_N$, $\rho = |\boldsymbol{\rho}|$, d is the space dimensionality, and Δ is a correction-to-scaling exponent. By definition

$$\int_0^\infty \rho^{d-1} d\rho \, f(\rho) = \frac{1}{S_d}, \tag{5.16}$$

$$\int_0^\infty \rho^{d+1} d\rho \, f(\rho) = \frac{2d}{S_d}, \tag{5.17}$$

where S_d is the volume of the d-dimensional sphere

$$S_d = \frac{2\pi^{d/2}}{\Gamma(d/2)} . \tag{5.18}$$

Several facts are known about $f(\rho)$. For large values of ρ it behaves as [60, 61, 62, 63]

$$f(\rho) \approx f_\infty \rho^\sigma \exp\left(-D\rho^\delta\right), \tag{5.19}$$

where σ and δ are given by

$$\delta = \frac{1}{1-\nu}, \tag{5.20}$$

$$\sigma = \frac{2\nu d - 2\gamma + 2 - d}{2(1-\nu)}. \tag{5.21}$$

For $\rho \to 0$, we have [62, 63]

$$f(\rho) \approx f_0 \left(\frac{\rho}{2}\right)^\theta, \tag{5.22}$$

where

$$\theta = \frac{\gamma - 1}{\nu} . \tag{5.23}$$

We can also consider the Fourier transform of $f(\rho)$,

$$\widetilde{f}(\mathbf{Q}) = \int \frac{d^d\boldsymbol{\rho}}{(2\pi)^d} e^{i\mathbf{Q}\cdot\boldsymbol{\rho}} f(\rho), \tag{5.24}$$

which is the critical (large-N) limit of $\widetilde{c}_N(\mathbf{q})/\widetilde{c}_N(\mathbf{0})$ with $\mathbf{Q} \equiv \mathbf{q}\xi_N$ fixed, $\widetilde{c}_N(\mathbf{q})$ being the Fourier transform of $c_N(\mathbf{r})$. For $Q \to 0$, $\widetilde{f}(Q)$ has a regular expansion in powers of Q^2, while for $Q^2 \to \infty$ it behaves as

$$\widetilde{f}(Q) = \widetilde{f}_\infty Q^{-\theta-d}. \tag{5.25}$$

The constants $\widetilde{f}_\infty$ and f_0 are related. Indeed

$$f_0 = \widetilde{f}_\infty \, (4\pi)^{-d/2} \frac{\Gamma\left(-\frac{\theta}{2}\right)}{\Gamma\left(\frac{\theta+d}{2}\right)}. \tag{5.26}$$

For the purpose of computing D and δ from Monte Carlo data, it is much easier to consider the "wall-to-wall" distribution function

$$P_{N,w}(x) = \sum_{x_2,\ldots,x_d} P_N(x, x_2, \ldots, x_d), \tag{5.27}$$

which represents the probability that the endpoint of the walk lies on a plane at a distance x from the origin of the walk. In the large-N limit, $P_{N,w}(x)$ has the scaling form

$$P_{N,w}(x) = \frac{1}{\xi_N} f_w(\rho) \left(1 + O(N^{-\Delta})\right), \qquad \rho = \frac{|x|}{\xi_N}. \tag{5.28}$$

For large ρ we have

$$f_w(\rho) \approx f_{w,\infty} \rho^{\sigma_w} \exp(-D\rho^\delta) \, , \tag{5.29}$$

where δ is given by (5.20), D is the same constant appearing in Eq. (5.19), and

$$\sigma_w = \delta \left(\nu - \gamma + \frac{1}{2}\right). \tag{5.30}$$

5.1.3 Phenomenological expression

A phenomenological representation for the function $f(\rho)$ has been proposed by McKenzie and Moore [62] and des Cloizeaux [55]:

$$f(\rho) \approx f_{\rm ph}(\rho) = f_{\rm ph} \rho^{\theta_{\rm ph}} \exp\left(-D_{\rm ph} \rho^{\delta_{\rm ph}}\right). \tag{5.31}$$

Here $\delta_{\rm ph}$ and $\theta_{\rm ph}$ are free parameters, while $f_{\rm ph}$ and $D_{\rm ph}$ are fixed by the normalization conditions (5.16) and (5.17):

$$D_{\rm ph} = \left\{ \frac{\Gamma[(1-\nu)(2+d+\theta_{\rm ph})]}{2d\,\Gamma[(1-\nu)(d+\theta_{\rm ph})]} \right\}^{\frac{\delta_{\rm ph}}{2}}, \tag{5.32}$$

$$f_{\rm ph} = \frac{\delta_{\rm ph} D_{\rm ph}^{(d+\theta_{\rm ph})(1-\nu)}}{S_d\,\Gamma[(1-\nu)(d+\theta_{\rm ph})]} \, . \tag{5.33}$$

5.1.4 Internal points distribution function

Beside the endpoint distribution function one may consider the probability $P_{N,M}(\vec{r})$ that $\omega_M - \omega_0 = \vec{r}$, where ω_M is an internal point, i.e. $M < N$. Then, consider the limit $N, M \to \infty$, $\vec{r} \to \infty$ with $rN^{-\nu}$ and M/N fixed. We obtain

$$P_{N,M}(\vec{r}) \approx \frac{1}{\xi_M^d} f_{\rm int}(r/\xi_M, M/N), \tag{5.34}$$

where $\xi_M^2 = (\omega_M - \omega_0)^2/(2d)$. For $\rho \to 0$ and $M/N \neq 0, 1$, we have

$$f_{\rm int}(\rho, M/N) \sim \rho^{\theta_{\rm int}} \tag{5.35}$$

where the exponent is independent of M/N. The exponent $\theta_{\rm int}$ has been computed exactly in two dimensions, obtaining $\theta_{\rm int} = 5/6$ for noninteracting SAWs and $\theta_{\rm int} = 5/12$ at the θ point. Such an exponent can be determined by measuring the probability $P_N^{\rm ENN}$ that the endpoint is a nearest neighbor of the walk, i.e. $c_{iN} = 1$ for some $i < N - 1$. By adding an analytic background, due to local interactions that are not taken into account in the previous analytic behavior, we can write

$$P_N^{\rm ENN} \approx a + \frac{b}{N} + \frac{c}{N^{\nu(d+\theta_{\rm int})-1}} + \dots \tag{5.36}$$

At the θ point this gives

$$P_N^{\rm ENN} \approx a + \frac{b}{N} + \frac{c}{N^{8/21}}, \tag{5.37}$$

while for noninteracting SAWs the analytic correction is the dominant one

$$P_N^{\rm ENN} \approx a + \frac{b}{N} + \frac{c}{N^{9/8}}. \tag{5.38}$$

5.1.5 Gyration tensor

Typically, the shape of a polymer is not spherical. In order to characterize this asymmetry it is customary to consider the gyration tensor defined by

$$Q_{N,\alpha\beta} = \frac{1}{2(N+1)^2} \sum_{i,j=0}^{N} (\omega_{i,\alpha} - \omega_{j,\alpha})(\omega_{i,\beta} - \omega_{j,\beta}), \tag{5.39}$$

which is such that $\mathrm{Tr}\, Q_N = R_{g,N}^2$. The relevant quantities are the eigenvalues q_α, that are expected to scale as

$$\langle q_\alpha \rangle_N \approx B_\alpha N^{2\nu_\theta}, \tag{5.40}$$

for $N \to \infty$, and, more generally, obey a scaling law of the form

$$P_N(q_\alpha) = \frac{1}{\langle q_\alpha \rangle_N} F_\alpha \left(\frac{q_\alpha}{\langle q_\alpha \rangle_N} \right). \tag{5.41}$$

To characterize the shape, one also considers the asphericity

$$\mathcal{A}_N = \frac{1}{d(d-1)} \sum_{\alpha=1}^{d} \left\langle \frac{(q_\alpha - \bar{q})^2}{\bar{q}^2} \right\rangle_N, \tag{5.42}$$

where $\bar{q} = \sum_\alpha q_\alpha / d = R^2_{g,N}/d$.

5.2 Numerical results

We have performed extensive simulations using a Monte Carlo algorithm that uses reptation moves and bilocal moves. It is described in detail in Ref. [67]. For the simulation we have fixed $\beta = 0.665$, which is the estimate of Ref. [76] of β_θ, and performed runs for walk lengths $N = 100, 800, 1600, 3200$.

5.2.1 Critical exponents and reweighting

Results for several observables of interest are reported in Table 5.2 together with accurate error estimates (in parentheses).

In order to determine ν_θ we have performed a fit of $\langle R^2 \rangle_N$ to the ansatz $aN^{2\nu_\theta}$ with and without the data for $N = 100$. The results are in Table 5.3. These estimates are close to the theoretical prediction $\nu_\theta = 4/7 \approx 0.5714\ldots$, but the data apparently overshoot. One may think this is due to the fact that $\beta = 0.665 < \beta_\theta$ so that we are seeing the beginning of the crossover towards the good-solvent value $\nu = 3/4$. To verify this hypothesis, we have computed the mean values for other β values using the standard reweighting technique. In particular, we have computed $\langle R^2 \rangle_N$ for $\beta = 0.665 - 0.0005n$, $n = 1, 2, 3, 4$. All these points should lie in the high-temperature phase and should scale as

$$\langle R^2 \rangle_N = aN^{2\nu_\theta} + bN^{2\nu_\theta + \phi}(\beta - \beta_\theta), \tag{5.43}$$

valid for $N^\phi(\beta - \beta_\theta) \lesssim 1$. Fits performed by letting all five parameters run or by fixing the two exponents to their theoretical values — both with the full range of N and with data restricted to $N_{\min} = 800$ — yield similar results for β_θ, which are reported in Table 5.4[1]. Our final estimate is

[1] Errors are to be taken with a grain of salt, since they are computed from a non-linear two-variable iterative fit, and tend to be over-optimistic.

N	$\langle R_g^2 \rangle_N$	$\langle R_e^2 \rangle_N$	$\langle R_m^2 \rangle_N$	$\langle \mathcal{E} \rangle_N$	$\langle \mathcal{E}^2 \rangle_N - \langle \mathcal{E} \rangle_N^2$
100	43.4385(75)	241.874(71)	123.024(26)	46.3044(24)	68.095(16)
800	472.72(30)	2604(3)	1332(1)	429.712(26)	909.53(60)
1600	1050.19(37)	5784(3)	2957(1)	877.717(21)	2034.49(68)
3200	2338.7(1.5)	12895(13)	6584(5)	1780.259(53)	4460.2(2.5)

N	A_N	B_N	C_N	D_N
100	0.179592(61)	0.50863(18)	0.35309(97)	2.2793(15)
800	0.18152(22)	0.51139(64)	0.35496(35)	6.826(15)
1600	0.18156(12)	0.51123(35)	0.35514(19)	9.54(1)
3200	0.18137(21)	0.51060(63)	0.35521(35)	13.170(29)

Table 5.2: Results for $\langle R_g^2 \rangle_N$, $\langle R_e^2 \rangle_N$, $\langle R_m^2 \rangle_N$, $\langle \mathcal{E} \rangle_N$, $\langle \mathcal{E}^2 \rangle_N - \langle \mathcal{E} \rangle_N^2$, A_N, B_N, C_N, D_N.

$N_{\min}$	ν_θ (from R_g^2)	ν_θ (from R_e^2)	ν_θ (from R_m^2)
100	0.5746(3)	0.5727(6)	0.5736(4)
800	0.5767(7)	0.5770(10)	0.5764(8)

Table 5.3: Estimates of ν_θ at $\beta = 0.665$.

$$\beta_\theta = 0.667(1) \tag{5.44}$$

Better results for ν_θ can then be obtained by performing a fit on the reweighted data at $\beta = 0.667$; see Table 5.5.

In order to compute the crossover exponent we have analyzed D_N and c_N. The fit results are reported in Table 5.6. Corrections to scaling are emerging to some extent here, but since no error can be computed when $N_{\min} = 800$ (for the number of data points equals the number of free parameters) their strength is difficult to guess. Nonetheless, there seems to be good agreement with the expected value $\phi_\theta = 0.428\ldots$

Finally, we have tested the CSCPS relation, obtaining the results in Table 5.7. Results are all compatible with the expected asymptotic value $F_\infty = 0$ (except perhaps F_{100}). The result obtained by including all data with $N \geq 1600$ is

$$F_\infty = 0.0021(48). \tag{5.45}$$

	$N_{\min}$	ν	ϕ	β_θ	β_θ (fixed exponents)
R_g	100	0.5720(2)	0.480(4)	0.6669(1)	0.6675(1)
	800	0.5721(2)	0.480(5)	0.6669(1)	0.6675(1)
R_e	100	0.5678(3)	0.480(5)	0.6677(1)	0.6670(1)
	800	0.5683(3)	0.480(5)	0.6676(1)	0.6670(1)
R_m	100	0.5706(3)	0.478(6)	0.6672(1)	0.6671(1)
	800	0.5711(3)	0.478(5)	0.6670(1)	0.6671(1)

Table 5.4: Estimates of exponents and critical temperature obtained from reweighted data.

ν_θ (from R_g^2)	ν_θ (from R_e^2)	ν_θ (from R_m^2)
0.5708(3)	0.5720(1)	0.5712(1)

Table 5.5: Estimates of ν_θ from reweighted data at $\beta = 0.667$.

5.2.2 End-to-end distribution function

We have studied the EEDF closely following the strategy employed in Ref. [66] to analyze the same quantity for non-interacting SAWs. In principle we should correct for the estimate of β_θ obtained in Section 5.2.1. However, the error is negligible on the EEDF and thus we will analyze the results for $\beta = 0.665$ without additional corrections.

First, we have considered the wall-wall distribution $f_w(\rho)$ — see Eq. (5.28) — and we have performed two different fits

$$\ln f_w(\rho) = \ln f_{w,\infty} - D\rho^\delta, \tag{5.46}$$

$$\ln(\rho^{1/6} f_w(\rho)) = \ln f_{w,\infty} - D\rho^\delta. \tag{5.47}$$

In the second fit we have used the theoretical prediction for σ_w. In order to detect corrections to scaling, we have repeated the fit for each $N = 100, 800, 1600, 3200$. Moreover, Eqs. (5.46) and (5.47) are valid only for $\rho \to \infty$ and thus we have included in each case only the data with $\rho \geq \rho_{\min}$, for $\rho_{\min} = 2, 2.5, 3$. Finally, corrections to scaling increase with ρ, and thus we have also studied the dependence of the results on the upper cutoff $\rho_{\max} = 4, 5, 6$. Results obtained with the first ansatz (5.46) are reported in Table 5.8; a plot of the curves is in Fig. 5.1.

Two features are manifest. Firstly, a mild systematic dependence on N is evident, if one neglects the results for $N = 100$ which are always op-

$N_{\min}$	ϕ_θ (from c_N)	ϕ_θ (from D_N)
100	0.450(4)	0.436(5)
800	0.430	0.416

Table 5.6: Estimates of ϕ_θ. The values for $N_{\min} = 800$ have no error because there are as many fit parameters as data.

N	F_N
100	0.0052(28)
800	0.0050(97)
1600	0.0026(53)
3200	-0.0007(120)

Table 5.7: CSCPS values.

posite to the trend; the curve at $N = 100$ is also visibly less close to the asymptotic regime (especially where ρ is small). As expected, these corrections become more important as $\rho_{\max}$ increases, but values are nonetheless consistent within error bars, at least for the greater values of N. Secondly, data apparently do not display any systematic dependence on either $\rho_{\min}$ or $\rho_{\max}$, and the very slight drift in $\rho_{\min}$ that is visible for certain choices of the parameters gets completely lost in the noise. Fits become more and more unstable as $\rho_{\min}$ and $\rho_{\max}$ increase, especially in the regime $\rho_{\min} \gtrsim 3.5$, $\rho_{\max} \gtrsim 6$ (not shown here). Our final estimates are obtained by fitting all data with $N \geq 800$ in the window $3 \leq \rho \leq 5$.

From the first fit, we obtain finally

$$\delta = 2.354(24) \qquad D = 0.163(7), \tag{5.48}$$

while from the second one (results with $\rho_{\max} = 5$ are in Table 5.9)

$$\delta = 2.395(24) \qquad D = 0.149(7). \tag{5.49}$$

In order to estimate $f_{w,\infty}$, we cannot neglect the multiplicative factor ρ^{σ_w} and thus only the results of the second fit are relevant. We obtain

$$f_{w,\infty} = 0.562(24). \tag{5.50}$$

The results for the exponent δ should be compared with the theoretical value $\delta = 7/3 = 2.33\ldots$ The second fit yields an overestimated value, but Table 5.9

N	$\rho_{\max}$	$\rho_{\min}$	δ	D
100	4	2	2.517(3)	0.127(1)
		2.5	2.516(6)	0.128(1)
		3	2.501(21)	0.131(5)
	5	2	2.466(6)	0.142(1)
		2.5	2.483(7)	0.138(2)
		3	2.504(13)	0.133(3)
	6	2	2.565(14)	0.117(3)
		2.5	2.579(19)	0.114(4)
		3	2.601(29)	0.109(6)
800	4	2	2.394(12)	0.148(3)
		2.5	2.392(26)	0.149(6)
		3	2.410(82)	0.144(20)
	5	2	2.318(9)	0.173(3)
		2.5	2.319(15)	0.173(5)
		3	2.305(29)	0.177(9)
	6	2	2.378(20)	0.153(6)
		2.5	2.372(28)	0.155(8)
		3	2.361(43)	0.158(13)
1600	4	2	2.426(5)	0.141(1)
		2.5	2.423(11)	0.142(2)
		3	2.390(30)	0.150(8)
	5	2	2.353(7)	0.164(2)
		2.5	2.358(12)	0.162(3)
		3	2.358(21)	0.162(6)
	6	2	2.414(15)	0.144(4)
		2.5	2.418(21)	0.142(6)
		3	2.430(32)	0.139(9)
3200	4	2	2.455(11)	0.135(2)
		2.5	2.426(24)	0.142(6)
		3	2.423(77)	0.142(18)
	5	2	2.371(15)	0.159(4)
		2.5	2.368(24)	0.160(7)
		3	2.375(45)	0.158(13)
	6	2	2.469(31)	0.132(8)
		2.5	2.468(43)	0.132(11)
		3	2.493(67)	0.125(16)

Table 5.8: Fit results for the wall-wall EEDF. Fit function (5.46).

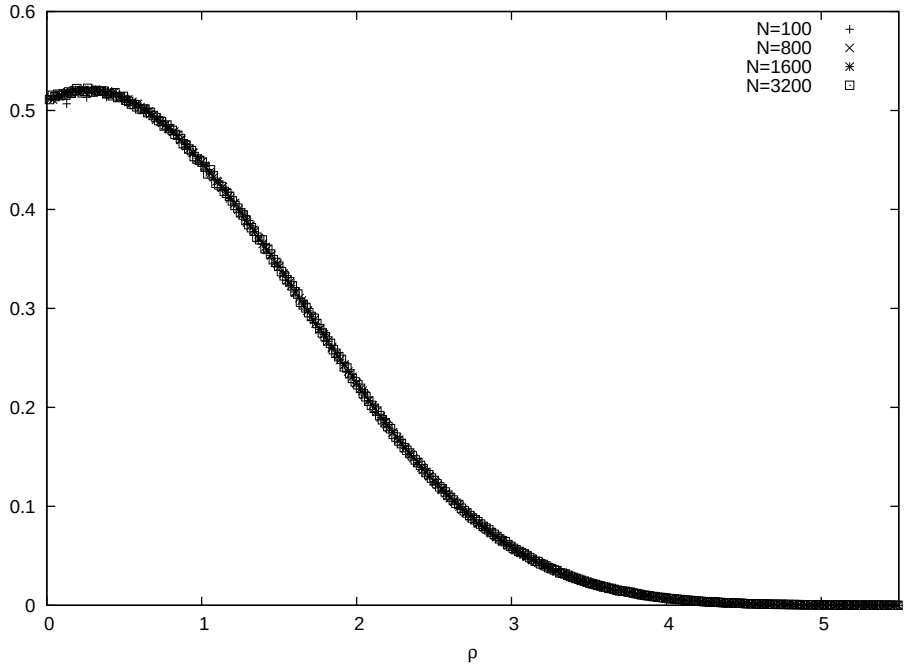

Figure 5.1: The renormalized wall-wall EEDF.

shows that the non-asymptotic corrections — which were absent in the first fit — are now present and dragging it towards the expected limit. The two values of D are not compatible with each other; however, the second value is again affected by corrections in $\rho_{\min}$ that are pushing it towards the other value. A precise estimate of the systematic errors is hard here, since corrections to scaling and non-asymptotic corrections have different signs. But there is evidence that one should trust the first fit more, since it does display less dependence on the cut-off, and it yields a better value of δ, so it probably works better for D as well.

Let us consider now the radial distribution $f(\rho)$ — see Eq. (5.15). From the Monte Carlo data we can estimate $\hat{P}_N(\vec{r})$, which is the probability that the endpoint is in $\vec{r}$. This quantity is not well suited for the analysis because of fluctuations due to the lattice structure. In order to average them out, we will use a trick, already used in this context in Refs. [64, 65, 66]. We shall

N	$\rho_{\min}$	δ	D	$\log f_{w,\infty}$
100	2	2.527(4)	0.125(1)	0.640(5)
	2.5	2.533(7)	0.124(2)	0.649(9)
	3	2.545(13)	0.121(3)	0.670(2)
800	2	2.377(10)	0.153(3)	0.577(13)
	2.5	2.366(16)	0.156(4)	0.560(23)
	3	2.345(30)	0.162(9)	0.520(53)
1600	2	2.412(7)	0.145(2)	0.607(9)
	2.5	2.406(12)	0.146(3)	0.598(17)
	3	2.397(22)	0.149(6)	0.581(37)
3200	2	2.431(15)	0.140(4)	0.620(18)
	2.5	2.417(24)	0.144(6)	0.599(35)
	3	2.417(46)	0.144(12)	0.598(78)

Table 5.9: Fit results for the wall-wall EEDF. Fit function (5.47). ($\rho_{\max} = 5$).

consider two different averages

$$\hat{P}^{(\mathrm{av})}_{1,N}(r_{1,n}) = \frac{1}{2N_{1,n}(r_{1,n})} \sum_{\vec{r}: r^2_{1,n-1} < r^2 \le r^2_{1,n}} \hat{P}_N(\vec{r}), \tag{5.51}$$

$$\hat{P}^{(\mathrm{av})}_{2,N}(r_{2,n}) = \frac{1}{2N_{2,n}(r_{2,n})} \sum_{\vec{r}: r^2_{2,n-1} < r^2 \le r^2_{2,n}} \hat{P}_N(\vec{r}), \tag{5.52}$$

where $r_{1,n} = r_0 + n\Delta$, $r^2_{2,n} = r^2_0 + n\Delta$ where r_0 and Δ are fixed parameters[1], and $N_{1,n}(r_{1,n})$ and $N_{2,n}(r_{2,n})$ are the number of lattice points with the same parity[2] of N that lie in the considered shell. For Δ fixed, $\hat{P}_N(\vec{r})$, $\hat{P}^{(\mathrm{av})}_{1,N}(r)$ and $\hat{P}^{(\mathrm{av})}_{2,N}(r)$ have the same scaling behavior as $N \to \infty$. For practical purposes, we measure Δ in units of the correlation length: we define $\Lambda = \Delta/\xi_N$ and keep it fixed for all N. The curves in Figure 5.2 are obtained with (5.51) and $\Lambda = 1/15$.

In order to determine the parameters D and δ we have performed a fit of the form

$$\log f(\rho) = \log f_\infty - D\rho^\delta \tag{5.53}$$

[1]Procedure (5.51) corresponds to fixing the width of the annuli on which the average is computed, while (5.52) corresponds to fixing the volume.

[2]A point (x, y) is odd (resp. even) if $x + y$ is odd (resp. even).

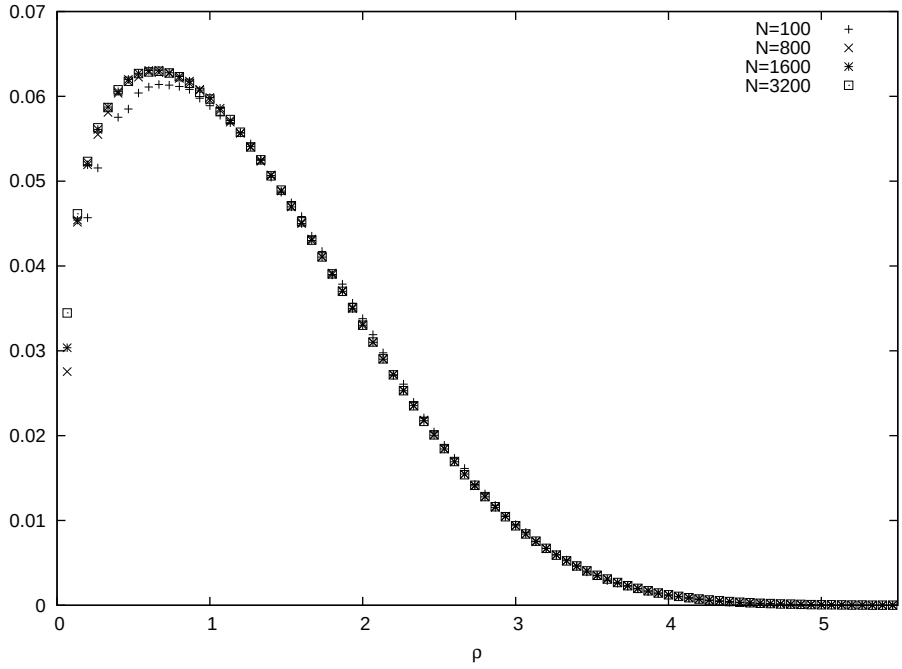

Figure 5.2: The renormalized EEDF.

for each N and for several $\rho_{\min}$ and Λ. Note that in this case theory predicts $\sigma = 0$ and thus this fit allows us to determine f_∞ too. Results are in Tables 5.10 and 5.11. An oscillating behavior in N is now visible, and again the data for $N = 100$ appear largely out of the scaling regime (this is visible also in Figure 5.2). Since no systematic corrections are apparent, the final results are obtained by including in the fit only walks with $N \geq N_{\min}$, where $N_{\min}$ is chosen so that the estimates for all $N \geq N_{\min}$ are independent of N within error bars. Instead, non-asymptotic corrections are much more pronounced than they were for $f_w(\rho)$. For this reason, in final results we choose to keep the fit window as far into the asymptotic regime as it is allowed by instability and errors ($\rho_{\min} = 3.5$). The upper cutoff $\rho_{\max}$ in Tables 5.10 and 5.11 is chosen so as to be the last ρ before the sampled distribution function takes on its first null value. Clearly, for fixed N, $\rho_{\max}$ depends on the smoothing function and on Δ. In the final results $\rho_{\max}$ is the min over the distributions merged.

Λ	N	$\rho_{\max}$	$\rho_{\min}$	δ	D	$\log f_\infty$
1/5	100	7	2	2.613(23)	0.103(5)	2.710(50)
			2.5	2.613(31)	0.103(7)	2.710(77)
			3	2.613(40)	0.103(8)	2.71(11)
			3.5	2.596(60)	0.107(13)	2.65(19)
	800	6.7	2	2.350(25)	0.156(8)	2.513(52)
			2.5	2.317(33)	0.167(11)	2.420(82)
			3	2.285(42)	0.178(15)	2.32(12)
			3.5	2.209(62)	0.210(28)	2.04(21)
	1600	7.2	2	2.400(13)	0.142(4)	2.585(30)
			2.5	2.390(17)	0.145(5)	2.556(46)
			3	2.383(21)	0.147(7)	2.530(63)
			3.5	2.365(31)	0.153(10)	2.46(11)
	3200	7.2	2	2.381(25)	0.147(7)	2.560(60)
			2.5	2.367(33)	0.151(10)	2.514(91)
			3	2.357(41)	0.155(14)	2.48(13)
			3.5	2.336(62)	0.162(22)	2.40(22)
1/15	100	7	2	2.597(51)	0.110(11)	2.74(11)
			2.5	2.597(67)	0.110(15)	2.74(17)
			3	2.592(89)	0.111(20)	2.72(25)
			3.5	2.59(13)	0.111(30)	2.72(41)
	800	7	2	2.355(32)	0.158(10)	2.566(75)
			2.5	2.340(42)	0.163(14)	2.52(11)
			3	2.323(56)	0.170(20)	2.46(17)
			3.5	2.296(83)	0.180(32)	2.35(30)
	1600	7.2	2	2.381(13)	0.150(4)	2.610(32)
			2.5	2.375(17)	0.153(5)	2.588(47)
			3	2.366(22)	0.155(7)	2.558(70)
			3.5	2.351(32)	0.161(11)	2.50(11)
	3200	7.2	2	2.368(35)	0.154(11)	2.589(80)
			2.5	2.355(47)	0.159(15)	2.55(12)
			3	2.340(63)	0.164(21)	2.50(19)
			3.5	2.317(95)	0.172(34)	2.42(32)

Table 5.10: Fit results for the large-distance behavior of the radial EEDF obtained with fixed-width averaging (5.51).

Λ	N	$\rho_{\max}$	$\rho_{\min}$	δ	D	$\log f_\infty$
1/15	100	7	2	2.614(63)	0.107(14)	2.66(16)
			2.5	2.614(77)	0.108(17)	2.66(21)
			3	2.615(93)	0.107(21)	2.60(28)
			3.5	2.60(13)	0.110(30)	2.61(42)
	800	7	2	2.346(49)	0.162(16)	2.43(13)
			2.5	2.331(60)	0.167(21)	2.38(18)
			3	2.317(73)	0.173(27)	2.33(24)
			3.5	2.29(10)	0.181(39)	2.24(37)
	1600	7.3	2	2.393(24)	0.148(7)	2.513(70)
			2.5	2.393(29)	0.148(9)	2.513(90)
			3	2.393(36)	0.148(11)	2.51(12)
			3.5	2.379(48)	0.154(16)	2.46(18)
	3200	6.95	2	2.353(30)	0.160(10)	2.446(80)
			2.5	2.340(36)	0.164(12)	2.40(11)
			3	2.327(45)	0.170(16)	2.36(14)
			3.5	2.305(62)	0.177(24)	2.27(22)
1/30	100	6.7	2	2.620(31)	0.106(7)	2.764(71)
			2.5	2.620(37)	0.106(8)	2.764(92)
			3	2.620(49)	0.106(11)	2.76(13)
			3.5	2.626(69)	0.105(15)	2.78(21)
	800	6.6	2	2.340(31)	0.165(10)	2.528(75)
			2.5	2.327(37)	0.170(13)	2.49(10)
			3	2.305(50)	0.177(18)	2.42(15)
			3.5	2.271(73)	0.191(29)	2.29(25)
	1600	7	2	2.360(33)	0.159(11)	2.560(89)
			2.5	2.352(39)	0.161(13)	2.53(11)
			3	2.335(51)	0.167(18)	2.47(16)
			3.5	2.308(72)	0.177(27)	2.37(26)
	3200	6.6	2	2.373(44)	0.155(13)	2.58(10)
			2.5	2.374(53)	0.155(17)	2.58(14)
			3	2.350(72)	0.163(24)	2.51(21)
			3.5	2.33(10)	0.171(38)	2.42(34)

Table 5.11: Fit results for the large-distance behavior of the radial EEDF obtained with fixed-volume averaging (5.52).

With the first averaging procedure (5.51) we obtain

$$\delta = \begin{cases} 2.356(41) & \Lambda = 1/5 \\ 2.333(40) & \Lambda = 1/15 \end{cases} \tag{5.54}$$

$$D = \begin{cases} 0.156(13) & \Lambda = 1/5 \\ 0.167(15) & \Lambda = 1/15 \end{cases} \tag{5.55}$$

$$f_\infty = \begin{cases} 0.086(12) & \Lambda = 1/5 \\ 0.085(12) & \Lambda = 1/15 \end{cases} \tag{5.56}$$

while the second averaging procedure (5.52) yields

$$\delta = \begin{cases} 2.325(43) & \Lambda = 1/15 \\ 2.344(46) & \Lambda = 1/30 \end{cases} \tag{5.57}$$

$$D = \begin{cases} 0.170(16) & \Lambda = 1/15 \\ 0.165(16) & \Lambda = 1/30 \end{cases} \tag{5.58}$$

$$f_\infty = \begin{cases} 0.098(16) & \Lambda = 1/15 \\ 0.084(13) & \Lambda = 1/30 \end{cases} \tag{5.59}$$

As expected, results obtained with different smoothing procedures and different values of Λ are compatible. Finally, a weighted average of the foregoing yields

$$\delta = 2.340(46) \quad D = 0.164(16) \quad f_\infty = 0.088(16), \tag{5.60}$$

where errors in parentheses are computed as the maximum over those of the estimates above (they are not the usual deviations from the weighted average), because results obtained with different averaging procedures and different Λ are not independent. The exponent δ is in perfect agreement with theory and D matches the value obtained through the analysis of f_w to a striking precision.

We can also obtain improved estimates of D, f_∞, and $f_{w,\infty}$ by fixing δ to its theoretical value $\delta = 7/3$. From the analysis of the wall-wall EEDF, using fit function (5.47), we obtain

$$D = 0.1668(3) \qquad f_{w,\infty} = 0.6250(44), \tag{5.61}$$

while from the radial distribution function we have

$$D = 0.1656(3) \qquad f_\infty = 0.0881(15). \tag{5.62}$$

n_{discard}	θ ($\Lambda = 1/50$)	θ ($\Lambda = 1/150$)
0	0.312(24)	0.296(11)
1	0.252(7)	0.278(12)
2	0.251(10)	0.257(11)
3	0.264(11)	0.243(10)

Table 5.12: Values of θ obtained by fitting data after discarding n_{discard} non-zero semples near the origin. Here $\rho_{\max} = 1.5$.

Results obtained from the wall-wall distribution function are less consistent and precise, but again this can be due to corrections. On the other hand, improved estimates from radial EEDF sharply agree with previous results (5.48) and (5.60) obtained from fits with δ as a free parameter.

We consider now the behavior for $\rho \to 0$, performing fits of the form

$$\log f(\rho) = \log f_1 + \theta \log \rho. \tag{5.63}$$

Since Eq. (5.63) is valid only for $\rho \to 0$ and for $r \to \infty$ (scaling limit) data must be analyzed in a window $\rho_{\min} \leq \rho \leq \rho_{\max}$. We also checked consistence of results for different values of the smoothing parameter Λ. Only data for $N = 3200$ has proved useful, since the forthcoming analysis gives very blurry results for smaller values of N.

Fixing the cut-offs is a twofold process. Firstly, we fix $\rho_{\max}$ and study the behavior of the results as functions of $\rho_{\min}$. We do this by controlling the number of non-zero data samples that get discarded after cutting off the small-ρ region. Values of θ for several cut-offs are reported in Table 5.12. It is evident that the first few samples (depending on Λ) are plagued by lattice effects, so they will be discarded (we choose $n_{\text{discard}} = 1$ for $\Lambda = 1/50$ and $n_{\text{discard}} = 2$ for $\Lambda = 1/150$). The second step is then to study how results depend on the upper cut-off, with $\rho_{\min}$ fixed by the foregoing analysis. A plot of θ versus $\rho_{\max}$ is shown in Figure 5.3. The plot shows a large amount of noise in the small-$\rho_{\max}$ region, due to the small number of samples that get involved in the fit. As the number of samples increases, θ reaches a plateaux, after which it starts to drop, because of deviations from linearity. We therefore choose as a cut-off the first $\rho_{\max}$ in the plateaux, finally obtaining

$$\theta = \begin{cases} 0.252(7) & \Lambda = 1/50 \\ 0.257(10) & \Lambda = 1/150 \end{cases} \tag{5.64}$$

$$f_1 = \begin{cases} 0.0807(12) & \Lambda = 1/50 \\ 0.0824(18) & \Lambda = 1/150 \end{cases} \tag{5.65}$$

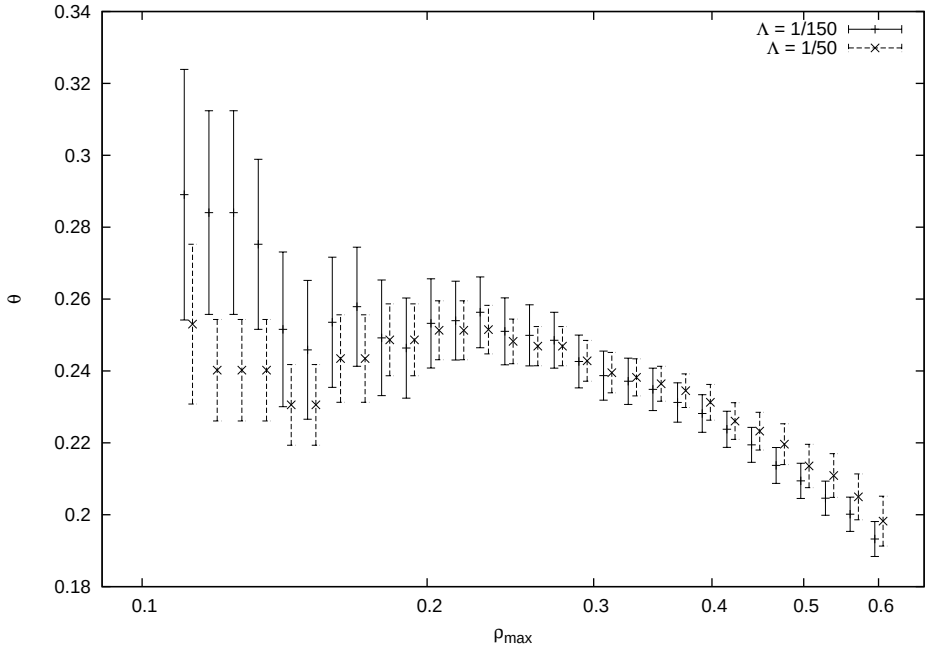

Figure 5.3: Exponent θ obtained from fits as a function of the upper cut-off, for 2 values of Λ. (Notice the logarithmic scale on the X-axis).

The results for θ are in perfect agreement with the theoretical prediction $\theta = 1/4$. An improved estimate of f_1 can be obtained by fixing θ to its theoretical value:

$$f_1 \quad = \quad \begin{cases} 0.0806(2) & \Lambda = 1/50 \\ 0.0813(4) & \Lambda = 1/150 \end{cases} \tag{5.66}$$

Finally, we computed the moments

$$M_{2k,N} = \frac{\sum_{\vec{r}} |r|^{2k} P_N(\vec{r})}{[\sum_{\vec{r}} |r|^2 P_N(\vec{r})]^k}. \tag{5.67}$$

We extrapolated the results by performing a fit of the form

$$M_{2k,N} = M_{2k,\infty} + aN^{-\Delta} \tag{5.68}$$

where $M_{2k,\infty}$, a, and Δ are free parameters. Results are reported in Table 5.13. Notice that results for $N = 1600$ and $N = 3200$ are already compatible with each other. Unfortunately, there seems to be a slight systematic underestimation of the values at $N = 3200$ (or an overestimation at $N = 1600$) that is probably causing deviations in the extrapolated asymptotic moments.

N	$M_{4,N}$	$M_{6,N}$	$M_{8,N}$	$M_{10,N}$	$M_{12,N}$
100	1.778(1)	4.422(4)	13.89(2)	52.2(1)	226.8(6)
800	1.815(4)	4.66(1)	15.31(7)	60.8(4)	281(3)
1600	1.819(2)	4.69(1)	15.49(4)	61.8(2)	288(2)
3200	1.818(4)	4.68(2)	15.40(7)	61.2(4)	283(3)
$N \to \infty$	1.821(4)	4.70(3)	15.5(2)	62(1)	290(10)

Table 5.13: The first five non-trivial even moments, with their extrapolated asymptotic values.

5.2.3 Phenomenological expression

Fits against expression (5.31) (with $D_{\rm ph}$ and $f_{\rm ph}$ given by the expressions above) for the two different averaging procedures (5.51) and (5.52), with several values of Λ[1], are reported in Table 5.14. Fitting in a window $\rho_{\rm min} \leq \rho \leq \rho_{\rm max}$ displayed nearly no dependence on the upper cut-off $\rho_{\rm max}$; on the other hand we noticed very high dependence on $\rho_{\rm min}$, meaning that the phenomenological parameters are sensitive almost only to the shape of the distribution function near the origin. Therefore, results were obtained using the whole available range in ρ. There are differences between values obtained from the two different averaging procedures. This is due to the fact that the two regularized distribution functions differ mainly in the small-ρ regime, where the fits are most sensitive. But fixed-width averaging (5.51) turns out to give more self-consistent results (as Λ changes), so we choose this one for our final estimates. Moreover, data for $N = 100$ still displays strong corrections to scaling, as one can see by inspecting Table 5.14 and Figure 5.2, while the other values of N yield results compatible within error bars. Finally, by merging all data with $N \geq N_{\rm min} = 800$ we get

$$\theta_{\rm ph} = \begin{cases} 0.6091(93) & \Lambda = 1/15 \\ 0.6166(83) & \Lambda = 1/50 \end{cases} \tag{5.69}$$

$$\delta_{\rm ph} = \begin{cases} 1.435(27) & \Lambda = 1/15 \\ 1.412(22) & \Lambda = 1/50 \end{cases} \tag{5.70}$$

Values are consistent among different choices of Λ.

One can also fix $\theta_{\rm ph}$ and $\delta_{\rm ph}$ to the theoretical asymptotic values θ and δ, thus obtaining the results in Table 5.15. The same observations hold as for

[1]Values of Λ greater than $1/15$ yield too few data points, while fits for $\Lambda < 1/50$ begin to be quite unstable.

Λ	N	$\theta_{\rm ph}$	$\delta_{\rm ph}$
1/15	100	0.739(20)	1.690(92)
		0.961(25)	2.128(57)
	800	0.616(16)	1.431(46)
		0.594(23)	1.627(72)
	1600	0.609(16)	1.433(45)
		0.560(23)	1.559(84)
	3200	0.603(17)	1.436(49)
		0.518(23)	1.559(84)
1/50	100		
		0.89(28)	1.24(19)
	800	0.645(18)	1.426(48)
		0.679(4)	1.560(12)
	1600	0.602(13)	1.407(34)
		0.675(4)	1.552(12)
	3200	0.601(14)	1.406(35)
		0.676(4)	1.555(12)

Table 5.14: The phenomenological exponents, obtained by fixing the normalization as in Eqs. (5.32) and (5.33). Double entries refer respectively to the two averaging procedures (5.51) and (5.52). Missing entries are due to unstable fits.

the fixed-normalization fits. We obtain

$$D_{\rm ph} = \begin{cases} 0.1913(13) & \Lambda = 1/15 \\ 0.1947(17) & \Lambda = 1/50 \end{cases} \tag{5.71}$$

$$f_{\rm ph} = \begin{cases} 0.07368(26) & \Lambda = 1/15 \\ 0.07341(33) & \Lambda = 1/50 \end{cases} \tag{5.72}$$

These results are not compatible with (5.32) and (5.33) evaluated at $\theta_{\rm ph} = \theta$ and $\delta_{\rm ph} = \delta$ (which give $D_{\rm ph} = 0.17938\ldots$ and $f_{\rm ph} = 0.06931\ldots$), meaning that the asymptotic exponents do not correctly reproduce the region $\rho \approx 1$.

It turns out that much better results for the region of interest can be obtained by letting all 4 parameters ($\theta_{\rm ph}$, $\delta_{\rm ph}$, $D_{\rm ph}$ and $f_{\rm ph}$) run in the fit.

Λ	N	$D_{\rm ph}$	$f_{\rm ph}$
1/15	100	0.159(11)	0.0637(23)
		0.137(16)	0.0573(51)
	800	0.0.1901(25)	0.07333(50)
		0.1613(45)	0.0686(14)
	1600	0.1912(23)	0.07376(46)
		0.1646(33)	0.0700(11)
	3200	0.1923(21)	0.07397(41)
		0.1685(13)	0.07187(43)
1/50	100	0.111(16)	0.0298(22)
		0.2022(81)	0.0646(19)
	800	0.1885(41)	0.07161(80)
		0.1836(16)	0.07029(46)
	1600	0.1978(20)	0.07433(38)
		0.1844(16)	0.07053(46)
	3200	0.1979(20)	0.07434(38)
		0.1841(16)	0.07045(46)

Table 5.15: The phenomenological constants, obtained by fixing the exponents in (5.31) to their asymptotic values. Double entries refer respectively to the two averaging procedures (5.51) and (5.52).

We obtain

$$\theta_{\rm ph} = 0.2765(82) \tag{5.73}$$
$$\delta_{\rm ph} = 1.947(31) \tag{5.74}$$
$$D_{\rm ph} = 0.285(11) \tag{5.75}$$
$$f_{\rm ph} = 0.08046(96) \tag{5.76}$$

(with $\Lambda = 1/15$, $N_{\rm min} = 800$, and using all the available range in ρ). With this choice one loses proper normalization in favor of a tighter accordance with data in the region where the EEDF is higher.

A comparative plot of the EEDF and its phenomenological approximants is displayed in Figure 5.4.

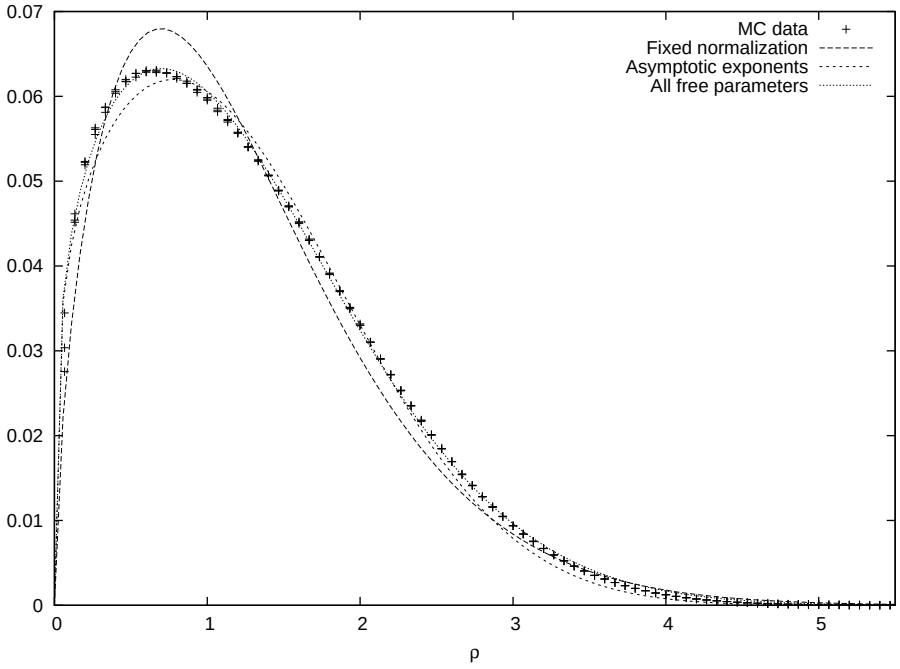

Figure 5.4: The EEDF against several phenomenological approximants.

5.2.4 Internal points distribution function

We have computed P_N^{ENN} at the θ point[1] and fitted the results with $a+b/N^{\Delta}$ (see Table 5.16).

The estimate for the exponent is

$$\theta_{\mathrm{int}} = 0.407(11), \tag{5.77}$$

which is in good agreement with the theoretical value $0.4166\ldots$ For the probability in the scaling limit, we find

$$P_{\infty}^{\mathrm{ENN}} = 0.7854(14). \tag{5.78}$$

5.2.5 Gyration tensor

Numerical results are reported in Table 5.17, while a graph of the scaling functions F_α is reported in Figure 5.5.

[1] We have also studied P_N^{ENN} for noninteracting SAWs in two and three dimensions. In both cases the data are well fitted by $a + b/N$, that allows us to conclude that $\theta_{\mathrm{int}} > 1$. Note that in three dimensions we do not observe corrections of order $N^{-\Delta}$, $\Delta \approx 0.5$, that are naively expected.

N	P_N^{ENN}
100	0.63307(4)
800	0.71579(10)
1600	0.73159(6)
3200	0.74407(10)
$N \to \infty$	0.7854(14) $\theta_{\mathrm{int}} = 0.407(11)$

Table 5.16: Probability that the endpoint is a nearest neighbor of the walk, with its extrapolated asymptotic value and exponent.

N	q_1	q_2	$\mathcal{A}$
100	35.5431(77)	7.89542(82)	0.376682(82)
800	386.85(30)	85.871(34)	0.37569(28)
1600	859.93(37)	190.262(41)	0.37653(16)
3200	1916.6(1.5)	422.06(17)	0.37805(28)

Table 5.17: Observables related to the gyration tensor: the two eigenvalues and the asphericity.

Fitting the eigenvalues as functions of N against scaling form (5.40) yields

$$\nu = \begin{cases} 0.5747(3) & \text{from } q_1 \\ 0.5739(1) & \text{from } q_2 \end{cases} \tag{5.79}$$

which agree with the slightly off-critical values obtained through the analysis of the radii in Section 5.2.1. Notice that the walk is quite strongly elliptical, with the major axis being a factor of three longer than the minor one.

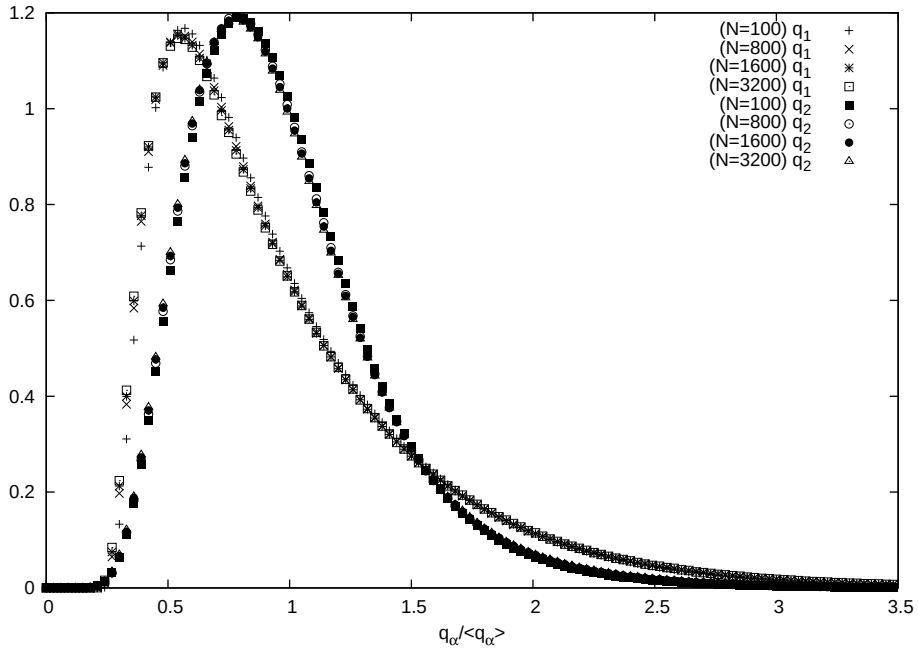

Figure 5.5: The renormalized distribution functions for the two eigenvalues of the gyration tensor.

Chapter 6

SLE and walks

In this chapter we put everything together. We compare the end-to-end distribution function obtained by whole-plane SLE stopped at the random time when its fractal variation reaches a fixed value and the distribution of an inner point in the self-avoiding walk and in the critical (θ-point) interacting self-avoiding walk. The main result is numerical evidence in favor of a conjecture by Loewner, Schramm and Werner [35] about the scaling limit of whole-plane self-avoiding walks. Much of the material in this chapter will appear in [80].

6.1 Details of the analysis

Before one can actually try and match two distribution functions, some details must be checked. First of all, the SLE simulation depends on many parameters (namely, the number of samples produced, the length used in computing the fractal variation, the total variation, the mean length of each step), and one has to check that the correct scaling regime is attained. Secondly, the distribution function for inner points in the walk models depends on the ratio M/N, as in Equation (5.34), and since SLE is supposed to reproduce the distribution of a finite section inside an infinite walk one should let $M/N \to 0$; this requires another check to see if the necessarily finite values of N and M lie deep enough in the scaling limit.

Recall from Chapters 3 and 4 what parameters play a role in the simulations:

- κ: the diffusivity of the Brownian motion that drives the Loewner evolution.
- N: the number of independent samples generated; it corresponds to

the total number of iterations, since we use exact sampling.

- λ: the length parameter used to measure the fractal variation of the curve; the variation is $\mathrm{fvar}_\lambda(\gamma) = n\lambda$, where n is the number of segments of length λ needed to cover the entire curve γ.

- Υ: the total variation of the curve, which defines the stopping time τ_Υ.

- Λ: the radius of the forbidden circle around the origin; the trace starts at $z = 1$ and travels towards ∞ avoiding this region.

- l: the inherent characteristic length of the discretization steps: since we let Δ_k scale with k in such a way as to have approximate constant behaviour in the step length, this corresponds to the mean distance between consecutive points along the SLE trace.

Of course, not all parameters are independent, since for instance a shrinking of Λ corresponds to a swelling of l, for a scale invariant system as the one we are simulating (one can map each configuration in the two scenarios by a rescaling).

In the scaling limit[1], we want to have

$$\begin{aligned} l &\to 0 \\ \Lambda &\to 0 \\ \lambda &\to 0 \\ \mathrm{fvar}_\lambda(\gamma) &= \Upsilon \end{aligned} \tag{6.1}$$

In words, one wants to let the size of the steps go to zero, to remove the cutoff induced by the presence of a forbidden region around the origin, to measure the fractal variation with a finer and finer mesh, and to have the number of steps go to infinity. The latter requirement is actually implied by the last line of Equation (6.1). In fact, keeping a finite value of the total variation when it is measured at scale $\lambda \to 0$ means covering the curve with a number of segments $n \to \infty$. We will also ask that the fractal variation be measured at a scale large enough with respect to the granularity of the trace, because actually each single portion of the trace that is covered by one segment of length λ should be large enough to have the same fractal properties of the whole curve. In the end what this means is, that we have to let both l and λ go to 0, but in such a way that $1/l \gg 1/\lambda$.

[1] We are not claiming to have a precise statement of convergence for the fractal variation. The reasoning in this section is purely heuristic.

Operatively, what we will do is the following. We will fix l to some small value and will measure everything else (but Λ) in units of l. We will compute the fractal variation using several values for λ and try to recognize the regime where it is small enough to be far into the scaling limit, but not too small to be comparable with the step-size of the discretization. Then, instead of letting $\Lambda \to 0$, we will keep it fixed to $\Lambda = 1$ (this is very convenient because of the nature of the simulations) and let $\Upsilon \to \infty$. Again, what this means operatively is that we will perform the simulations for increasings values of Υ and check whether we are already in the scaling regime or there remain corrections to scaling.

For both $\kappa = 6$ and $\kappa = 8/3$ we are going to perform these checks before actually matching the distribution against the lattice models. As we discussed in Chapter 5, the universal scaling behaviour of the distribution function of the M-th point in an N-step walk ω_i, $i = 0, \ldots, N$ (both the SAW and the ISAW) in the limit $N \to \infty$ and $\mathbf{r} \to \infty$ is

$$P_{N,M}(\mathbf{r}) \sim \frac{1}{\xi_M^2} \, f_W(\rho, \frac{M}{N}) \tag{6.2}$$

where $\rho = |\mathbf{r}/\xi_N|$ and $\xi_M^2 = \langle(\omega_M - \omega_0)^2\rangle_\omega$ is the correlation length after M steps. The subscript in f_W stands for "Walk", and of course the mean $\langle\cdot\rangle_\omega$ is on the walk ensemble. Again, we will have to perform some smoothing operation on the raw lattice data, as in (5.51) and (5.52), since wild lattice artifacts would otherwise cover the true behaviour. This is not necessary (and we shall not do it) when computing observables of the distribution, such as the moments.

We define the corresponding quantities also for the SLE approximated trace $\gamma(t_k)$, $k = 0, \ldots, \mathcal{N}$, where $\mathcal{N}$ is the number of points computed on the trace up to the stopping time τ_Υ (not counting the starting point). Consider the probability density $P(z)$ that the point $\gamma(t_\mathcal{N})$ is z, then we will suppose it has the following scaling behaviour in the scaling limit defined above:

$$P_\Upsilon(z) \sim \frac{1}{\xi_\Upsilon^2} \, f_S(\rho) \tag{6.3}$$

where $\rho = |z/\xi_\Upsilon|$, and

$$\xi_\Upsilon^2 = \left\langle |\gamma(t_\Upsilon)|^2 \right\rangle_{\text{SLE}} \tag{6.4}$$

and the mean $\langle\cdot\rangle_{\text{SLE}}$ is over all realizations of the Brownian driving function. We will use here the same smoothing procedure as before (it is needed in this case as well, even though the end-point lives in the continuum). Of course, the lattice is replaced by the complex plane, and the denominator in (5.51),

which represents the number of lattice points in each shell, will get replaced by the volume of each shell:

$$P_{\Upsilon}^{\mathrm{av}}(\Sigma_j) = \frac{1}{V(\Sigma_j)} \int_{\Sigma_j} P_{\Upsilon}(z) dz \tag{6.5}$$

where Σ_j is the shell[1] $(j-1)\Delta < |z| < j\Delta$, $j = 1, 2, \ldots$, and its volume is $V(\Sigma_j) = \pi(2j-1)\Delta^2$. We shall not explicitly study the behaviour of equation (6.5) as Δ is changed — as we did in in Chapter 5 —, because many more important sources of systematic error are present in this case.

The foregoing relations define the two renormalized distribution functions f_W and f_S that we plan to try and match between SLE and the lattice models. More precisely, we will compare $f_S(\rho)$ and $f_W(\rho, M/N \to 0)$ — which from now on we shall denote simply $f_W(\rho)$ —, so as to avoid boundary effects in the lattice walk models, and will check whether

$$f_W(\rho) = f_S(\rho). \tag{6.6}$$

Implicit in the forthcoming analysis is the assumption that the distribution function for the stopped SLE trace behaves as in (6.3), which we are going to verify *a posteriori* on a case-by-case basis.

In order to compare quantitatively the distributions, we will focus on their moments

$$M_{2k} = \frac{\int_0^\infty \rho^{2k+1} f(\rho)\, d\rho}{(2\pi)^{k-1} \left[\int_0^\infty \rho^3 f(\rho)\, d\rho\right]^k}, \tag{6.7}$$

where $f(\rho)$ can be either $f_W(\rho)$ or $f_S(\rho)$. In practice, we will not use this definition. For simplicity, we will be computing M_{2k} directly from the end-point data obtained from the simulation. Moreover, it is convenient to introduce an ultra-violet and an infra-red cutoff — that is, a window for computing the moments — since deviations from scaling behaviour are more pronounced in the large and small ρ regimes. Suppose we have N independent samples of $\gamma(t_{\mathcal{N}})$, and call them z_i, $i = 0, \ldots, N-1$. We will compute the following quantities

$$M_{2k}(\rho_{\min}, \rho_{\max}) = \frac{\sum' |z_i|^{2k}}{\left[\sum' |z_i|^2\right]^k}, \tag{6.8}$$

where the sums $\sum'$ are restricted to the window

$$\rho_{\min} < \frac{|z_i|}{\xi_{\Upsilon}} < \rho_{\max}, \tag{6.9}$$

[1]Notice that Δ here has nothing to do with the Δ_k defined elsewhere.

and we shall study how well the moments compare for the two distributions f_W and f_S as a function of the cut-offs $\rho_{\min}$ and $\rho_{\max}$. Notice that the moments in (6.8) strongly depend on the cut-offs, especially the higher-order ones.

6.2 Fractal dimensions

In this section we do some preliminary checks to be sure that the process we are simulating has the expected properties. First, we check that it has the scaling property (6.3), by making sure that — modulo slight corrections to scaling — the renormalized distribution functions obtained with different values of λ and Υ all collapse onto the same universal curve.

In Figure 6.1 are plotted the distribution functions of whole-plane SLE with $\kappa = 8/3$ for $\lambda = 4, 10, 20, 40$ with $\Upsilon = 400$. Recall that we measure everything in units of l. As is clear from the plots, the distributions nicely fall on the same curve, apart from slight deviations in the extreme regimes (ρ large and ρ small) where corrections due to scaling and to the finiteness of λ are more important (these are more apparent in the logarithmic plot). What is clear from the plots is that the curve with $\lambda = 40$ suffers from severe deviations due to the coarse grained nature of the procedure used for computing the fractal variation. On the other hand, any other value $\lambda < 40$ seems to yield distributions falling more or less on the same curve. Actually, a systematic drift in λ is present also for smaller values, this time in the regime where $\rho \approx 1$. It becomes visible if one carefully computes the moments of the distributions in a window discarding the tails at ρ large and small. By inspection of Table 6.3, where this behavior is apparent, we then choose the value $\lambda = 20$, which seems a good compromise, and simulate SLE for a larger value of the total fractal variation, namely $\Upsilon = 800$. Results are reported in the same table, and a comparative plot of two distributions obtained with different values of Υ and the same λ is in Figure 6.2.

The same check is done for $\kappa = 6$: results are in Figure 6.3. We have less data than in the $\kappa = 8/3$ case; here $\lambda = 4, 10, 20$ and $\Upsilon = 400$. Statistical errors are slightly larger as well.

Next, we measure the fractal dimension d_f of the SLE traces. For this purpose, we revert to parametrization by capacity, since the fractal dimension is not a parametrization-dependent observable, and of course simulating SLE with its natural proper time is way faster. We produce the SLE trace approximant $\gamma(t_k)$, $k = 0, \ldots, \mathcal{N}$ and then apply the same technique we introduced in Chapter 4 for computing the fractal variation of a growing chain. For increasing values of λ we measure the number $n(\lambda)$ of segments of length

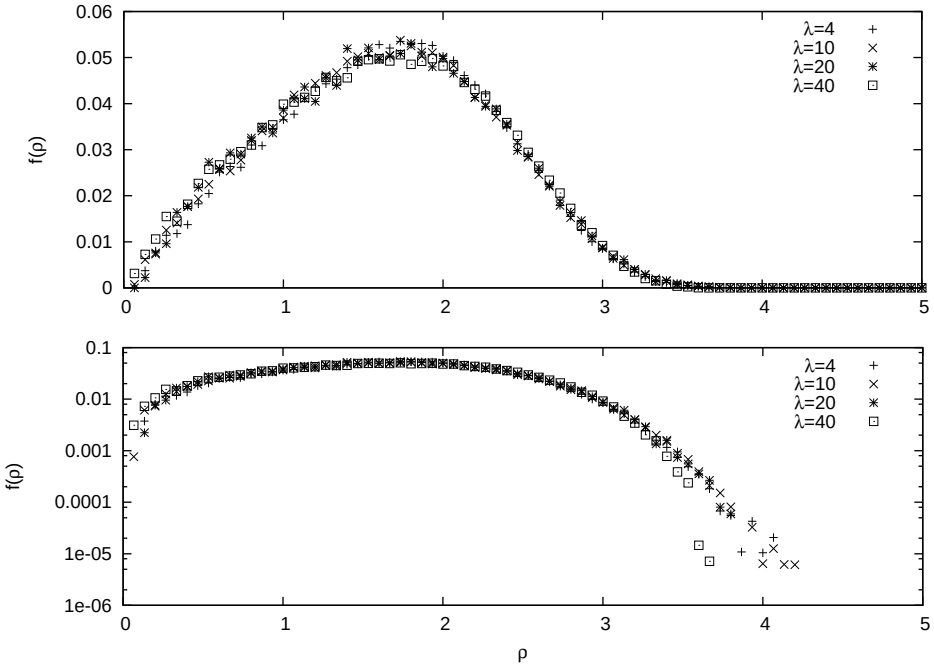

Figure 6.1: The renormalized distribution functions for whole-plane SLE $\kappa = 8/3$ with fixed total fractal variation $\Upsilon = 400$. The plot on the bottom has logarithmic scale on the y axis.

λ that are needed to cover up the entire γ. The expected scaling form as $\lambda \to 0$ is

$$n(\lambda) \sim \lambda^{-d_f} \tag{6.10}$$

We recall from Chapter 2 that the fractal dimension of SLE is $d_f(\kappa) = 1+\kappa/8$. The results for $\kappa = 8/3$ and $\kappa = 6$ are reported in Figure 6.4 in a log-log plot, and compared against the two lines corresponding to fractal dimensions $4/3$ and $7/4$. Notice the expected strong deviations from the scaling form (6.10) at small values of λ. These deviations are due to the fact that at small scales (comparable to the step-size l) the curve is of course non-fractal; moreover, for very small λ a saturation effect occurs, because $n(\lambda)$ can not exceed the actual number of steps in γ. Small deviations are expected to appear also at large λ, when λ is comparable to the end-to-end radius of the trace itself.

Results for fits in a window $\lambda_{\min} < \lambda < \lambda_{\max}$ are reported in Table 6.2. We kept $\lambda_{\max}$ fixed to the largest possible value just before the saturated region (which occurs quite abruptly), while changing $\lambda_{\min}$. Errors naturally become larger and larger as $\lambda_{\min}$ is increased, but nonetheless the trend shows that the fractal dimensions converge to the expected values.

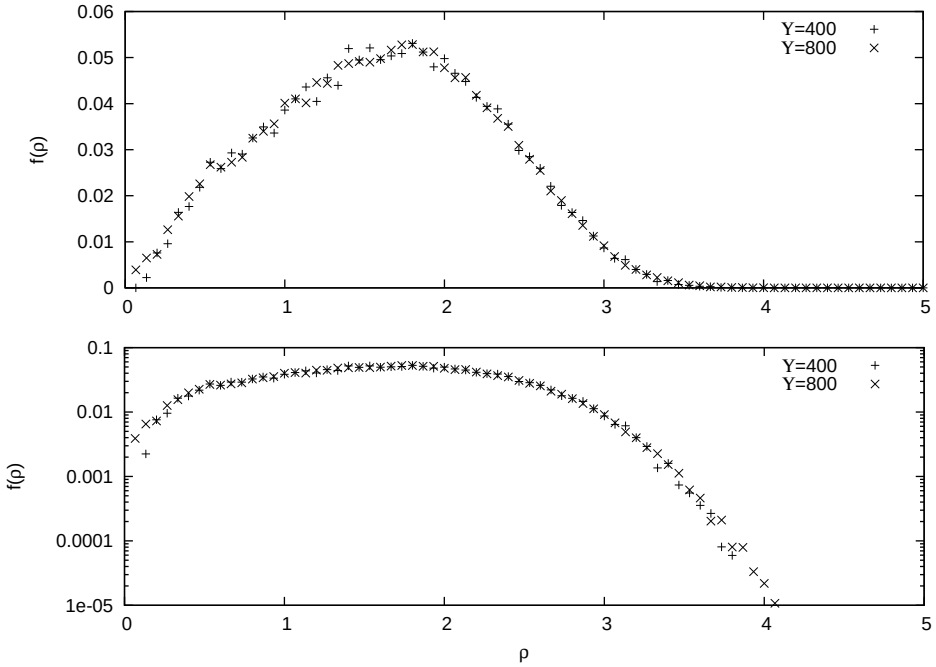

Figure 6.2: The renormalized distribution functions for whole-plane SLE $\kappa = 8/3$ stopped at fractal variation $\Upsilon = 400$ and 800. Here $\lambda = 20$.

6.3 $\kappa = 8/3$ and SAW

Correspondence between the distribution functions for the self-avoiding walk restricted to stay in the upper half plane and chordal SLE with $\kappa = 8/3$ has been tested numerically in [51], yielding a positive answer. We shall not repeat this test here, but we shall rather move on directly to the whole-plane case.

Before comparing the distribution functions obtained from whole-plane SLE and the self-avoiding walk, we study the behaviour of $f_W(\rho, M/N)$ as a function of M/N, since we want to look at f_W in the regime where the parameter goes to zero. Figure 6.5 shows plots of the internal point renormalized distribution function for $M = 1000, 2000, 4000, 8000, 16000, 32000$ and $N = 100000$. The curves all fall onto the same universal distribution. Table 6.3 displays the computed moments for these distributions. One can see that the dependence on M/N is very slight, if present at all. Only the moments for the extreme values $M = 1000$ and $M = 32000$ seem to be very slightly out of the regime. In the former case, this is probably due to lattice fluctuations, while in the latter one probably begins to see the corrections that will eventually sum up to give the usual end-point distribution function

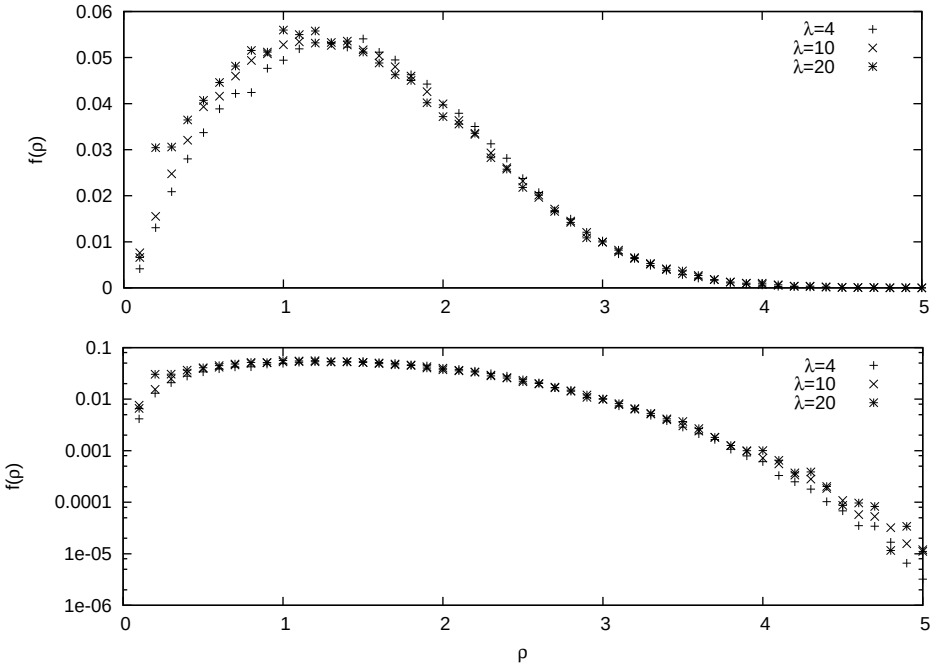

Figure 6.3: The renormalized distribution functions for whole-plane SLE $\kappa = 6$ with fixed total fractal variation $\Upsilon = 400$.

as $M \to N$.

We choose to pick the distribution at $M = 8000$ for the comparison with SLE data. The choice is not at all crucial, since — as will be clear in the following — errors in SLE data are much higher than the "distance" between the SAW distributions for different inner points. Table 6.3 gathers values of the moments evaluated for the self-avoiding walk and for the whole-plane SLE for several values of the cut-offs $\rho_{\min}$ and $\rho_{\max}$ and of the parameter λ, with fixed $\Upsilon = 400$ and $\Upsilon = 800$. Let us take a closer look at the table. Of course, accordance for low-order moments is more easily established, while inspection of high-order ones helps in recognizing trends. Notably, systematic errors are huge. They are due to the scaling behavior in λ and Υ. Moreover, they are wilder for larger windows, since — as we already noted — corrections in the extreme regimes are more important. Also, for the same reason they appear to be more prominent for $\rho \in [0.5, 3.5]$ than for $\rho \in [0, 3]$. Let us then consider only the window $\rho_{\min} = 0$, $\rho_{\max} = 3$. As we noted in Section 6.2, if we fix $\Upsilon = 400$ the moments display a maximum corresponding to $\lambda = 20$, which then seems to be the best compromise. Moreover, if one then fixes $\lambda = 20$ and looks at the scaling in the total fractal variation, one can see that the moments actually keep increasing as Υ is doubled and tend to the

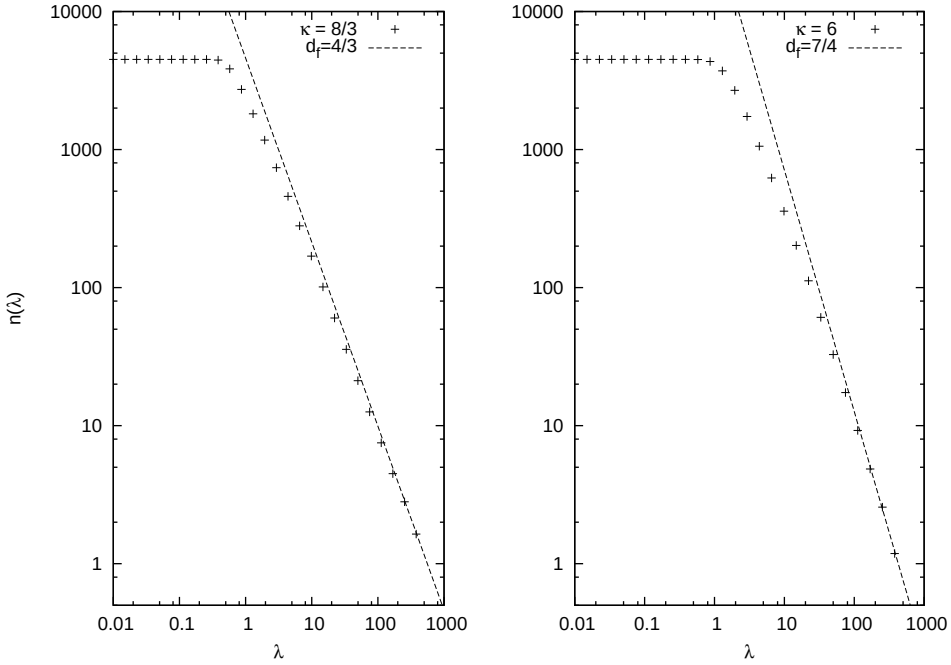

Figure 6.4: Number of segments of length λ needed to cover the trace. Notice the logarithmic scale on both axes. The lines represent the theoretical slope corresponding to fractal dimension $1 + \kappa/8$. (Errors are too small to be displayed in these plots.)

SAW values.

A comparative plot of the distribution functions of SLE and SAW is in Figure 6.6.

6.4 $\kappa = 6$ and ISAW

Correspondence between SLE with $\kappa = 6$ and the critical (θ-point) interacting self-avoiding walks in the half-plane is easily established. The argument by Coniglio et al. described in Chapter 1 connects the critical ISAW to the interfaces of critical percolation. The correspondence of the latter with SLE has been rigorously proved for the triangular lattice [42], and universality suggests that it holds also for the square lattice. Finally, Kennedy has compared the distribution functions for SLE with $\kappa = 6$ and the critical percolation explorer in [51], finding good agreement.

Here, we consider the whole plane. As we did for the self-avoiding walk in Section 6.3 we first compare the distributions of the internal points. The

κ	$\lambda_{\min}$	d_f	$1 + \kappa/8$
$\frac{8}{3}$	1	1.14(1)	$\frac{4}{3} = 1.33\ldots$
	3	1.241(6)	
	10	1.283(2)	
	30	1.284(5)	
	100	1.29(4)	
6	1	1.06(4)	$\frac{7}{4} = 1.75$
	3	1.36(1)	
	10	1.37(4)	
	30	1.40(7)	
	100	1.61(4)	

Table 6.1: The fractal dimension of whole-plane SLE for $\kappa = 8/3$ and $\kappa = 6$, measured in shrinking windows.

M	M_4	M_6	M_8	M_{10}	M_{12}
1000	1.3821(23)	2.3206(60)	4.477(16)	9.623(46)	22.59(14)
2000	1.3828(23)	2.3243(60)	4.493(16)	9.682(47)	22.81(14)
4000	1.3826(23)	2.3232(60)	4.489(16)	9.677(47)	22.83(15)
8000	1.3822(23)	2.3214(60)	4.482(16)	9.645(46)	22.69(14)
16000	1.3812(23)	2.3179(60)	4.472(16)	9.613(46)	22.58(14)
32000	1.3787(23)	2.3071(59)	4.436(16)	9.504(45)	22.26(14)

Table 6.2: The first 5 non-trivial moments of the self-avoiding walk renormalized distribution function for several internal points. Here, the total walk length is $N = 100000$.

distributions of two internal points ($M = 500, 2000$ out of walks of length $N = 3000$) together with the distribution of the endpoint are plotted in Figure 6.7.

The plot in Figure 6.8 shows the distribution functions for whole-plane SLE with $\kappa = 6$ and the interacting self-avoiding walk at the transition point. It is obvious that there is no coincidence at all.

We want to make sure that the discrepancy is not caused by a scaling in λ or Υ, and neither by a failure of the fractal variation method due to the compactness of the trace at $\kappa = 6$. Therefore, we compare the distributions obtained by this method with those obtained with the reparametrization

λ	$\rho_{\min}$	$\rho_{\max}$	M_4	M_6	M_8	M_{10}	M_{12}
4	0	3	1.304(10)	1.970(18)	3.267(38)	5.787(84)	10.74(18)
		3.5	1.337(10)	2.127(21)	3.817(50)	7.49(13)	15.77(32)
		∞	1.342(10)	2.155(22)	3.933(55)	7.94(15)	17.39(42)
	0.5	3	1.291(10)	1.928(17)	3.164(37)	5.543(79)	10.18(17)
		3.5	1.324(10)	2.084(20)	3.700(49)	7.19(12)	14.97(31)
10	0	3	1.315(7)	2.009(14)	3.374(32)	6.045(70)	11.35(16)
		3.5	1.352(10)	2.182(17)	3.979(42)	7.93(11)	16.94(27)
		∞	1.357(7)	2.216(18)	4.120(46)	8.47(12)	18.92(36)
	0.5	3	1.300(6)	1.962(14)	3.254(30)	5.760(65)	10.68(14)
		3.5	1.337(7)	2.132(17)	3.841(40)	7.57(10)	15.97(26)
20	0	3	1.320(11)	2.022(25)	3.404(55)	6.11(12)	11.48(27)
		3.5	1.355(12)	2.188(29)	3.983(71)	7.91(18)	16.79(46)
		∞	1.359(12)	2.212(30)	4.078(75)	8.27(20)	18.06(54)
	0.5	3	1.303(11)	1.971(24)	3.274(52)	5.80(11)	10.75(25)
		3.5	1.338(12)	2.134(28)	3.835(68)	7.52(17)	15.76(43)
40	0	3	1.318(7)	2.008(14)	3.352(31)	5.955(68)	11.07(15)
		3.5	1.344(7)	2.133(16)	3.784(39)	7.282(94)	14.92(23)
		∞	1.345(7)	2.135(16)	3.792(39)	7.311(95)	15.02(24)
	0.5	3	1.300(6)	1.954(14)	3.217(30)	5.636(64)	10.33(14)
		3.5	1.327(7)	2.077(16)	3.635(37)	6.901(88)	13.95(22)
20	0	3	1.322(9)	2.030(20)	3.428(42)	6.177(93)	11.66(21)
		3.5	1.359(9)	2.207(23)	4.048(56)	8.12(14)	17.43(37)
		∞	1.366(10)	2.247(24)	4.218(62)	8.77(17)	19.81(49)
	0.5	3	1.304(8)	1.975(18)	3.290(40)	5.845(87)	10.88(19)
		3.5	1.341(9)	2.149(22)	3.889(53)	7.69(13)	16.30(34)
SAW	0	3	1.330(2)	2.059(5)	3.508(10)	6.379(23)	12.155(52)
		3.5	1.371(2)	2.258(6)	4.211(14)	8.592(36)	18.763(94)
		∞	1.382(2)	2.321(6)	4.482(16)	9.645(47)	22.69(15)
	0.5	3	1.312(2)	2.003(5)	3.365(10)	6.034(21)	11.336(48)
		3.5	1.353(2)	2.199(5)	4.045(13)	8.141(33)	17.539(87)

Table 6.3: The moments for whole-plane SLE with $\kappa = 8/3$, computed in several windows and for several values of λ. Values in the uppermost table have $\Upsilon = 400$ while those in the middle table have $\Upsilon = 800$. They are to be compared with the values listed immediately below, which are those measured in the same windows for the SAW with $N = 100000$, $M = 8000$.

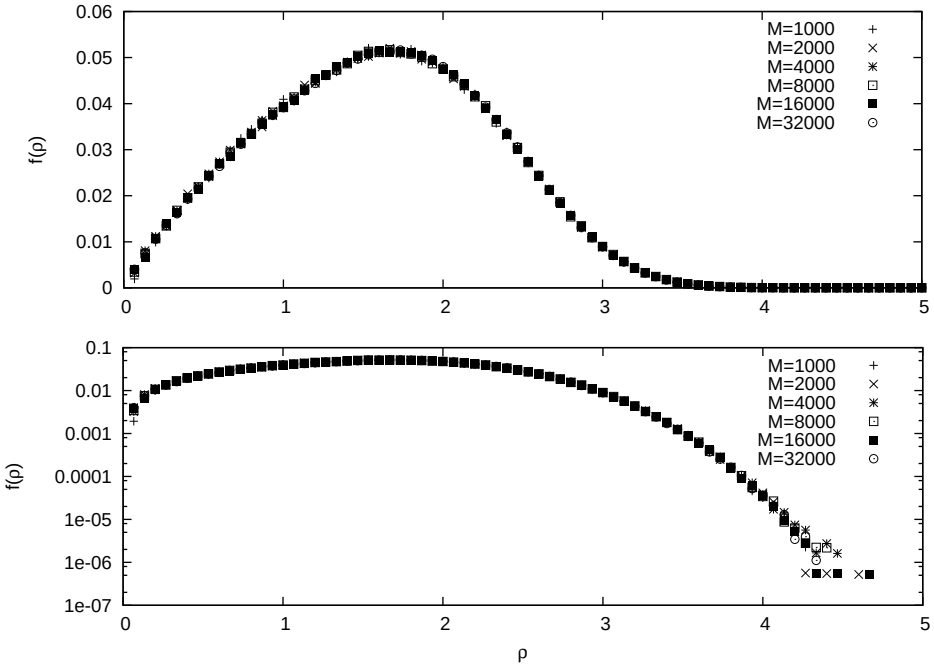

Figure 6.5: The self-avoiding walk renormalized distribution functions for several internal points ($N = 100000$).

based on the second-derivative of the map, which we proposed and studied in Chapter 4. The results for both $\kappa = 8/3$ and $\kappa = 6$ are in Figure 6.9, and support the fact that the SLE traces we are producing have the correct parametrization.

This result is puzzling. Naively one would expect that just as whole-plane SLE with $\kappa = 8/3$ turns out to yield the correct distribution function of the self-avoiding walk, so should happen for $\kappa = 6$ and the θ-point. As to why this is not so, one can make suppositions. One possibility is that the correspondence between SLE and the walk model extends to the whole plane for the self-avoiding walk thanks to some special feature the latter possesses. One such feature for instance could be restriction covariance [35], that the θ-point indeed does not possess. It is by restriction covariance that the SAW in the half plane is just the SAW in the whole plane restricted not to leave $\mathbb{H}$. On the other hand, the *interacting* SAW behaves in a very different way under a change of the domain: in defining the ISAW in the half plane one faces some ambiguity with the boundary conditions. Should the real axis be attractive as the walk itself, or should it simply be the boundary of a forbidden region?

Another possibility is that the θ-point is not in the same universality class

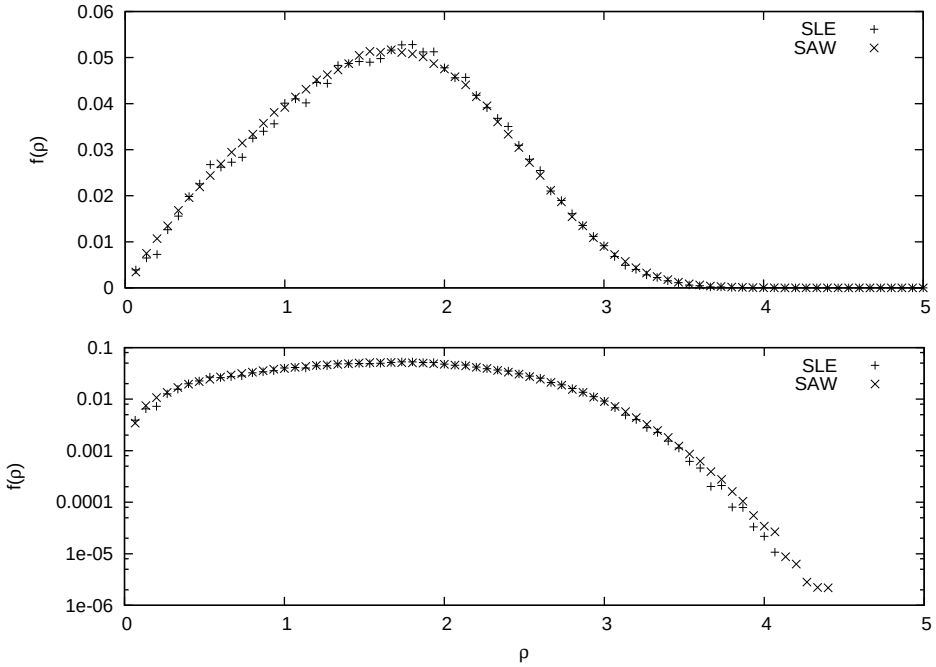

Figure 6.6: A comparative plot of the distribution functions obtained from whole-plane SLE and SAW.

as the percolation explorer, even in the half plane. Actually, the argument by Coniglio et al. uses Ockham's razor to guess that the attractive interaction introduced by the plaquettes that have already been visited drives the model towards the *tri*-critical point. Nothing really ensures that it is not a transition of higher order criticality. Moreover, the structure of the operators emerging in the scaling limit is unknown, and there could be exactly marginal perturbations that could change some properties of the distribution function without affecting the critical exponents. To check numerically if this is the case, one should first of all define what the ISAW is in the half plane. If one wants a chance of obtaining the scaling limit of the percolation explorer, an *attractive* real boundary should probably be chosen. This is because the percolation explorer is defined by fixing the spins of the boundary plaquettes, which means that the walk has a fixed choice when it hits the boundary, and this counts as an attractive interaction in the partition function. Moreover, heuristics tell us that since SLE satisfies conformal Markov covariance, then the walk model should probably treat the boundary in the same way as the support of the walk itself. Notice that simulating such a half-plane version of the ISAW would require devising new algorithms (or relying on PERM [79]), since the Monte Carlo moves we used for our simulations intrinsically need

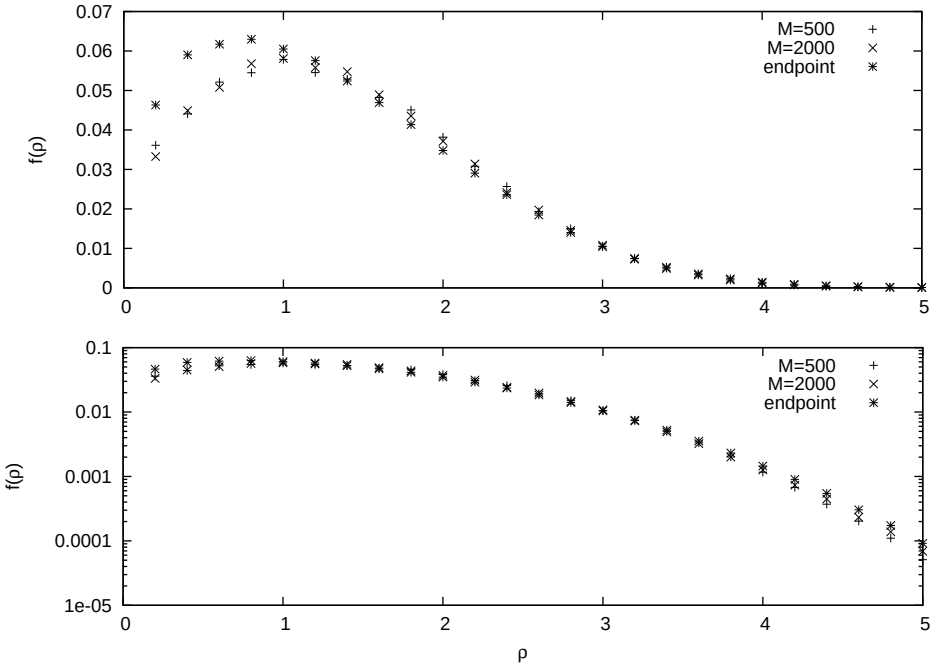

Figure 6.7: The θ-point renormalized distribution functions for two internal points and the endpoint ($N = 3000$).

the full plane. In addition, the critical point of such a model is not expected to be at the same temperature as in the whole-plane version, so one should also carefully look for it before a match with SLE and/or percolation can be done.

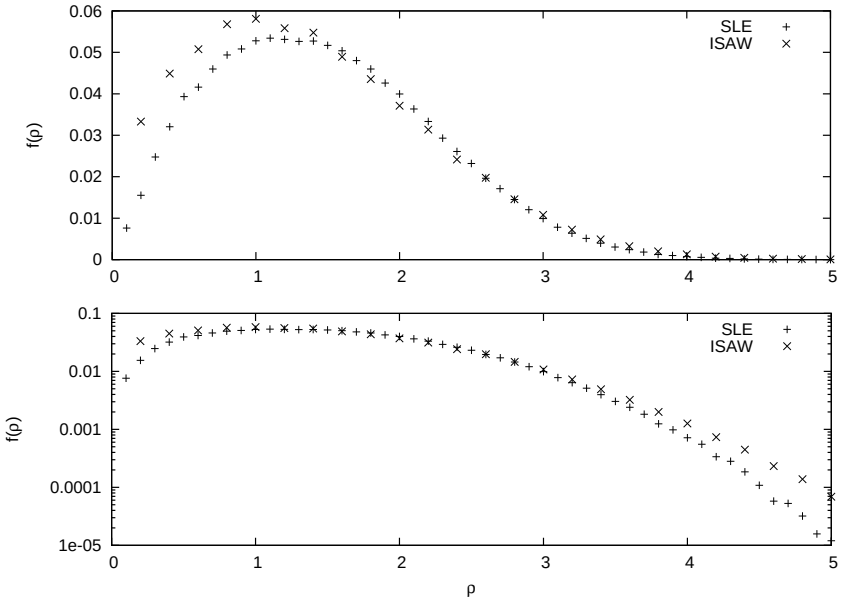

Figure 6.8: A comparative plot of the distribution functions obtained from whole-plane SLE and critical ISAW.

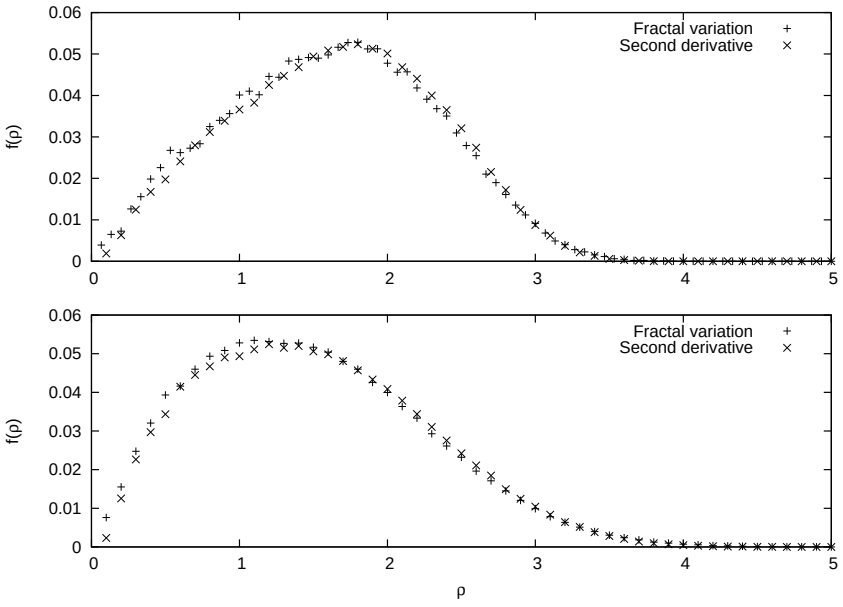

Figure 6.9: A comparative plot of the distribution functions obtained for SLE with $\kappa = 8/3$ (above) and $\kappa = 6$ (below) with two different methods of reparametrizing the trace.

Conclusions and outlook

This work was devoted to the study of the critical properties of interacting walks in two dimensions, with particular emphasis on their conformal invariance.

Two models have been considered, which belong to different universality classes. The first is the well-known self-avoiding walk, which models polymers in good solutions. The second is the interacting self-avoiding walk, in which nearest-neighbor contacts between non-consecutive monomers are energetically favored. As the strength of this interaction is varied a (tri-)critical point is reached, called the θ point. This model describes polymers in poor solutions (under the critical temperature) and the critical transition between the latter and the swelled SAW-like behavior above the critical temperature.

We first focused on the critical properties at the θ point, checking them against the theoretical predictions. We performed extensive Montecarlo simulations and obtained high precision estimates for the critical exponents and the critical temperature, as well as for several quantities such as the universal ratios and the CSCPS expression. The end-to-end distribution function has been studied thoroughly (both the short- and large-distance behaviors, and the phenomenological expression).

Then we moved on to considering conformal-invariance related questions. The recently-introduced and widely studied Schramm-Loewner evolutions (SLE) are the perfect candidates for the scaling limits of conformally invariant walk models. SLE is a one-parameter family ($\kappa > 0$) of random processes on the complex plane. Connection to the self-avoiding walk ($\kappa = 8/3$) and to the θ-point interacting self-avoiding walk ($\kappa = 6$) has been established in the literature only in the half plane (the latter relies on the supposed equivalence with the critical percolation explorer). We checked this connection in the topologically different whole-plane case, focusing in particular on the distribution functions. To this aim, we devised a way to simulate SLE in $\mathbb{C}$ and introduced and studied some techniques to obtain the correct parametrization. We found that the distribution function of an inner point in the self-avoiding walk actually coincides with the end-point distribution function

of whole-plane $\kappa = 8/3$ SLE with the correct parametrization, thus providing numerical evidence in favor of a conjecture by Werner. We did the same check for the θ-point polymers and $\kappa = 6$ whole-plane SLE, and surprisingly found that the two distribution functions do not match. This unexpected result deserves further investigation, since it could unveil new aspects of the conformal invariance of θ-point self-avoiding walks, and shed new light on the connection with critical percolation.

The present results and methods could be extended and developed in several directions. First of all, the conformal invariance of θ-point polymers has to be investigated further. Of course, one expects the critical point to display conformal invariance. The failure of the connection to whole-plane SLE could be due for instance to the critical interacting SAW not satisfying the domain Markov property, and this property could be checked directly. One could also go the other way around, and analyze the statistical properties of the driving function of ISAWs by embedding the lattice in $\mathbb{C}$ and then taking the continuum limit. One way to do this is the so-called *zipper algorithm*, which exploits some of the techniques we described in Chapter 3 to obtain the approximate driving function given the trace.

Another numerical investigation could be done, using this same method. Lately, several researchers turn their attention to the study of off-critical (massive) scaling limits of walks and interfaces using Loewner methods []. The zipper algorithm can be used for such a purpose, for studying the critical crossover limit to and from the several polymeric universality classes. For instance the Domb-Joyce model (random walks with energy proportional to the number of intersections) and the ISAW offer the possibility of such an investigation.

Higher-order multicritical points could be studied, as well. Polymers at higher order criticality all have a trivial central charge (this is essentially because they all map to a $O(N \to 0)$ field theory). But since the mapping SLE$\leftrightarrow$CFT expressed by Equation (2.37) is quadratic, at most two values of κ can be found for a given central charge, namely our old friends $\kappa = 8/3$ and $\kappa = 6$. An immediate consequence is then that multicritical polymers either are not conformally invariant or they do not satisfy the domain Markov property. Necessarily, their driving function is not rescaled Brownian motion.

Now, turning attention to SLE itself, it would be interesting to study its reparametrization issues more deeply. Firstly, at present we do not know

how to obtain the distribution function of the *end-point* of a *finite-length* walk (in the scaling limit) from SLE. This could be related to the problem of the Schramm-Loewner description of the critical crossover. Secondly, the techniques studied in Chapter 4 should be developed more (for instance by mixing the first- and second-derivative approaches in order to obtain a better approximation), since they are very useful in matching conformational properties of SLE and the walk models. The fractal-variation method is good for obtaining the distribution of a single point, but it gets slower and slower when one is interested in computing more and more points on the trace with the correct parametrization.

Appendix A

Slit mapping of the disc

In this appendix we give a derivation of the radial map $\phi^{\mathbb{D}}(z)$ that produces a slit of logarithmic capacity Δ inside the unit disc, Equation (3.19). The whole-plane map that produces a slit out of the disc can then be computed as in (3.18). As we discussed in Chapter 3, $\phi^{\mathbb{D}}(z)$ can be found by solving the radial Loewner equation in the disc with constant driving force, and then taking the inverse. In particular, we want the slit to be based at the real point 1, so the driving term will be taken equal to

$$e^{iU_0} = 1. \tag{A.1}$$

The Loewner equation takes the form

$$\dot{g}_t(z) = -g_t(z)\frac{g_t(z)+1}{g_t(z)-1}, \quad g_0(z) = z, \tag{A.2}$$

which gives the map that absorbs the slit as a function of time. The atomic map that instead *produces* the slit of capacity Δ will then be

$$\phi^{\mathbb{D}}(z) = g^{-1}_{t=\Delta}(z). \tag{A.3}$$

From Equation (A.2), by separation of variables, one obtains

$$\frac{g_t - 1}{g_t(g_t+1)}dg_t = -dt \tag{A.4}$$

where we have dropped the dependency on z for clarity. By integrating, one gets

$$2\log\frac{g_t+1}{g_0+1} - \log\frac{g_t}{g_0} = t_0 - t \tag{A.5}$$

whence, by setting the initial condition $t_0 = 0$ and exponentiating,

$$\frac{g_0}{(g_0+1)^2}\frac{(g_t+1)^2}{g_t} = e^{-t} \tag{A.6}$$

whose solution is

$$g_t = \frac{(g_0+1)^2}{2g_0}\left[e^{-t} - \frac{2g_0}{(g_0+1)^2} - \sqrt{e^{-2t} - \frac{4e^{-t}g_0}{(g_o+1)^2}}\right] \tag{A.7}$$

Actually, since Equation (A.2) is quadratic, it also allows the solution with the "+" sign before the square root in (A.7). The "−" sign is chosen, because this is the only solution which sends the interior of $\mathbb{D}$ onto $\mathbb{D}$.

Substituting the initial condition $g_0(z) = z$ to read the behavior of the map in the actual complex plane, we get

$$g_t(z) = \frac{1}{4e^t z}\left[2(z+1)^2 - 4e^t z - 2(z+1)\sqrt{(z+1)^2 - 4e^t z}\right] \tag{A.8}$$

and finally, by inverting and substituting $t = \Delta$, we obtain the atomic map

$$\phi_k^{\mathbb{D}}(z) = \frac{1}{4e^{-\Delta_k} z}\left[2(z+1)^2 - 4e^{-\Delta_k} z - 2(z+1)\sqrt{(z+1)^2 - 4e^{-\Delta_k} z}\right], \tag{A.9}$$

which is of course Equation (3.19). Inversion of equation (A.8) turns out to be just an inversion of time $t \mapsto -t$. The reason why this is true will be clear in the following. In this radial case as well as in the chordal case discussed in Chapter 3, the choice of the analytical branch of the square root is crucial. Here — opposite to the choice we made for the map in (3.13) — we need to set the branch cut on the *negative* real axis, so that $\sqrt{(z+1)^2}$ will have positive real part for $z \in \mathbb{D}$.

Another way of looking at the problem of constructing a slit mapping for the disc is to try and guess it by composing known maps. The map

$$\phi(z) = \frac{4z}{(z+1)^2} \tag{A.10}$$

sends the open unit disc onto the complex plane minus the semi-infinite real needle $(1, \infty)$. It leaves the points 0 and 1 invariant, and opens up the unit circumference, mapping it onto the needle. Moreover, real points $0 < x < 1$ are mapped to real points $0 < x' < 1$. One can exploit this simple map by devising the slit mapping in the new geometry realized by ϕ. In fact, a dilatation in this geometry

$$D_t(z) = e^t z \tag{A.11}$$

corresponds to the map g_t that absorbs the (t-dependent) slit in the disc geometry, as a little thinking convinces. Then

$$g_t = \phi^{-1} \circ D_t \circ \phi \tag{A.12}$$

which, by substituting the inverse of (A.10)

$$\phi^{-1}(z) = \frac{2 - z - 2\sqrt{1-z}}{z}, \tag{A.13}$$

yields[1] the desired result, that is Equation (A.8).

It is now clear that the inverse of $g_t(z)$ is simply $g_{-t}(z)$, since from (A.12) one has

$$\begin{aligned} g_t^{-1} &= \left(\phi^{-1} \circ D_t \circ \phi\right)^{-1} \\ &= \phi^{-1} \circ (D_t)^{-1} \circ \phi \\ &= \phi^{-1} \circ D_{-t} \circ \phi = g_{-t}. \end{aligned} \tag{A.14}$$

[1]Here, as well as in the previous derivation from the Loewner equation, the sign in front of the sqare root must be chosen carefully.

Appendix B

Scaling of the step length in discrete SLE

We derive here the scaling relations (3.24) and (3.25). Let us start from the chordal case. Let l_n denote the length of the n-th step in the discretized growth, that is

$$l_n = |\gamma(t_n) - \gamma(t_{n-1})| \,. \tag{B.1}$$

We saw in Chapter 2 that the half-plane capacity is a measure of the size of a hull. Then, by approximating (B.1) by

$$l_n \sim |\gamma(t_n)| - |\gamma(t_{n-1})| \tag{B.2}$$

as if it grew radially, one gets

$$l_n \sim \mathrm{hcap}\left(\gamma[0,t_n]\right) - \mathrm{hcap}\left(\gamma[0,t_{n-1}]\right), \tag{B.3}$$

and since the capacity of the composition of the atomic maps is the sum of the capacities, one can write

$$\begin{aligned} l_n &\sim \sqrt{\sum_{i=0}^{n} \Delta_i} - \sqrt{\sum_{i=0}^{n-1} \Delta_i} \\ &= \frac{1}{2}\Delta_n \left(\sum_{i=0}^{n-1} \Delta_i\right)^{-\frac{1}{2}} . \end{aligned} \tag{B.4}$$

Setting

$$\Delta_i = \Delta i \tag{B.5}$$

in Equation (B.4) and then expanding at first order around infinity yields

$$l_n \sim \sqrt{\frac{\Delta}{2}} \left[1 + \frac{1}{2n} + O\left(\frac{1}{n^2}\right)\right], \tag{B.6}$$

which shows that scaling Δ_i as in (3.24) provides an asymptotically constant step length. The constant value reached for large n can be adjusted through the choice of Δ. Of course the foregoing is just an approximation, and the actual step length is a random variable, but its mean behaves as described.

Let us move on to the whole-plane radial case. Now the exponential of the logarithmic capacity is a measure of the linear size of the growing hull. This is essentially a consequence of the Koebe 1/4 theorem, which bounds the size of the image of the unit disc $\mathbb{D}$ under a conformal map g in terms of $g'(0)$. One gets

$$\begin{aligned} l_n &\sim \exp\left(\sum_{i=0}^{n} \Delta_i\right) - \exp\left(\sum_{i=0}^{n-1} \Delta_i\right) \\ &= \left(e^{\Delta_n} - 1\right) \exp\left(\sum_{i=0}^{n-1} \Delta_i\right) \end{aligned} \tag{B.7}$$

Setting

$$\Delta_i = \frac{\Delta}{i} \tag{B.8}$$

in Equation (B.7) and expanding yields

$$l_n \sim e^{\Delta\gamma}(n-1)^{\Delta}\left[\frac{\Delta}{n} + O\left(\frac{\Delta^2}{n^2}\right)\right] \tag{B.9}$$

where γ is the Euler-Mascheroni constant. By choosing $\Delta = 1$ one then has

$$l_n \sim e^{\gamma}\left[1 - \frac{1}{2n} + O\left(\frac{1}{n^2}\right)\right], \tag{B.10}$$

which shows that scaling Δ_i as in (3.25) provides an asymptotically constant step length. Here, contrary to the half-plane case, there is no freedom left to choose the mean step length, since Δ has to be fixed to 1 in order to have the correct scaling behavior. Operatively, one keeps a constant Δ_i for a few steps, until the step-length has approximately reached the desired value[1], and then sets $\Delta_i = 1/i$ from then on.

[1]The actual amplitude will be corrected by a factor e^{γ}, but this is of order unity.

List of Figures

List of Tables

Bibliography

[1] P. J. Flory, *Principles of polymer chemistry*, Cornell University Press, Ithaca NY, 1953.

[2] H. Yamakawa, *Modern theory of polymer solutions*, Harper & Row, New York, 1971.

[3] P.-G. de Gennes, *Scaling concepts in polymer physics*, Cornell University Press, Ithaca NY, 1979.

[4] K. F. Freed, *enormalization group theory of macromolecules*, John Wiley & Sons, New York, 1987.

[5] J. des Cloizeaux, G. Jannink, *Les Polymères en Solution*, Les Editions de Physique, Les Ulis, 1990.

[6] H. Fujita, *Polymer solutions*, Elsevier, New York, 1990.

[7] N. Madras, G. Slade, *The self-avoiding walk*, Birkhäuser Boston, 1996.

[8] A. D. Sokal, *Monte Carlo methods for the self-avoiding walk*, Nuc. Phys. B **47**, 172–179, 1996.

[9] G. Grimmett, *Percolation*, Springer-Verlag, New York, 1989.

[10] A. Coniglio, N. Jan, I. Majid, E. Stanley, *Conformation of a polymer chain at the θ' point: connection to the external perimeter of a percolation cluster*, Phys. Rev. B **35**, 3617–3620, 1987.

[11] K. G. Wilson, *Renormalization group and critical phenomena*, Phys. Rev. B **4**, 3174, 1971.

[12] K. G. Wilson, J. Kogut, *The renormalization group and the ϵ-expansion*, Phys. Rep. C **23**, 75, 1974.

[13] P. G. de Gennes, *Exponents for the excluded volume problem as derived by the wilson method*, Phys. Lett. **38A**, 339, 1972.

[14] J. Cardy *Scaling and renormalization in statistical physics*, Cambridge University Press, 2000.

[15] H. Saleur, *Conformal invariance for polymers and percolation* J. Phys. A: Math. Gen. **20**, 455, 1987.

[16] J. Cardy, *SLE for theoretical physicists*, Annals Phys. **318**, 81–118, 2005 (`cond-mat/0503313`).

[17] W. Kager, B. Nienhuis, *A guide to stochastic Löwner evolution and its applications*, J. Stat. Phys. **115**, 1149–1229, 2004 (`math-ph/0312056`).

[18] M. Bauer, D. Bernard, *2D growth processes: SLE and Loewner chains*, Phys. Rept. **432**, 115–221, 2006.

[19] I. A. Gruzberg, *Stochastic geometry of critical curves, Schramm-Loewner evolutions, and conformal field theory*, J. Phys. A: Math. Gen. **39**, 12601–12655, 2006 (`math-ph/0607046`).

[20] G. F. Lawler, *An introduction to the stochastic Loewner evolution*, in Vadim Kaimanovich, *Random walks and geometry*, Walter de Gruyter GmbH & Co. KG, Berlin, 261-293, 2004.

[21] K. Löwner, *Untersuchungen über schlichte konforme Abbildungen des Einheitskreises*, I, Math. Ann. **89**, 103, 1923.

[22] Z. Nehari, *Conformal mapping*, MacGraw-Hill Book Co., 1952.

[23] P. Di Francesco, P. Mathieu, D. Senechal, *Conformal field theory*, Springer, New York, 1997.

[24] J. Cardy, *Conformal invariance and statistical mechanics*, in Field Strings and Critical Phenomena, Elsevier Science Publishers BV, 1989.

[25] O. Schramm, *Scaling limits of loop-erased random walks and uniform spanning trees*, Israel J. Math. **118**, 221, 2000 (`math.PR/9904022`).

[26] P. Oikonomou, I. Rushkin, I. A. Gruzberg, L. P. Kadanoff, *Global properties of Stochastic Loewner evolution driven by Levy processes*, J. Stat. Mech., P01019, 2008 (`0710.2680v2`).

[27] S. Rohde, O. Schramm, *Basic properties of SLE*, Ann. Math. **161**, 879–920, 2005 (`math.PR/0106036`).

[28] V. Beffara, *The dimension of SLE curves*, Ann. Prob. **36**, No. 4, 1421-1452, 2008 (`math/0211322`).

[29] B. Duplantier, *Conformally invariant fractals and potential theory*, Phys. Rev. Lett. **84**, 1363, 2000 (`cond-mat/9908314`).

[30] *Conformal Invariance and Applications to Statistical Mechanics*, edited by C. Itzykson, H. Saleur, and J.-B. Zuber, World Scientific, Singapore, 1988; P. Ginsparg, "Applied conformal field theory", pp.1-168 in *Les Houches 1988, fields, strings and critical phenomena* edited by E. Brézin and J. Zinn-Justin, North-Holland, 1990; C. Itzykson and J.-M. Drouffe, *Statistical Field Theory* vol.1, 2, Cambridge Univ. Press, 1989; S. V. Ketov, *Conformal Field Theory*, World Scientific, 1995; P. Di Francesco, P. Mathieu and D. Sénéchal, *Conformal Field Theory*, Springer, 1997; V. G. Kac and A. K. Raina, *Bombay Lectures on Highest Weight Representations of Infinite Dimensional Lie Algebras*, World Scientific, 1987.

[31] M. Bauer, D. Bernard, *Conformal Field Theories of Stochastic Loewner Evolutions*, Commun. Math. Phys. **239**, 493-521 (2003) (`hep-th/0210015v3`).

[32] R. Friedrich, W. Werner, *Conformal fields, restriction properties, degenerate representations and SLE*, C.R. Acad. Sci. Paris, Ser. I Math. **335**, 947, 2003 (`math.PR/0209382`); *Conformal restriction, highest-weight representations and SLE*, Comm. Math. Phys. **243**, 105, 2003 (`math-ph/0301018`).

[33] G. F. Lawler, O. Schramm, W. Werner, *Conformal invariance of planar loop-erased random walks and uniform spanning trees*, Ann. Prob. **32**, 939, 2004 (`math.PR/0112234`).

[34] C. Amoruso, A. K. Hartmann, M. B. Hastings, M. A. Moore, *Conformal invariance and SLE in two-dimensional Ising spin glasses*, Phys. Rev. Lett. **97**, 267202, 2006 (`cond-mat/0601711`).

[35] G. F. Lawler, O. Schramm, W. Werner, *On the scaling limit of planar self-avoiding walk*, in *Fractal geometry and applications: a jubilee of Benoit Mandelbrot*, Part 2, 339, Proc. Sympos. Pure Math. 72, Part 2, Amer. Math. Soc., Providence, RI, 2004 (`math.PR/0204277`).

[36] R. Kenyon, *Dominos and the Gaussian free field*, Ann. Probab. **29**, 1128, 2001 (`math-ph/0002027`).

[37] O. Schramm, S. Sheffield, *The harmonic explorer and its convergence to SLE_4*, Ann. Probab. **33**, 2127, 2005 (`math.PR/0310210`).

[38] O. Schramm, S. Sheffield, *Contour lines of the two-dimensional discrete Gaussian free field*, (`math.PR/0605337`).

[39] D. Bernard, G. Boffetta, A. Celani, G. Falkovich, *Inverse turbulent cascades and conformally invariant curves*, Phys. Rev. Lett. **98**, 024501, 2007.

[40] S. Smirnov, *Critical percolation in the plane: conformal invariance, Cardy's formula, scaling limits*, C. R. Acad. Sci. Paris Sér. I Math. **333**, 239, 2001.

[41] S. Smirnov, W. Werner, *Critical exponents for two-dimensional percolation*, Math. Res. Lett. **8**, 728, 2001 (`math.PR/0109120`).

[42] F. Camia, C. M. Newman, *Critical percolation exploration path and SLE_6: a proof of convergence*, Probab. Theory Related Fields, **139**, 473519, 2007.

[43] T. Kennedy, *A fast algorithm for simulating the chordal Schramm-Loewner evolution* (`math/0508002v2`).

[44] R. Bauer, *Discrete Loewner Evolution*, Annales de la faculté des sciences de Toulouse Sr. 6, 12 no. 4, 433–451, 2003 (`math.PR/0303119`).

[45] T. Kennedy, *Monte Carlo comparisons of the self-avoiding walk and SLE as parameterized curves*, (`arXiv:math/0510604`).

[46] G. F. Lawler, *Dimension and natural parametrization for SLE curves*, (`math.PR/0712.3263v1`).

[47] T. A. Witten, L. M. Sander, *Diffusion-limited aggregation: a kinetic critical phenomenon*, Phys. Rev. Lett. **47**, 1400–1403, 1981.

[48] M. Z. Bazant, D. Crowdy, *Conformal mapping methods for interfacial dynamics*, in Volume I of the *Handbook of Materials Modeling*, ed. by S. Yip, (Springer Science and Business Media), 2005 (`cond-mat/0409439v1`).

[49] M. B. Hastings, L. S. Levitov, *Laplacian growth as one-dimensional turbulence*, Physica D **116**, 244–252, 1998.

[50] M. G. Stepanov, L. S. Levitov, *Laplacian growth with separately controlled noise and anisotropy*, Phys. Rev. E **63**, 061102, 2001 (`cond-mat/0005456v2`).

[51] T. Kennedy, *The length of an SLE — Monte Carlo studies*, J. Stat. Phys. **128**, 1263–1277, 2007.

[52] S. Caracciolo, M. Gherardi, M. Papinutto, A. Pelissetto, *θ-point polymers in two dimensions*, in preparation.

[53] S. Caracciolo, A. Pelissetto, A. D. Sokal, J. Phys. A: Math. Gen. **23**, L969 (1990)

[54] J. L. Cardy, H. Saleur, J. Phys. A: Math. Gen. **22**, L601 (1989)

[55] J. des Cloizeaux and G. Jannink, *Les Polymères en Solution* (Les Editions de Physique, Les Ulis, 1987); English translation: *Polymers in Solution: Their Modeling and Structure* (Oxford Univ. Press, Oxford–New York, 1990).

[56] P. G. de Gennes, *Scaling Concepts in Polymer Physics* (Cornell Univ. Press, Ithaca, NY, 1979).

[57] P. J. Flory, *Principles of Polymer Chemistry* (Cornell University Press, Ithaca, NY, 1953).

[58] K. F. Freed, *Renormalization-Group Theory of Macromolecules* (John Wiley, New York, 1987).

[59] P. G. de Gennes, Phys. Lett. **A38**, 339 (1972).

[60] M. E. Fisher and B. J. Hiley, J. Chem. Phys. **34**, 1253 (1961).

[61] M. E. Fisher, J. Chem. Phys. **44**, 616 (1966).

[62] D. S. Mc Kenzie and M. A. Moore, J. Phys. **A4**, L82 (1971).

[63] J. des Cloizeaux, Phys. Rev. **A10**, 1665 (1974); J. Physique **41**, 223 (1980).

[64] J. Dayantis and J.-F. Palierne, J. Chem. Phys. **95**, 6088 (1991).

[65] N. Eizenberg and J. Klafter, J. Chem. Phys. **99**, 3976 (1993).

[66] S. Caracciolo, M. S. Causo, and A. Pelissetto, J. Chem. Phys. 111, 7693 (2000).

[67] S. Caracciolo, M. S. Causo, G. Ferraro, M. Papinutto, and A. Pelissetto, J. Stat. Phys. **100**, 1111 (2000).

[68] B. Duplantier and H. Saleur, Phys. Rev. Lett. **59**, 539 (1987).

[69] T. Ishinabe, J. Phys. A **20**, 6435 (1987).

[70] F. Seno and A. L. Stella, J. Physique (France) **49**, 739 (1988).

[71] D. Maes and C. Vanderzande, Phys. Rev. A **41**, 3074 (1990).

[72] H. Meirovitch and H. A. Lim, J. Chem. Phys. **92**, 5144 (1990).

[73] D. P. Foster, E. Orlandini, and M. C. Tesi, J. Phys. A **25**, L1211 (1992).

[74] I. Chang and H. Meirovitch, Phys. Rev. E **48**, 3656 (1993).

[75] A. L. Owczarek, T. Prellberg, D. Bennett-Wood, and A. J. Guttmann, J. Phys. A **27**, L919 (1994).

[76] P. Grassberger and R. Hegger, J. Physique (France) I **5**, 597 (1995).

[77] P. P. Nidras, J. Phys. A **29**, 7929 (1996).

[78] G. T. Barkema, U. Bastolla and P. Grassberger, J. Stat. Phys. **90**, 1311 (1998), cond-mat/9707312.

[79] P. Grassberger, *Pruned-enriched Rosenbluth method: simulations of θ-polymers of chain length up to 1 000 000*, Phys. Rev. E **56**, 3682, 1997.

[80] M. Gherardi, *Whole-plane SAW and radial SLE: a numerical study*, in preparation.